COO-1195-351

PHOTOPRODUCTION OF ELECTRON PAIRS AT HIGH ENERGY

BY

LAIRD RENNY CORMELL, JR.

B.S. University of Oklahoma, 1970
M.S. University of Illinois, 1971

THESIS

Submitted in partial fulfillment of the requirements
for the degree of Doctor of Philosophy in Physics
in the Graduate College of the
University of Illinois at Urbana-Champaign, 1976

Urbana, Illinois

FERMILAB
LIBRARY

PHOTOPRODUCTION OF ELECTRON PAIRS

AT HIGH ENERGY

Laird Renny Cormell, Jr., Ph.D.

Department of Physics

University of Illlinois at Urbana-Champaign, 1976

In an experiment at the wide band neutral beam of FNAL large mass electron pairs from high energy photon interactions on Be were detected. The $\psi(3095)$ meson as well as a large mass Bethe-Heitler continuum is observed. The following cross sections for the interaction $\gamma + Be \rightarrow \underset{\hookrightarrow e^+e^-}{\psi} + X$ are measured

$$B\sigma = (15 \pm 2)\,nb$$

$$\left(\frac{d\sigma}{dt}\right)_{t=0} = (59 \pm 15)\,nb/GeV^2$$

from which we obtain

$$\sigma(\psi N) = (1.3 \pm 0.3)\,mb$$

which indicates that the ψ is a hadron. Distributions of K, t, p_T and $\cos\theta^*$ for ψ photoproduction are given. Comparisons are made with other experiments and the ratio $ee/\mu\mu$ is shown to be 1.0 ± 0.15.

ACKNOWLEDGMENTS

I am especially grateful to Professor A. Wattenberg for assistance and guidance in preparing this thesis and in conducting the experiment.

I would like to thank the members of the group who performed the experiment for their endless work and extreme dedication. They are: J. Bronstein, R. Coleman, G. Gladding, M. Gormley, R. Messner, T. O'Halloran, J. Sarracino, D. Wheeler, B. Knapp, W. Lee, P. Leung, S. Smith, A. Wijangco, M. Binkley, R. Orr, J. Peoples and L. Read.

I would also like to thank the staff of the FNAL and in particular, the staffs of the Proton Department and the Computing Department.

I have appreciated helpful discussions with B. Lee and W. Bardeen.

This thesis is dedicated to Brendel and Robin.

This research was supported in part by the U.S. Energy Research and Development Administration under contract E(11-1)-1195.

NOTE TO THE READER

The author apologizes for his extensive use of symbols and acronyms. Many of the terms in the text become very cumbersome without these abbreviations. All such terms are defined with their first usage. Furthermore, a glossary has been included to assist the reader by redefining these terms.

TABLE OF CONTENTS

I. INTRODUCTION 1

II. BEAM LINE AND EXPERIMENTAL DETAILS 11

A. Wide Band Neutral Beam 11
B. Apparatus 18
C. Electronics 43
D. Spectrum Measurement and Shower Detector Calibration 77

III. DATA AND RESULTS 88

A. Overview 88
B. Raw Data 88
C. Background 101
D. Acceptance, Flux and Efficiency Corrections. 108

1. Acceptance and Flux 110
2. Efficiency 114

E. Results and Conclusions 119

1. Total Cross Section 120
2. Differential Cross Section 120
3. Additional Distributions and Di-Lepton Continuum 125
4. Comparison to Other Experiments 130

APPENDIX I: DETAILS OF ANALYSIS 137

APPENDIX II: LIGHT PULSER SYSTEM 147

GLOSSARY 161

LIST OF REFERENCES 164

VITA 167

I. INTRODUCTION

The coupling of the photon to other $J^{PC} = 1^{--}$ states is a well established fact. It is this coupling that allows one to readily photoproduce vector mesons. Furthermore, the vector meson dominance model (VMD) is a useful (if not entirely satisfactory) way to view the coupling.[1-5] VMD connects the hadronic electromagnetic current $j_\mu^{em}(X)$ to the vector meson fields $V_\mu(X)$ by the current-field equation

$$j_\mu^{em}(X) = -\sum_V \left(\frac{m_V^2}{\gamma_V}\right) V_\mu(X) \tag{1}$$

where m_V is the mass of the vector and γ_V is the coupling constant of the photon to the vector meson (ρ, ω, ϕ).

This model has achieved a considerable amount of success in predicting photoproduction cross sections.[4] However, there is no reason to believe that Eq. 1 is summed only over the ρ, ω, and ϕ. Previous photoproduction searches have indicated that there are no new vector mesons of mass less than 1.5 GeV.[6-7] The photoproduction experiment we shall describe here was proposed in 1970 to search for the existence of large mass vector mesons (among other things).

Theoretical developments since that time have made this search even more desirable. In particular we note the work on the unification and renormalization of the weak and electromagnetic fields.[8-12] As a consequence of this work a new quantity, charm, was introduced. If charm does exist, then there must be a vector meson composed of a charmed (c) quark-antiquark

pair ($c\bar{c}$) in a^3S_1 state. And furthermore, this vector meson will couple directly to the photon.[13-14]

If we assume the existence of a $c\bar{c}$ vector meson and the possibility of its photoproduction, in what manner can we expect to detect it. There are two possibilities:

1. If the mass of the $c\bar{c}$ vector meson lies above the threshold to produce two charmed mesons, it will decay strongly into those mesons with a typical strong decay width limited only by phase space. The subsequent weak decays of the charmed mesons could then be detected.
2. If the mass of the vector meson lies below this charm threshold, it cannot decay into charmed mesons. Furthermore, its decay into ordinary mesons would be suppressed by Zweig's rule giving the vector meson a very narrow width.[15]

In case (1) we have a system analogous to the ϕ meson which is presumably a strange quark-antiquark pair ($s\bar{s}$). The ϕ lies just above the threshold for producing two strange mesons ($K\bar{K}$) and consequently it decays into $K\bar{K}$ pairs. The narrowness of the ϕ decay width is attributable to the fact it is just barely more massive than two kaons (phase space).

In the second case, (2), hadronic decays would be suppressed but we would expect a decay width into lepton pairs comparable with the other vector mesons ($\approx$ few KeV). In this case the width for leptonic decay would become an appreciable fraction of the total decay width (c.f. $\approx 5 \times 10^{-5}$ for the other vector

mesons). Therefore photoproduction of lepton pairs would be of considerable interest.

Recently two narrow resonances $\psi(3095)$ and $\psi'(3684)$ which couple directly to the photon ($J^{PC} = 1^{--}$) were discovered in e^+e^- annihilation at SLAC[16-17] (Fig. 1a). Since then much work has been done to determine the quantum numbers and branching ratios of the ψ meson.[18] Setting aside the question of charm for a moment, the ψ seems to have the properties of the vector meson described in (2) above. That is

$$\Gamma = (69 \pm 15)\,\text{KeV}$$

$$\Gamma_e = \Gamma_\mu = (4.8 \pm 0.6)\,\text{KeV}$$

$$\Gamma_{e/\Gamma} = 0.069 \pm 0.009$$

where Γ is the decay width. This is indeed an extremely narrow width for such a massive particle. However, the leptonic branching ratio is large.

Typically we would expect decay widths on the order of

Strong Decay:	$\Gamma \sim 100$ MeV
Radiative Decay:	$\Gamma \sim 0.5$ MeV
Second Order Electromagnetic Decay:	$\Gamma \sim 5$ KeV.

So we see that Γ_ψ is comparable to second order electromagnetic decays. If the ψ is a hadron, this is certainly a strange, if not charming, observation.

There are three logical possibilities to explain the narrowness of the ψ.

1. The ψ is not a hadron.
2. The ψ is a hadron but it possesses a new non-additive quantum number such as color which forbids its strong decay.

3. The ψ is a hadron but its strong decay is inhibited by a new dynamical mechanism such as charm.

We can reject the first possibility for two reasons. The first is that the ψN (ψ-nucleon) cross section is, as we shall show in Sec. III, consistent with the predicted value for a vector meson of its mass. The second is the fact that the ψ is observed to have a definite G parity.[19]

Harari[20] has argued that we can also reject the Han-Nambu color model[21] as an explanation of the narrowness of the ψ. The Han-Nambu model makes several very definite predictions about ψ decays and the production of ψ's in e^+e^- annihilation above $\sqrt{s}$ = 4 GeV. Several of the predictions are not observed.

	Prediction[20]		Observation[19,22]
1.	$e^+e^- \to \text{hadrons} \hookrightarrow \psi$, $\sqrt{s} > 4$ GeV	Large	Small
2.	$\Gamma(\psi \to \gamma + \text{hadrons}) \approx$ 1-10 MeV		40 KeV
3.	$\Gamma(\psi \to \pi^+\pi^-\gamma) > \Gamma(\psi \to \pi^+\pi^-\pi')$		$\Gamma(\psi \to \pi^+\pi^-\pi') \gg \Gamma(\psi \to \pi^+\pi^-\gamma)$
4.	$\Gamma(\psi \to \pi^+\pi^-K^+K^-) = 0$		0.19 KeV
5.	$\Gamma(\psi \to \pi^+\pi^-\pi^+\pi^-\pi^\circ) = 0$		1.88 KeV

From these observations then, Harari states that the ψ does not possess a new non-additive quantum number like color.

The third possibility involves an internal non-observable quantum number. All of the above observations are consistent with the prediction of the charmed quark model. The proof of this model depends on establishing the existence of charmed hadrons experimentally.

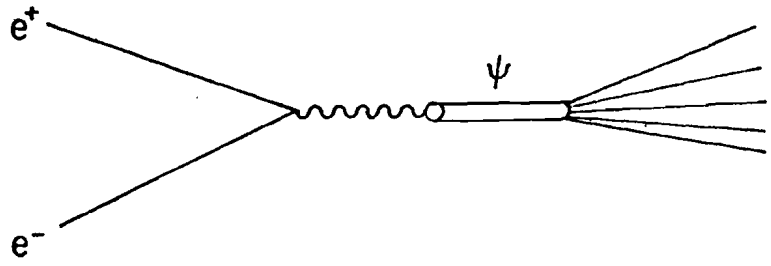

(a)

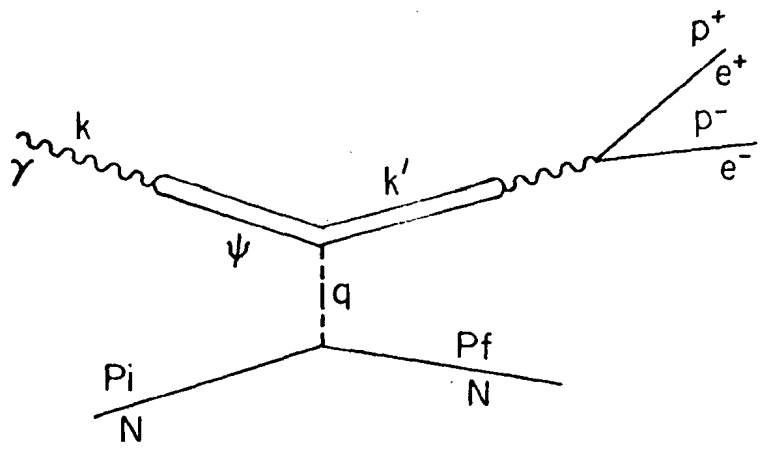

(b)

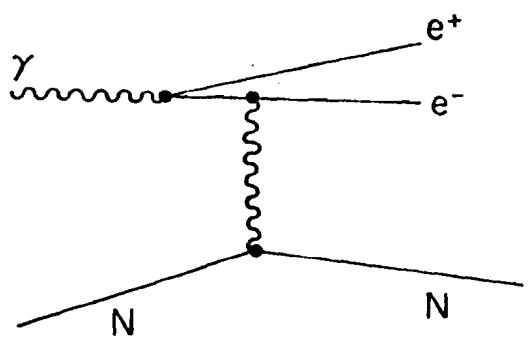

(c)

At this point there are no experimental observations which tend to reject the charm scheme. In fact, recent observations of new states at DESY[23] and SLAC[24] are consistent with the predicted "charm spectroscopy."

Regardless of whether the ψ is a $c\bar{c}$ vector meson or not, we can determine several of its properties from photoproduction. In this experiment we have measured the ψ photoproduction cross section at high energy, its t (invariant momentum transfer) distribution, and obtained the ψN cross section (Fig. 1b).

The vector mesons are known to be produced by diffractive scattering of photons from nuclei.[3-5] We expect the ψ to be produced in the same way and therefore we consider the following model of high energy diffraction from nuclear targets.[25] Let us assume an interaction potential $v(\vec{r} - \vec{r}_i)$ between the incident particle at position $\vec{r}$ and the target nuclei at r_i. Then in the Born approximation the matrix element for scattering at momentum transfer $\vec{q}$ between the initial $|I\rangle$ and final $|F\rangle$ nuclear states is

$$\begin{aligned} M_{FI}(\vec{q}) &= \langle F| \int e^{i\,\vec{q}\cdot\vec{r}} \sum_i v(\vec{r} - \vec{r}_i)\, d^3r \,|I\rangle \\ &= v(\vec{q}) \langle F| \sum_i e^{i\,\vec{q}\cdot\vec{r}_i} |I\rangle \end{aligned} \tag{2}$$

where $v(\vec{q}) = \int e^{i\,\vec{q}\cdot\vec{r}}\, d^3r$ is the corresponding two-body scattering amplitude. Summing over nuclear states (assumed degenerate) and ignoring nucleon-nucleon interactions we have

$$\frac{d\sigma}{dt} \sim \sum_F |M_{FI}|^2 = |v(\vec{q})|^2 \{A^2 |F(\vec{q})|^2 + A(1 - |F(\vec{q})|^2)\} \tag{3}$$

where $F(q) = \int \rho(\vec{r})\ e^{i\ \vec{q}\cdot\vec{r}}\ d^3r$ is the single particle form factor and ρ is the nuclear density. This equation corresponds to the sum of coherent ($\sim A^2$) and incoherent ($\sim A$) amplitudes squared. The coherent piece dominates for small t ($-q^2$) where $F(\vec{q}) \approx 1$. For large t values incoherent processes dominate as $F(\vec{q})$ approaches 0. At $t = 0$ ($\vec{q} = 0$) we have

$$\left(\frac{d\sigma}{dt}\right)_{t=0} \sim A^2 |v(o)| \tag{4}$$

which is solely determined by the coherent part. There are of course, t_{min} effects which enter into the measurement of $(d\sigma/dt)$ since a particle cannot be produced without some momentum transfer.

By measuring $\left(\frac{d\sigma}{dt}\right)_{t=0}$ and employing the optical theorem we can calculate the ψ-nucleon total cross section. Using VMD we first calculate the amplitude f for $\gamma + N \to \psi + N$ in Fig. 1b.

$$f(\gamma\to\psi) = e\left(\frac{M_\psi^{\ 2}}{\gamma_\psi}\right)\left(\frac{1}{M_\psi^{\ 2}}\right)\ f(\psi\to\psi)\,. \tag{5}$$

Squaring both sides we obtain

$$\frac{d\sigma}{dt}\ (\gamma \to \psi) = \left(\frac{e}{\gamma_\psi}\right)^2 \frac{d\sigma}{dt}\ (\psi \to \psi)\,, \tag{6}$$

and from the lepton vertex in Fig. 1b we obtain

$$\Gamma(\psi \to e^+e^-) = \frac{1}{12\pi}\ \left(\frac{e^2}{\gamma_\psi}\right)^2\ M_\psi; \tag{7}$$

therefore

$$\frac{d\sigma}{dt}\ (\gamma \to \psi) = \frac{3}{\alpha}\ \frac{\Gamma(\psi \to e^+e^-)}{M_\psi}\ \frac{d\sigma}{dt}\ (\psi \to \psi)\,. \tag{8}$$

The optical theorem states

$$\mathrm{Im}\ f\Big|_{t=0} = 2p^* \sqrt{s}\ \sigma_{tot} \tag{9}$$

where p^* is the cm momentum and s is the invariant mass. Now recall that

$$\frac{d\sigma}{dt} = \frac{1}{64\pi\ p^{*2}s}\ |f|^2, \tag{10}$$

and if α_ψ is the ratio of real to imaginary parts of the forward scattering amplitude, then combining (9) and (10) we have

$$\frac{d\sigma}{dt}\ (\psi \to \psi)\Big|_{t=0} = \frac{1}{16\pi}\ \sigma^2(\psi \to \psi)(1 + \alpha_\psi{}^2). \tag{11}$$

And finally, from (8) and (11) we obtain

$$\frac{d\sigma}{dt}\ (\gamma \to \psi)\Big|_{t=0} = \frac{3}{\alpha}\ \frac{\Gamma(\psi \to e^+e^-)}{M_\psi}\ \frac{(1 + \alpha_\psi{}^2)}{16\pi}\ \sigma^2(\psi \to \psi). \tag{12}$$

Thus by measuring $(\frac{d\sigma}{dt})_{t=0}$ for ψ photoproduction we obtain the ψN $(\psi-\psi)$ cross section.

If the ψ is a hadron what sort of ψN cross section can we expect? Based on a quark VMD model, Carlson and Freund[13] have shown that we should expect

$$\sigma\ (\psi N)/\sigma(\rho N) \approx m\rho^2/m_\psi{}^2 = 0.06,$$

or (13)

$$\sigma(\psi N) \approx 1.6\ \mathrm{mb}.$$

We note in passing that for the ϕ this prediction is in good agreement with the experimental observations for the ϕN cross section.

In photoproduction of lepton pairs we can anticipate a large contribution to the overall rate from Bethe-Heitler[26] pairs (Fig. 1c). Bethe-Heitler (B-H) theory with later

improvements[27-29] has been found to be in very good agreement with experimental measurements.[30-33] What we are searching for then are vector mesons such as the ρ', ω', ϕ' and ψ above this B-H background.

In the following sections we will discuss the experiment performed to study the photoproduction of lepton pairs at high energy. We will present data which shows the diffractive photoproduction of ψ mesons from which we will calculate $\sigma(\gamma \rightarrow \psi)$, $\frac{d\sigma}{dt}$, $\frac{d\sigma}{dK}$ and $\sigma(\psi N)$.

II. BEAM LINE AND EXPERIMENTAL DETAILS

A. Wide Band Neutral Beam

The experiment was performed in the wide band neutral beam line of the Proton Lab at Fermi National Accelerator Laboratory (FNAL). A diagram of this beam line is shown in Fig. 2. Protons of 300 or 380 GeV/c momentum from the FNAL main ring are steered down the proton line to the Proton-East target box by conventional beam line optics. The beam is then focused to a spot size of 2 mm x 3 mm at the target box where it strikes a 30.5 cm beryllium target. (See Fig. 3.)

Typical proton beam intensities were $2 \times 10^{11} - 1 \times 10^{12}$ protons per pulse. Beam intensity and targeting efficiency were continuously monitored by segmented wire ion chambers (SWIC's), secondary emission monitors (SEM), and ion chamber loss monitors. Beam position was determined by the SWIC's and was displayed on closed circuit TV monitors. The SEM's determined beam intensity while the loss monitors determined targeting efficiency. The outputs of these monitors were integrated, digitized, scaled, and written on magnetic tape.

The non-interacting beam and other charged particles are swept into a dump in the target box by sweeping magnets. (See Fig. 3.) Muons, however, present a further problem since the more energetic ones are not stopped by the dump. Also, muons which are bent away from the beam line and enter the return yokes of the sweeping magnets tend to be bent back into

the beam. Toroidally wound muon spoilers were installed to help reduce the muon flux. These magnets are wound such that they focus muons of one sign and defocus muons of the opposite sign. By using pairs of these magnets muon contamination was reduced by a factor of 2-3. Muon spoilers were installed both in front of the target box, to reduce upstream muons, and after, to reduce muons from the target and dump.

A neutral beam channel is then formed at 0° relative to the proton beam line by a collimator after the target box. (See Fig. 2.) The collimator has five openings of varying dimension and can be moved remotely from one hole to the other. In this way the neutral beam intensity and spot size can be varied. At this point the beam consists of photons, neutrons, kaons, and other neutral particles.

Following the first collimator the beam enters two liquid deuterium sections which serve as a neutron attenuator. Deuterium has the highest ratio of interaction length to radiation length, and therefore attenuates neutrons much more than photons. In fact, about 1000/1 reduction in the ratio of neutrons to photons is achieved when both deuterium sections are in operation. Consequently, following the deuterium sections the beam is almost entirely photons. The first section consists of a liquid deuterium cryostat 11 m long surrounded by three sweeping magnets 3 m long nominally set at 9 kG. The second section is 23 m long and is surrounded by six more magnets. The sweeping magnets, some 250 kG-m, remove electron pairs or other charged particles created in the deuterium.

Fig. 2. FNAL wide band neutral beam line. The beam is defined by two collimators. Neutrons in the beam are attenuated by two liquid D_2 cryostats; one is 11 m long and the other 23 m. Muon spoiler magnets reduce muon flux by a factor of 2-3. A $6X_0$Pb photon attenuator may be inserted into the beam one radiation length at a time to attenuate photons.

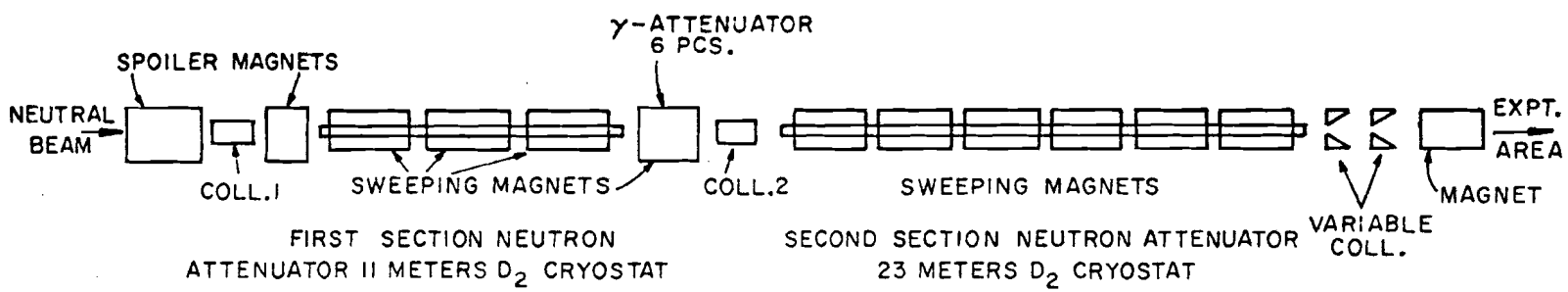
γ-ATTENUATOR
6 PCS.
SPOILER MAGNETS
NEUTRAL
BEAM
COLL.1
SWEEPING MAGNETS
COLL.2
SWEEPING MAGNETS
EXPT.
AREA
MAGNET
VARIABLE
COLL.
FIRST SECTION NEUTRON
ATTENUATOR 11 METERS D_2 CRYOSTAT
SECOND SECTION NEUTRON ATTENUATOR
23 METERS D_2 CRYOSTAT

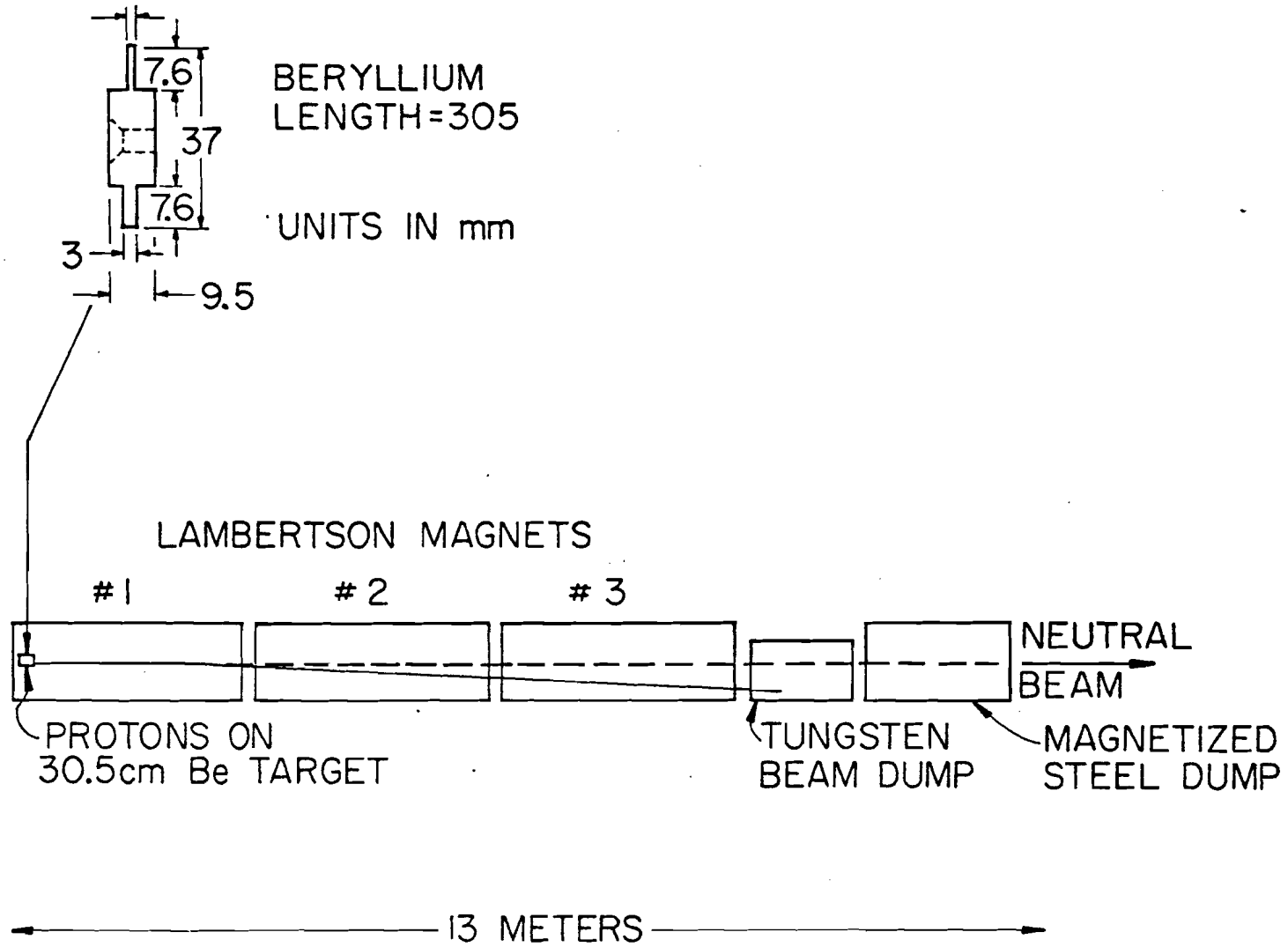
7.6
37
7.6
3
9.5
BERYLLIUM
LENGTH=305
UNITS IN mm
LAMBERTSON MAGNETS
#1
#2
#3
NEUTRAL
BEAM
PROTONS ON
30.5cm Be TARGET
TUNGSTEN
BEAM DUMP
MAGNETIZED
STEEL DUMP
13 METERS

Between the two deuterium sections is a second collimator, and another sweeping magnet. The second collimator like the first has several openings and is remotely controlled. This collimator mainly serves to reduce beam halo. Contained in the sweeping magnet is a remotely controlled lead attenuator which has the ability to insert, or remove, six radiation lengths of lead into the beam one radiation length at a time. If all six radiation lengths of lead are inserted, the beam becomes essentially all neutrons and background studies can be done. If the lead pieces are inserted one at a time, checks can be made to determine whether the deuterium cryostat is filled and whether the beam elements are positioned properly. (See Sec. II. D.)

Following the deuterium sections are two variable collimators. These collimators can be set to reduce beam halo. They are also used as safety devices, closing automatically whenever an access is made to the experimental area or there is some beam malfunction.

Finally, before the photon beam enters the experimental area there is about 100 ft of earth and steel to stop muons. This shielding reduces the muon flux by about a factor of ten.

The spectrum of the resulting beam is shown in Fig. 27. The beam is a wide band beam with an average photon energy of about 40 GeV, or 50 GeV from 300, or 380 GeV/c, protons respectively. The spectra resulting from 300 and 380 GeV/c protons is shown. Details of the measurements of these spectra will be given in Sec. II. D.

B. Apparatus

The experimental apparatus, as shown in Figs. 4-12 consists of a magnetic spectrometer and particle identification system. The magnet has a 41- x 61-cm aperture x 183 cm in length and was normally operated at 2700 A, which produced a field of about 8 kG or a 600 MeV/c momentum "kick." Particle tracks were detected by proportional wire chambers (PWC). There are five chambers, P0-P4, each containing three planes of signal wires, one plane of wires in each PWC is vertical, and the other two are crossed at an angle of 11° to the horizontal. The spacing between signal wires is 2 mm, except in the case of the X plane of the fifth chamber, P4, where the spacing is 3 mm. The first two chambers, P0 and P1, have active areas of 25-x 36-cm. The active area of P2 and P3 is 51- x 71-cm, and the active area of P4 is 102- x 152-cm. The spectrometer was found to give a resolution of

$$\frac{\Delta p}{p} = \pm\ 3.5\% \ \left(\frac{p}{100\ \mathrm{GeV/c}}\right). \tag{14}$$

Helium bags of increasing dimensions were inserted between the chambers to reduce multiple scattering and improve the resolution of the spectrometer.

Associated with the spectrometer are several sets of plastic scintillator arrays which were used as veto or trigger counters. The first plane contains seven counters called the A_μ counters numbered A0-A6. They are mounted in a vertical plane about 2 m upstream of the photon target. They serve to veto muons (or other charged particles) in and around the beam. The beam passes through the center counter,

Fig. 4. Apparatus, indicating the spatial arrangement of the magnetic spectrometer (vertical bending magnet, PWC's P0-P4), trigger and anti-counters, and the particle identification system (electron shower detectors, hadron calorimeter, and muon identifier).

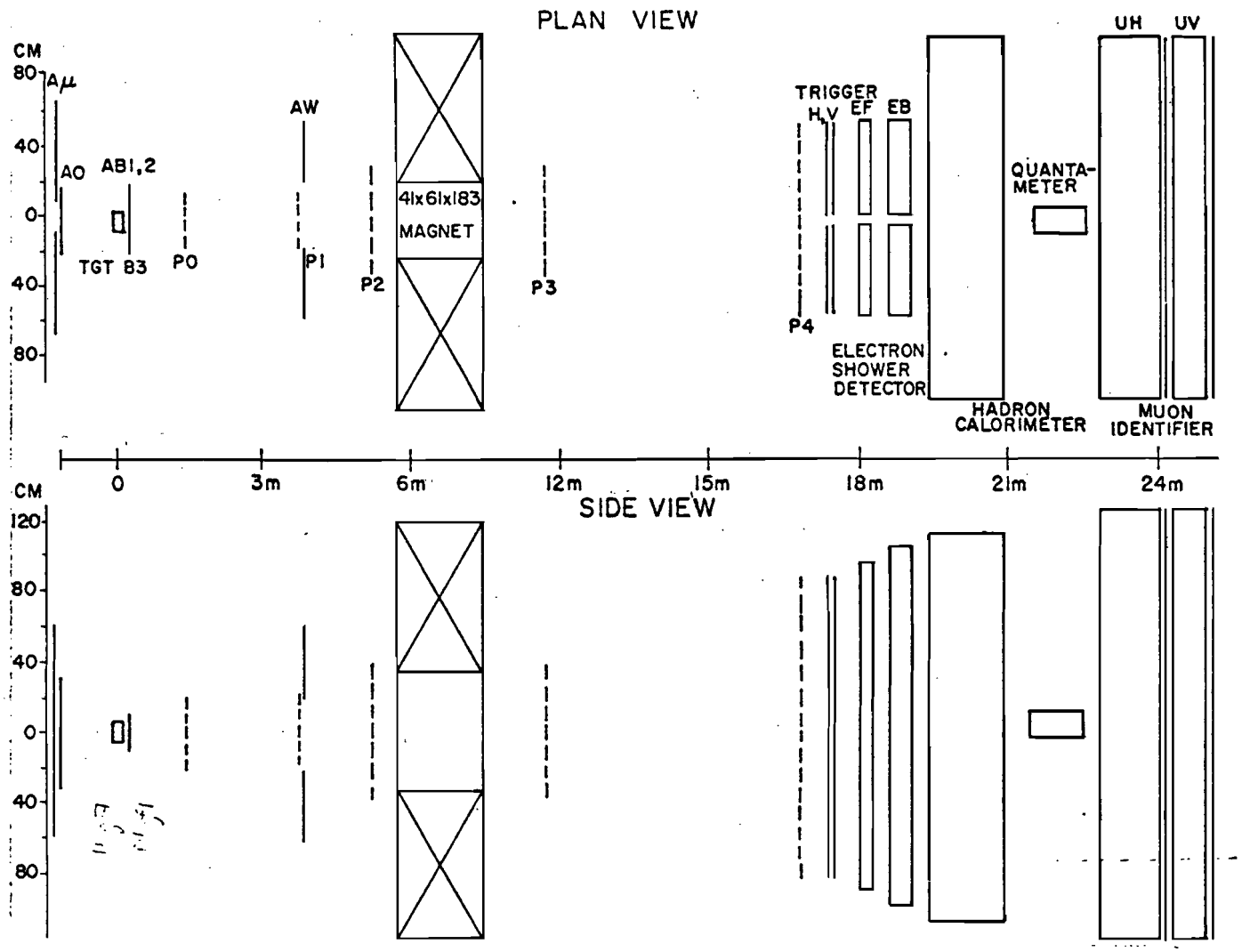
PLAN VIEW
CM
80
40
0
40
80
Aμ
AO
AB1,2
TGT B3
PO
AW
P1
P2
4Ix6Ix183
MAGNET
P3
TRIGGER
H,V
EF
EB
P4
ELECTRON
SHOWER
DETECTOR
QUANTA-
METER
HADRON
CALORIMETER
UH
UV
MUON
IDENTIFIER
0
3m
6m
12m
15m
18m
21m
24m
SIDE VIEW
CM
120
80
40
0
40
80

Fig. 5. Apparatus. Another view showing the horizontal bending magnet M1 used for shower detector calibration and photon spectrum measurement.

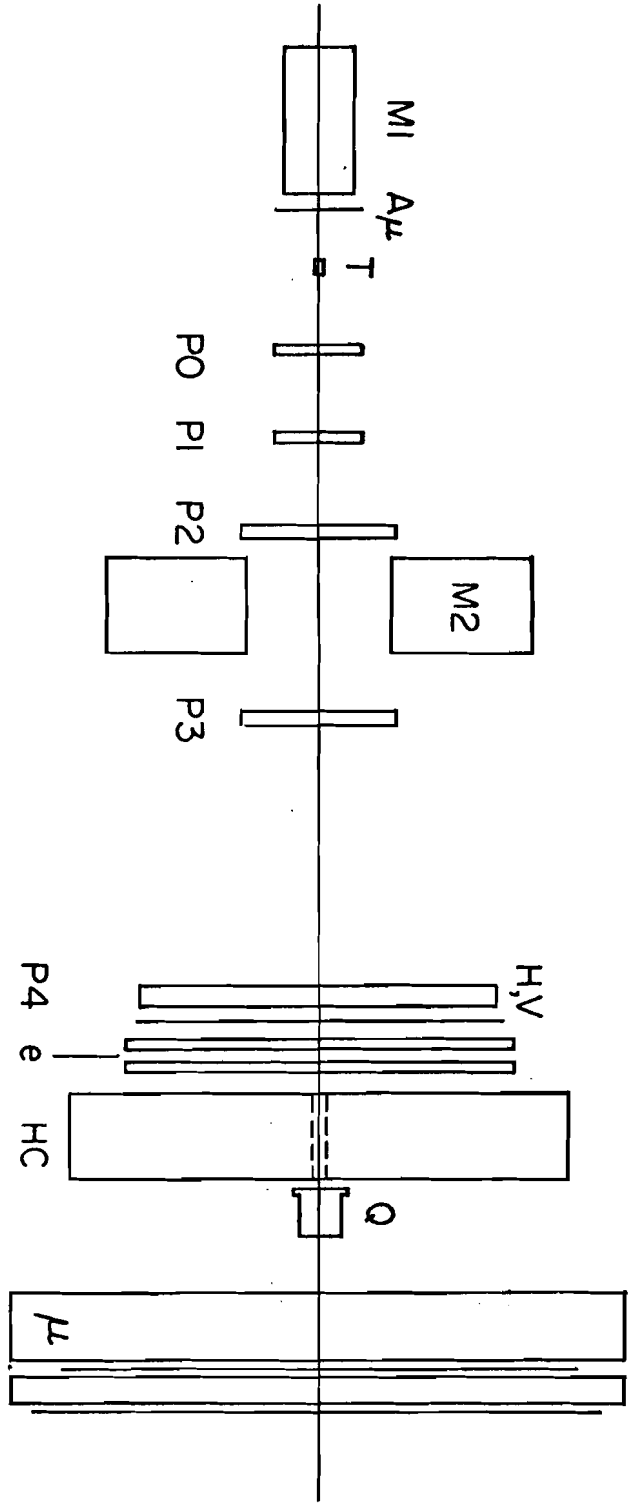
M1
Aμ
T
P0
P1
P2
M2
P3
H,V
P4
e
HC
Q
μ

Fig. 6. Apparatus. Details of a PWC. Only a few of the amplifier cards, trigger mixers, and central wires are shown. The V and U planes are crossed at an angle $\theta = \tan^{-1}(0.2) = 11°$ to the horizontal.

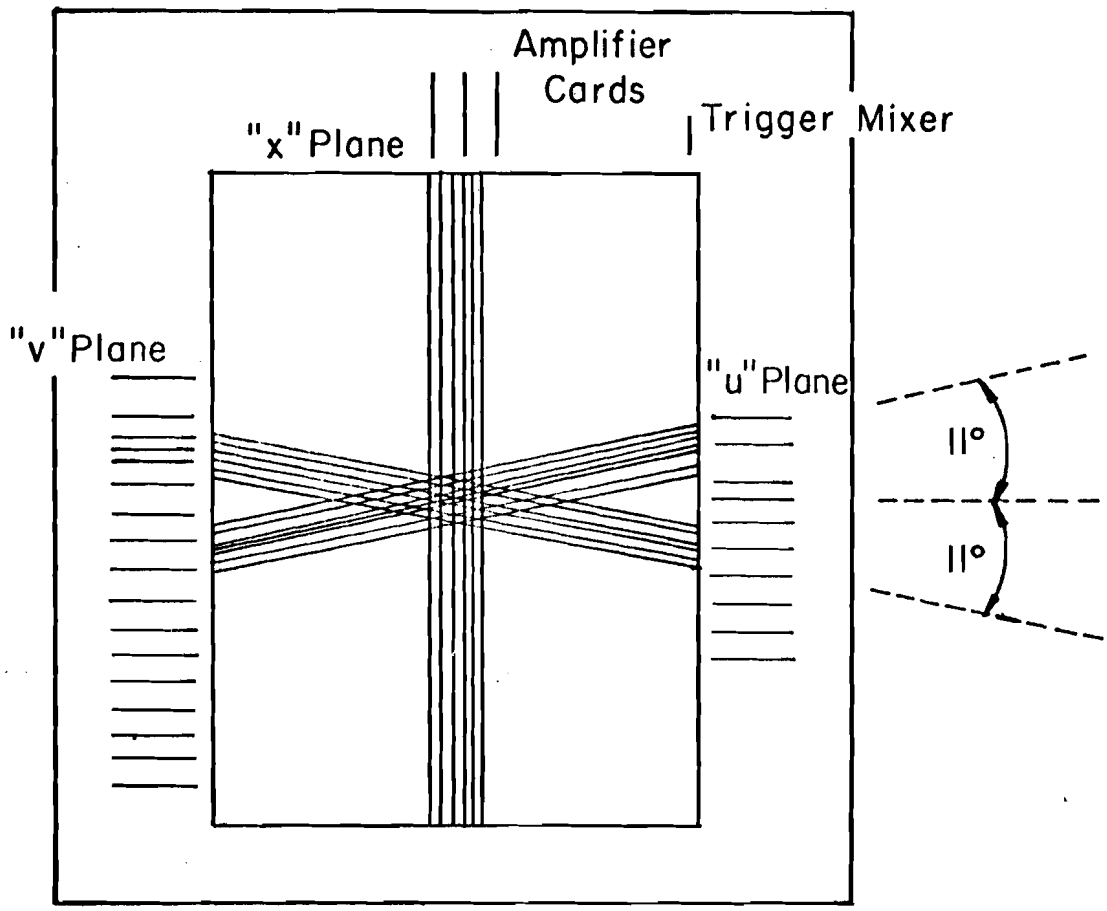
Amplifier
Cards
"x" Plane
Trigger Mixer
"v" Plane
"u" Plane
11°
11°

Fig. 7. Apparatus. Details of arrangement of T, AB, B3 and AW counters.

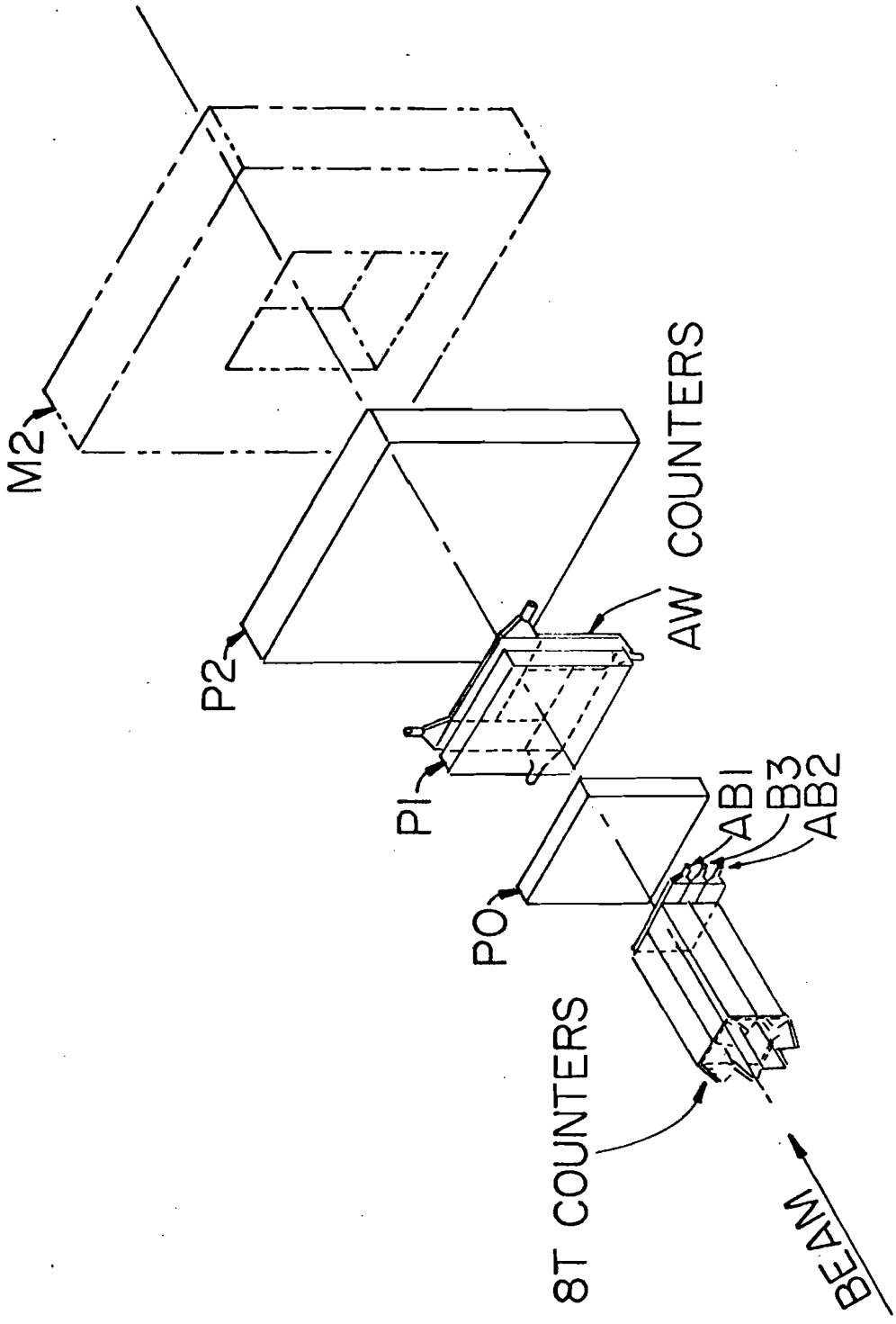
M2
P2
AW COUNTERS
PI
PO
AB1
B3
AB2
8T COUNTERS
BEAM

A0, which is 1.6 mm thick, 41 cm wide, and 61 cm long. The remaining counters in this plane are 6.4 mm thick by 20 cm wide, and 122 cm long.

Surrounding the target box are scintillation counters known as the T counters which detect the emission of particles at large angles. The T counters are mounted parallel to the beam with two counters on each side of the box. One radiation length of lead is mounted next to the T counters to convert any photons or π°'s which may come from the target.

Immediately following the target box are three more plastic scintillator counters. These counters are mounted horizontally in a vertical plane; they are 1.6 mm thick, 7.6 cm wide, and 38 cm long. The counter in the middle, B3, is used to trigger on charged particles that leave the target in the forward direction. The other two counters, AB1 and AB2, are mounted above and below B3 and are used to signal an event with one or more particles emitted at large angles. We refer to such events as being non-diffractive events.

Four more anti-counters, AW1, AW2, AW3 and AW4, surround the active area of the second PWC, P1. These counters which are each 6.3 mm thick, 41 cm wide, and 66 cm long, are also used to veto non-diffractive events.

Finally, immediately behind P4 are the H and V counters. These counters are used to trigger the rest of the apparatus. Signals from these counters, along with B3, determine what is called the master gate. Electronic decisions are made on the signals of these counters to trigger on either two or more

Fig. 8. Apparatus. Details of the A0, A_μ anti-counters mounted upstream of the target. Also shown is the H, V trigger array mounted downstream of P4.

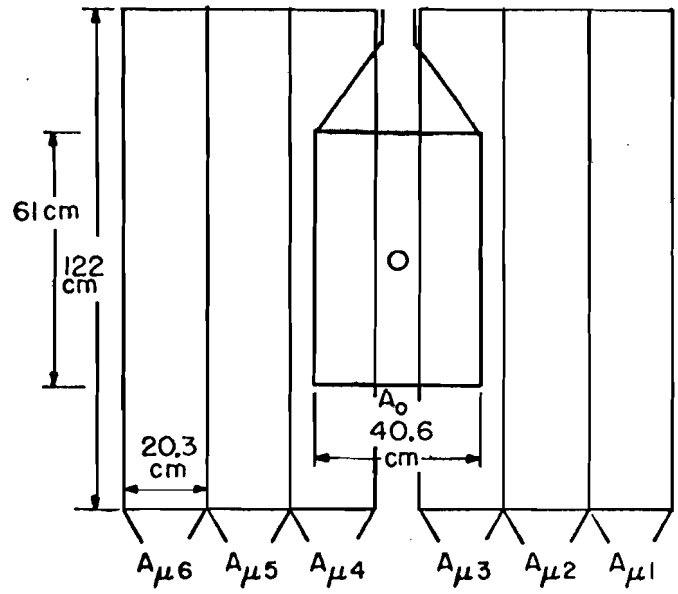
61 cm
122 cm
O
A_o
40.6 cm
20.3 cm
$A_{\mu 6}$
$A_{\mu 5}$
$A_{\mu 4}$
$A_{\mu 3}$
$A_{\mu 2}$
$A_{\mu 1}$

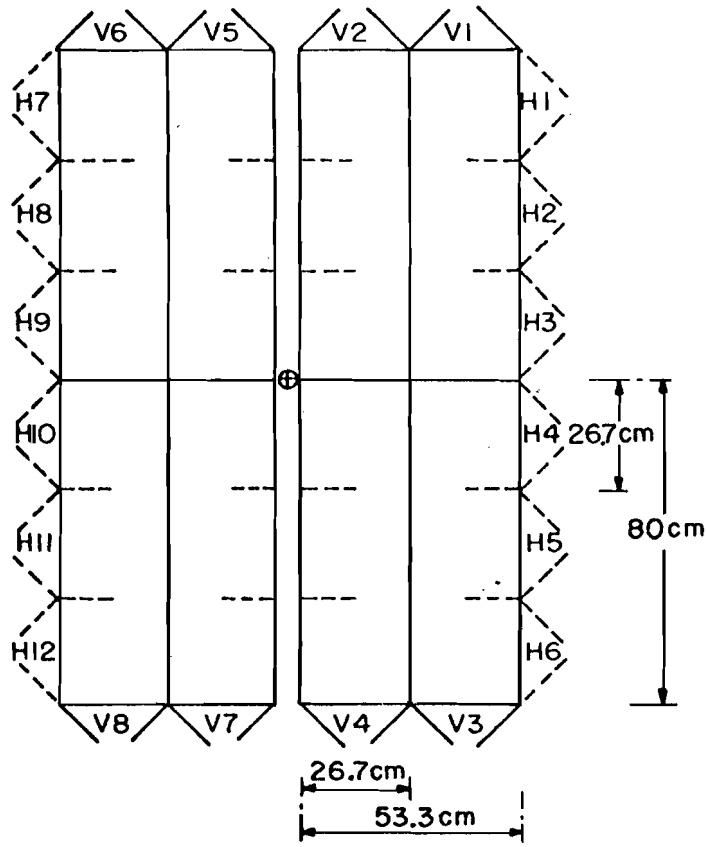
V6
V5
V2
V1
H7
H8
H9
H10
H11
H12
H1
H2
H3
H4
H5
H6
26.7cm
80cm
V8
V7
V4
V3
26.7cm
53.3cm

charged particles in the apparatus. (See Sec. II. C.) These counters are mounted in two planes. The H plane, mounted horizontally, consists of twelve counters (H1 through H12), six on either side of the beam line. The H counters are 1.6 mm thick, 27 cm wide, and 53 cm long. There are eight V counters (V1 through V8) which are mounted vertically directly behind the H counters. The V counters are 1.6 mm thick, 27 cm wide, and 80 cm long. Both the H and V counters are mounted on a track which allows the counters to be rolled apart horizontally making a vertical slit at the center. This vertical slit allows the non-interacting beam and the copiously produced electron pairs to pass through the H, V array without triggering the apparatus. Since these low mass electron pairs were of no interest in this experiment, the slit was normally opened to about 5 cm to reduce this background.

The particle identifying system consists of three sets of detectors. These are the shower detectors, the hadron calorimeter, and the muon identifier. The shower detectors identify electrons and electromagnetic showers and measure the energy of the showers to about 10%. The hadron calorimeter identifies hadrons and measures their energy. The muon identifier does just what its name implies; however, no energy measurement of the muons is made. All of these detectors in the particle identification system are of very large dimensions. They involve several tons of lead and steel, and many square feet of plastic scintillators.

The shower detector array consists of forty-six counters

arranged in four banks; two on either side of the beam. The counters are mounted horizontally with eleven counters in the front bank and twelve counters in the back bank on both sides of the beam. The counters themselves consist of lead-scintillator sandwiches. The front counters contain six radiation lengths of lead and six sheets of plastic scintillator, while the back counters contain sixteen sheets each of lead and scintillator. The scintillator is 4.8 mm thick, 15 cm wide, and 51 cm long. The electromagnetic showers which develop in the lead are sampled after each radiation length by the scintillator. The scintillators are glued to light pipes which are bent and fanned into one 6.2 cm polished lucite mixing block. The mixing block is in turn glued to a 12 cm phototube, Amperex 58-AVP.

Light collection uniformity and linearity provided some problems. Non-uniformity arose in two ways. One, along the 51 cm length of the scintillator, and two, across the 12 cm face of the phototube. Non-uniformity in the scintillator arises from the fact that scintillation light is re-absorbed by the scintillating centers in the plastic. This amounts to approximately a 15-20% effect from one edge of the scintillator to the other. By adding reflecting surfaces around the scintillator sheets, the loss of light from distant locations is reduced. The reflecting material that was used was Alzac aluminum which also increased the strength of the plastic sheets. However, there is still an increase in light levels from locations very near the phototube. This effect was overcome by gluing a yellow (Wratten #4) filter between the

phototube and the mixing block. The light which is readily re-absorbed by the scintillating centers is violet to UV; however, the yellow light is transmitted with little attenuation. Hence, light from near or far positions in the scintillator would produce equal signals, to about 5%, from the phototube. The yellow filter, of course, attenuated the amount of light reaching the phototube, but the enormous amount of light emitted by the showering particles was such that it did not matter. The tube base was designed to give maximum uniformity and linearity (Appendix II). The variable resistors on the focusing grid and the first dynode were adjusted for each phototube and its base to give the best response. The phototube was glued to the counter such that the axis of maximum uniformity was parallel to the axis of shower development. Along the perpendicular axis, light rays were "mixed" in the light pipe as well as in the mixing block. In this manner, non-uniformities of 30% across the face of the phototube were reduced to about 5%.

Signals from the shower detectors were integrated by analog to digital converters (ADC's). The area under the pulse is proportional to the energy of the shower. The shower detector high voltages were set to give equal gain from each phototube. The detectors were calibrated with electrons by a method described in Sec. II. D. and were found to give a resolution (FWHM) for electrons of energy E:

$$\frac{\Delta E}{E}\ (\%) = \frac{39}{\sqrt{E}} + 2.6. \qquad (15)$$

Fig. 9. Apparatus. Electromagnetic shower detectors. The front banks of counters (EF1-22) left and right are shown. These counters contain $6X_0$ of Pb and six sheets of plastic scintillator. The twenty-four back counters (EB1-24) are mounted 30 cm downstream from the EF counters. The EB counters contain $16X_0$ of Pb and sixteen sheets of plastic scintillator.

Shower Detectors

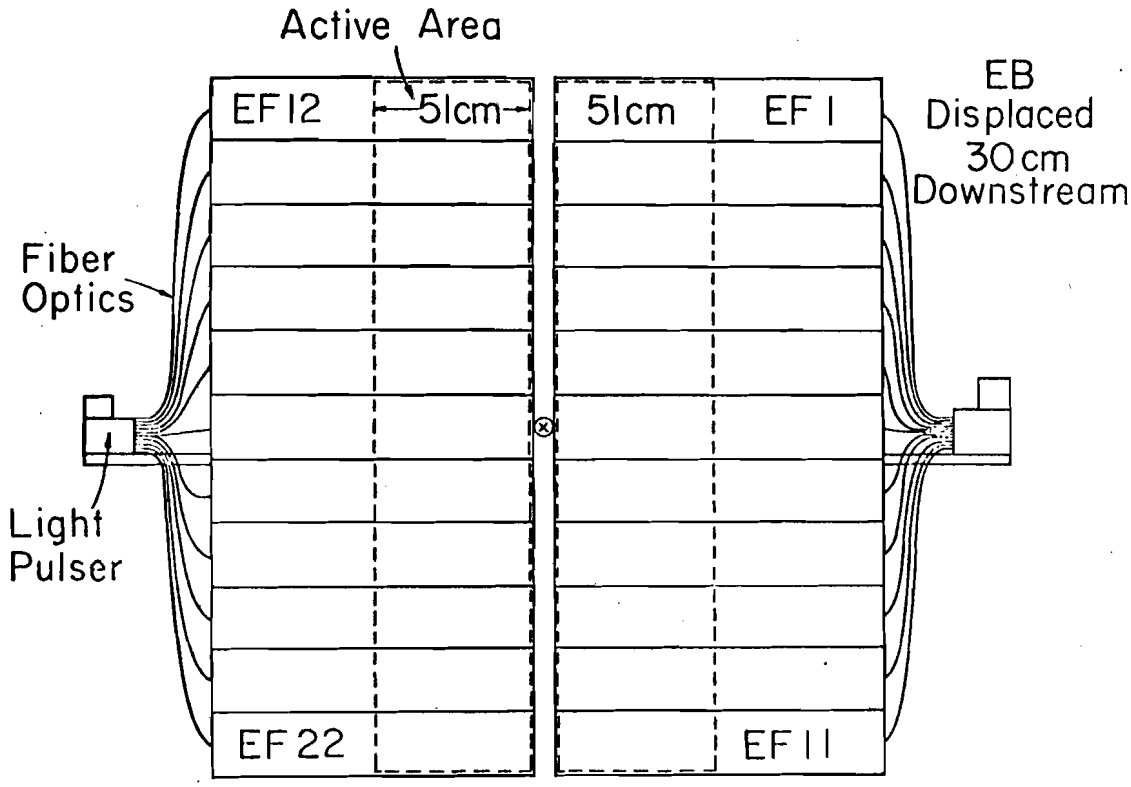

Cutaway $6X_0$ Detector

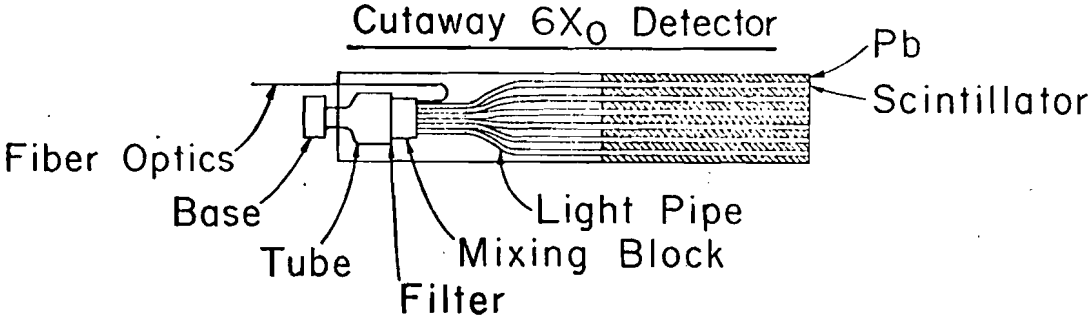

Fig. 10. Apparatus. Arrangement of hadron calorimeter counters. The front ten counters are shown.

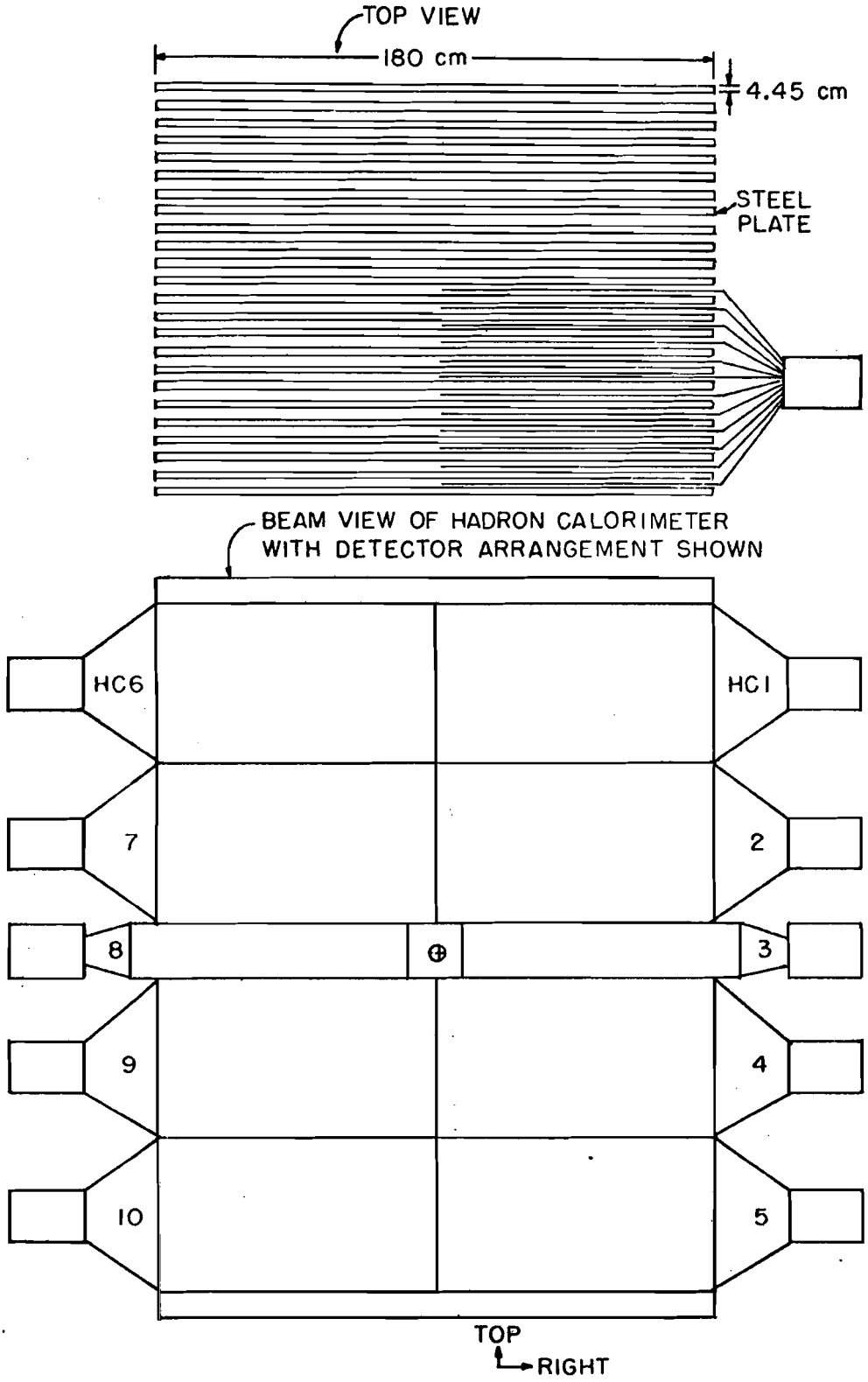
TOP VIEW
180 cm
4.45 cm
STEEL PLATE
BEAM VIEW OF HADRON CALORIMETER WITH DETECTOR ARRANGEMENT SHOWN
HC6
HC1
7
2
8
3
9
4
10
5
TOP
RIGHT

Fig. 11. Apparatus. Details of a large hadron calorimeter counter showing the twelve sheets of plastic scintillator and the optical couplings to the phototube.

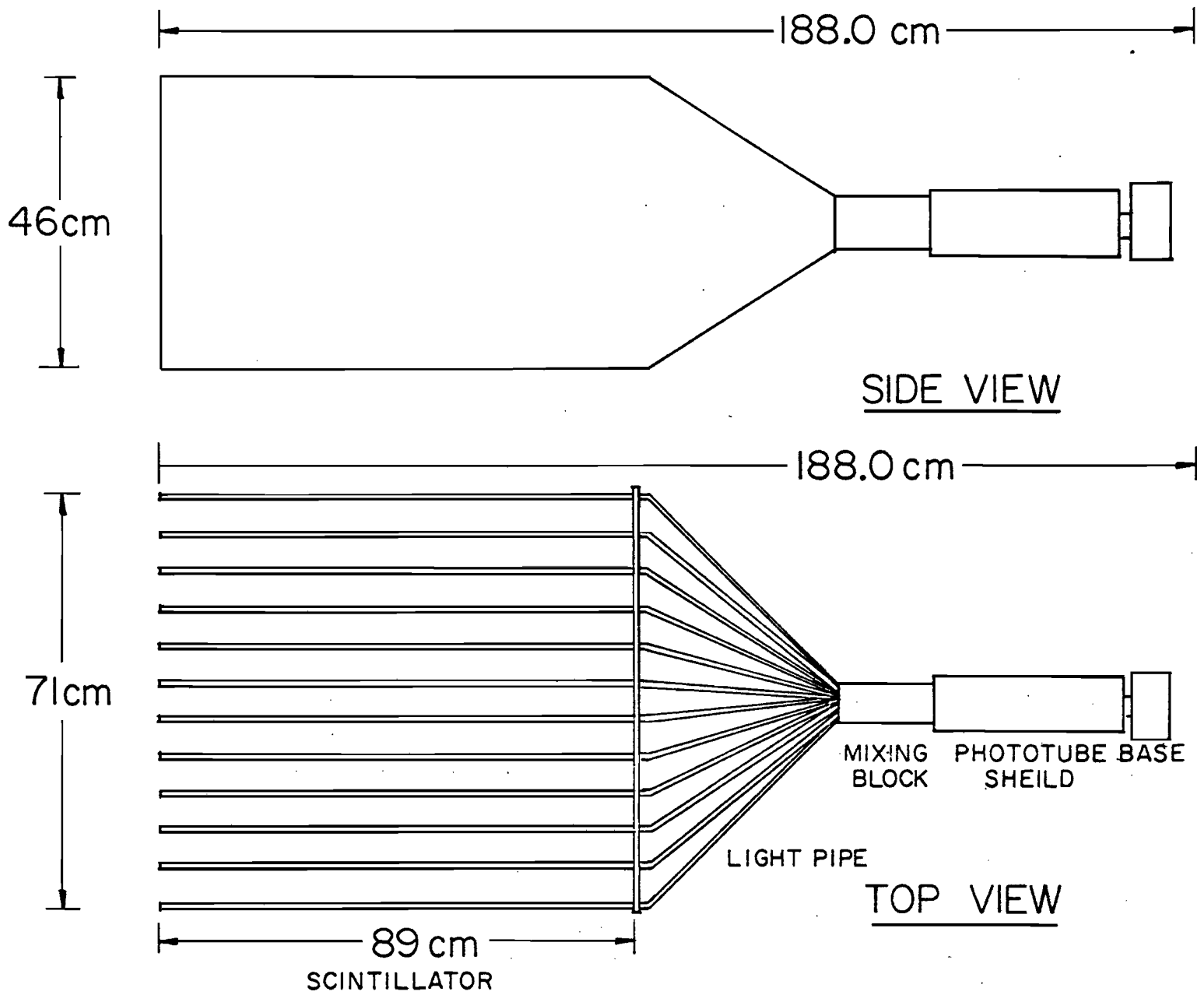
188.0 cm
46cm
SIDE VIEW
188.0 cm
71cm
MIXING BLOCK
PHOTOTUBE SHEILD
BASE
LIGHT PIPE
TOP VIEW
89 cm
SCINTILLATOR

Fig. 12. Apparatus. Muon identifier array showing the 22 μH counters mounted behind 122 cm of steel and the 18 μV counters mounted behind another 61 cm of steel.

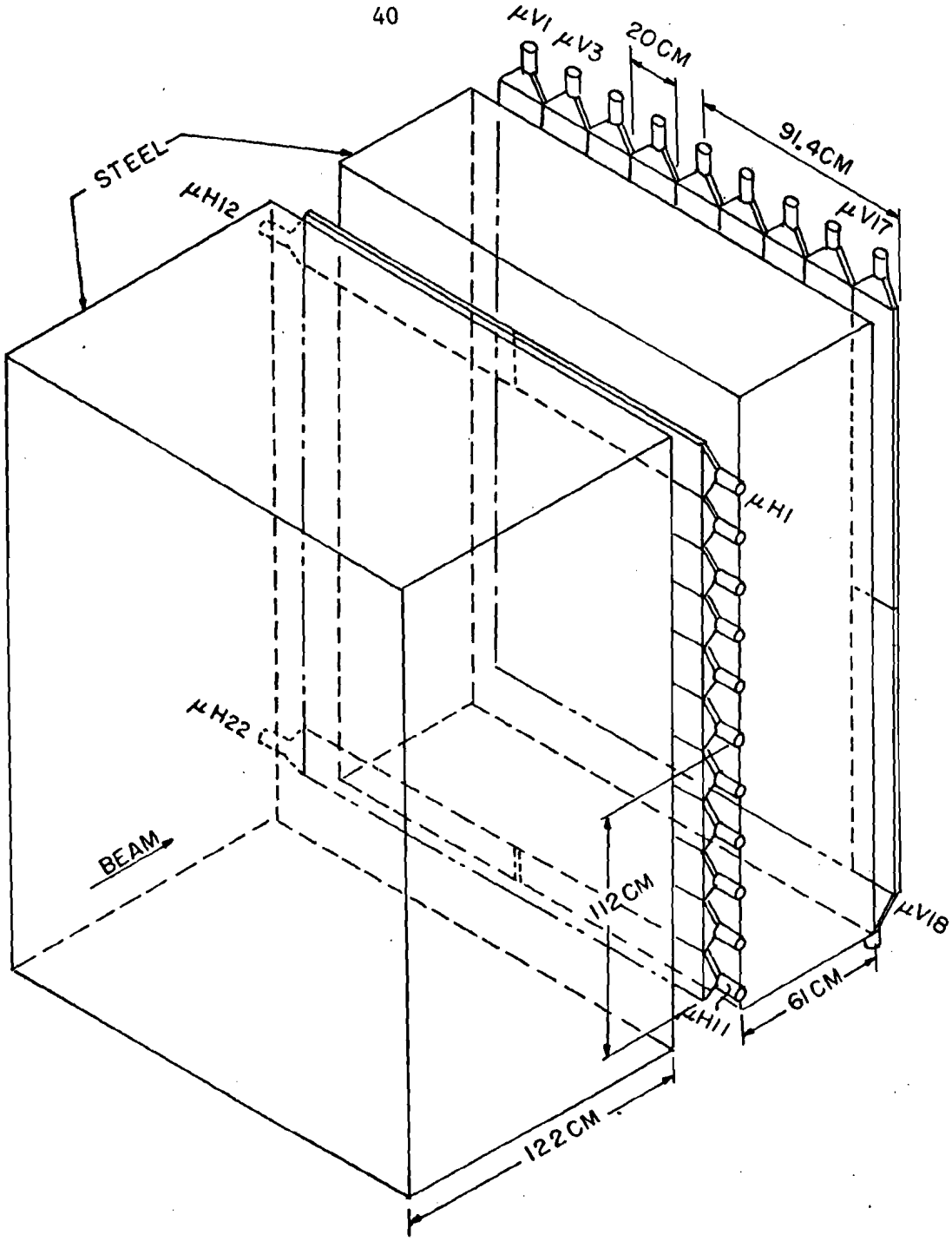
μV1
μV3
20CM
91.4CM
μV17
STEEL
μH12
μH1
μH22
BEAM
112CM
μV18
61CM
μH11
122CM

A calibration run was taken at least once a week to monitor the performance of the shower detectors. Furthermore, a light pulser was flashed during each run to monitor the gain and stability of the detectors (Appendix II).

Following the shower detectors is a column of lead 15.4 cm thick which covers the vertical slit between the detectors. Its purpose is to stop small angle electron pairs before they enter the hadron calorimeter. The column is divided into two halves, top and bottom, with a gap in between to allow non-interacting beam to pass through.

The hadron calorimeter consists of a steel-scintillator sandwich (Figs. 10,11). There are twenty-four sheets of steel 180 cm wide, 200 cm high and 4.5 cm (0.5 absorption lengths) thick. In the center of each sheet is a 15 cm square hole which allows the beam to pass through. There are twenty calorimeter counters (only sixteen were in operation in this experiment), ten mounted on each side of the beam. The counters are stacked five high vertically, and two deep longitudinally, sixteen of the twenty counters have twelve sheets each of plastic scintillator 89 cm long, 46 cm wide, and 6.3 mm thick. All twelve sheets are fanned together with light pipes to a mixing block and filter and are viewed by a single 58 AVP phototube. The remaining four counters consist of twelve sheets of plastic scintillator 89 cm long, 15.2 cm wide, and 6.3 mm thick. The light collection is achieved in the same way as the larger counters. These four counters are mounted in the array at beam height. The calorimeter counters are mounted to the

steel plates themselves. Light collection uniformity is accomplished in the same way as with the shower detectors. Each sheet of scintillator is, however, wrapped with aluminum foil instead of Alzac. Tubes and bases were also set for maximum uniformity and linearity in the same way the shower detectors were done. Again the anode signals are integrated by ADC's. The resolution for a 50 GeV/c pion beam was found to be 30% FWHM.[34]

The last piece of apparatus in the particle identification system is the muon identifier. It consists of two large blocks of steel and two planes of plastic scintillation counters. The first block of steel is 122 cm long, 183 cm wide, and 224 cm high. Following this block are twenty-two horizontally mounted counters, each 91 cm long, 20 cm wide, and 6.3 mm thick. Eleven counters are on the left, μH 1-11, and eleven counters on the right μH 12-22. The second block of steel is 61 cm thick, 183 cm wide, and 224 cm high. Mounted behind this block are the vertical muon counters μV 1-18. These counters are each 122 cm long, 20 cm wide, and 6.3 mm thick. Anode signals from these counters set DC latches and form the logic for muon triggers. The dynode signals from these counters and all other arrays of counters except the shower counters and hadron calorimeter counters were summed passively and integrated by ADC. This pulse height measurement was a monitor of the performance of the counters.

One final element in the apparatus was the Wilson compensating quantameter used to measure beam power ($\int \frac{dN}{dK}\, dK$). The quantameter is a copper plate electromagnetic shower device.

Beam showers ionized the hydrogen gas in the quantameter and deposited electrons on the copper plates held at high positive voltage. There are forty-four plates each 1.45 cm thick. Current from the charge deposited on the plates was integrated over the entire beam spill. The total charge deposited is then proportional to the total beam power; the conversion factor, c, being

$$c = 416 \text{ ion/GeV}. \tag{16}$$

The quantameter was calibrated and the conversion factor determined at SLAC.[35] This device was used as a beam monitor and for normalization in the calculation of cross sections.

C. Electronics

The function of the electronics in the experiment was to receive signals from the various detectors, digitize or integrate them, make logic decisions, and send the data to the computer (Xerox Data Systems Σ2) which ultimately wrote the data on magnetic tape. The electronics may be broken into several functions: triggering, integrating, and recording of proportional wire chamber (PWC) wires. The devices which implement these functions include: master gate (MG), input trigger generator (TGI), output trigger generator (TGO), analog to digital converters (ADC's), coincidence registers (CR's), sum logic, pin logic, PWC registers and encoders, and interfaces. A block diagram of the electronics is shown in Fig. 13. The functions of the components in this diagram are detailed in this sub-section and in Figs. 13-25. (We remind the reader to consult the glossary for terms and symbols used in this section.)

Fig. 13. Electronics. Block diagram of data taking electronics.

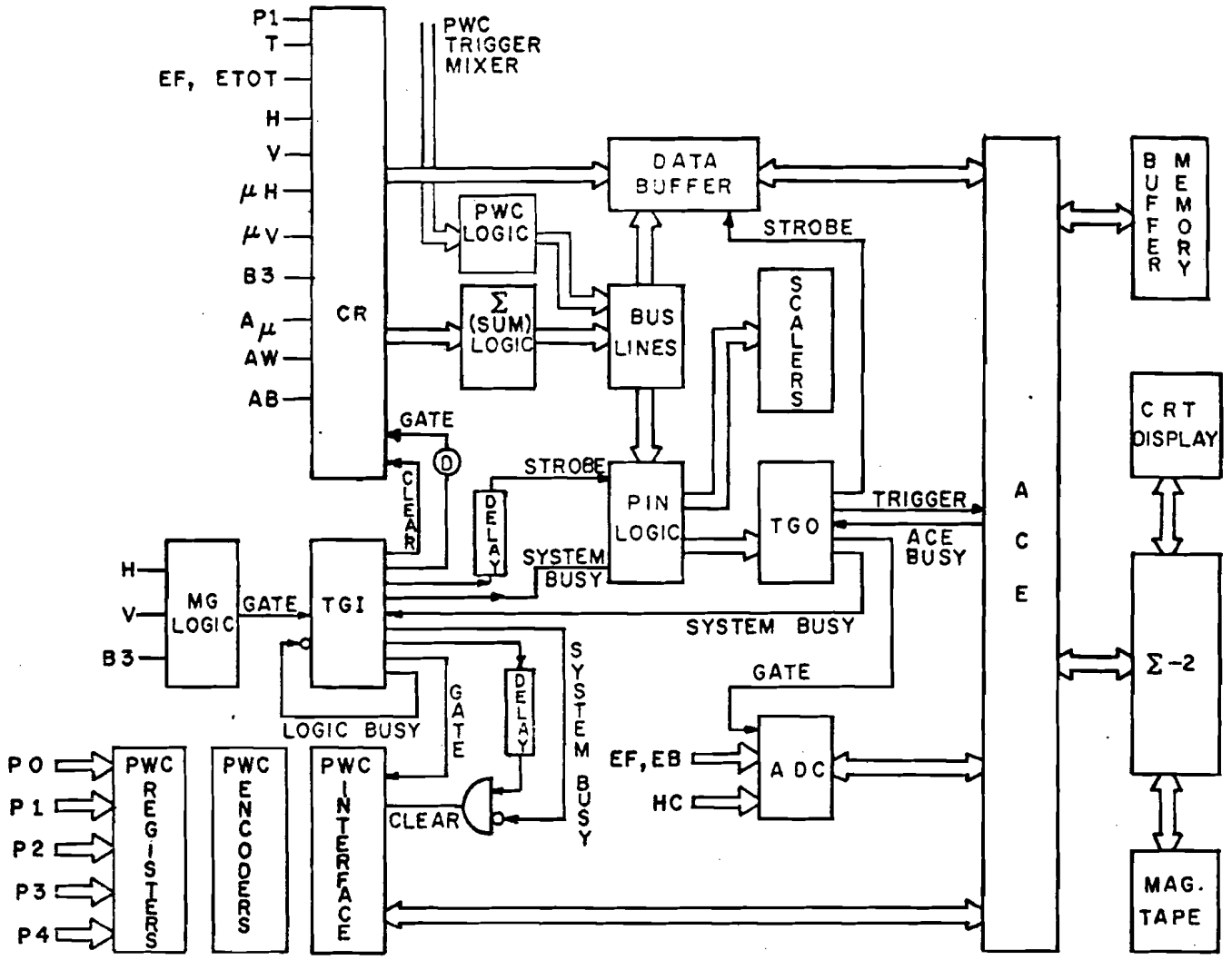
P1
T
EF, ETOT
H
V
μH
μV
B3
Aμ
AW
AB
CR
PWC TRIGGER MIXER
DATA BUFFER
PWC LOGIC
Σ (SUM) LOGIC
BUS LINES
SCALERS
STROBE
GATE
CLEAR
DELAY
STROBE
PIN LOGIC
TGO
TRIGGER
ACE BUSY
SYSTEM BUSY
SYSTEM BUSY
H
V
B3
MG LOGIC
GATE
TGI
LOGIC BUSY
GATE
DELAY
SYSTEM BUSY
CLEAR
GATE
EF, EB
HC
ADC
P0
P1
P2
P3
P4
PWC REGISTERS
PWC ENCODERS
PWC INTERFACE
ACE
BUFFER MEMORY
CRT DISPLAY
Σ-2
MAG. TAPE

The master gate (MG) was designed to be a rather loose two-particle trigger. The MG, generated by fast logic, gated all other electronics. Decisions are later made by the sum logic and the pin logic (DC) to refine this loose trigger before an event is read or written on tape. The master gate was

$$MG = B3 \cdot (L + R) > 1$$

where (L + R) is defined as at least one hit (two overlapping counters firing) on the left side of the trigger array (H, V) in conjunction with one or more hits on the right; or two or more hits on either the left or the right side (Figs. 8, 14). From Fig. 14 it is clear that

$$(L + R) > 1 = \{(H) > 0 \cdot (V) > 1\} + \{(H) > 1 \cdot (V) > 0\}.$$

In other words, a minimum of three counters in the trigger array are required to fire since two particles could go through the same H (V) counter but then must go through two different V (H) counters. The requirement for B3 insures that the particles came from the target. The output of the master gate is scaled, recorded, and triggers the TGI.

The trigger input generator (TGI) makes no further decisions on the master gate except to inhibit itself for a set deadtime (logic deadtime, not to be confused with computer deadtime) of 100 nsec. The TGI then generates a clear and a delayed gate to the CR's, a strobe to the pin logic, gates to the PWC, and passes through the MG to the pin logic all with deadtime included (Fig. 15). Master gate and master gate logic busy are scaled for normalization purposes.

Fig. 14. Electronics. Derivation of master gate from B3, H and V counters.

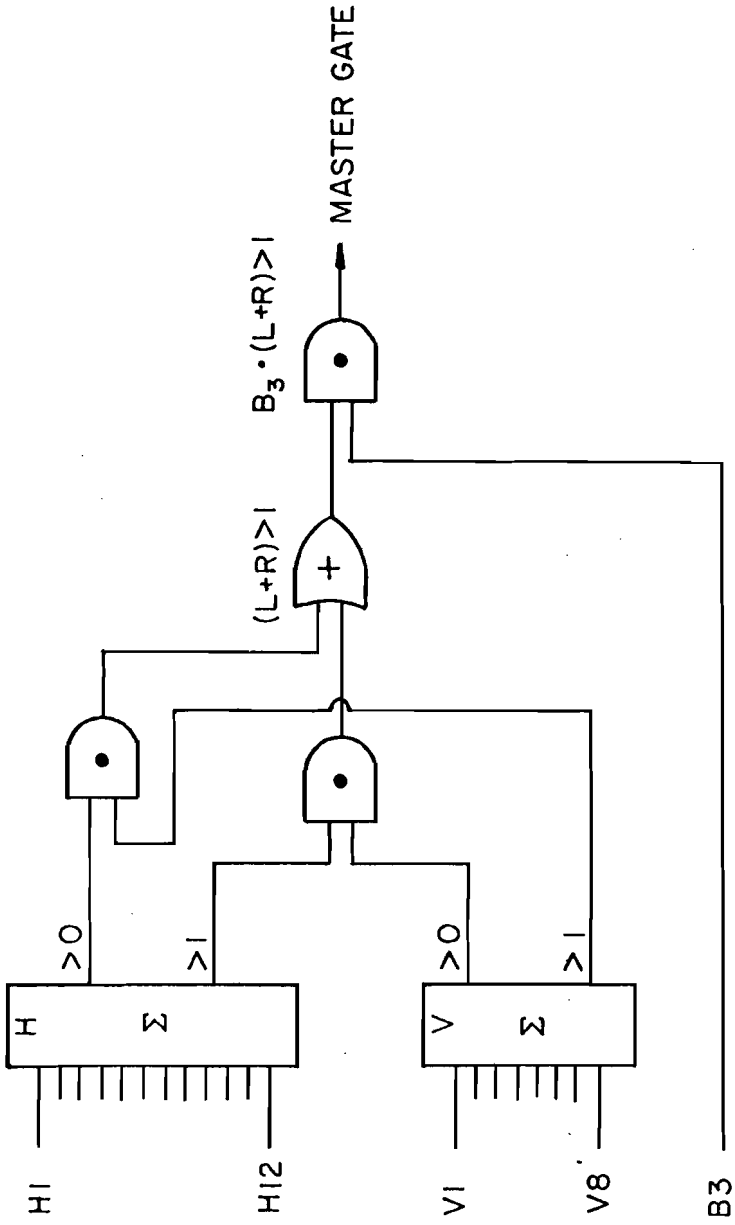
MASTER GATE
$B_3 \cdot (L+R) > 1$
$(L+R) > 1$
+
H
Σ
V
Σ
>0
>1
>0
>1
H1
H12
V1
V8
B3

Fig. 15. Electronics. Input trigger generator (TGI) is triggered by the master gate, and in turn gates the remainder of system. Logic and system busy deadtimes are also passed along.

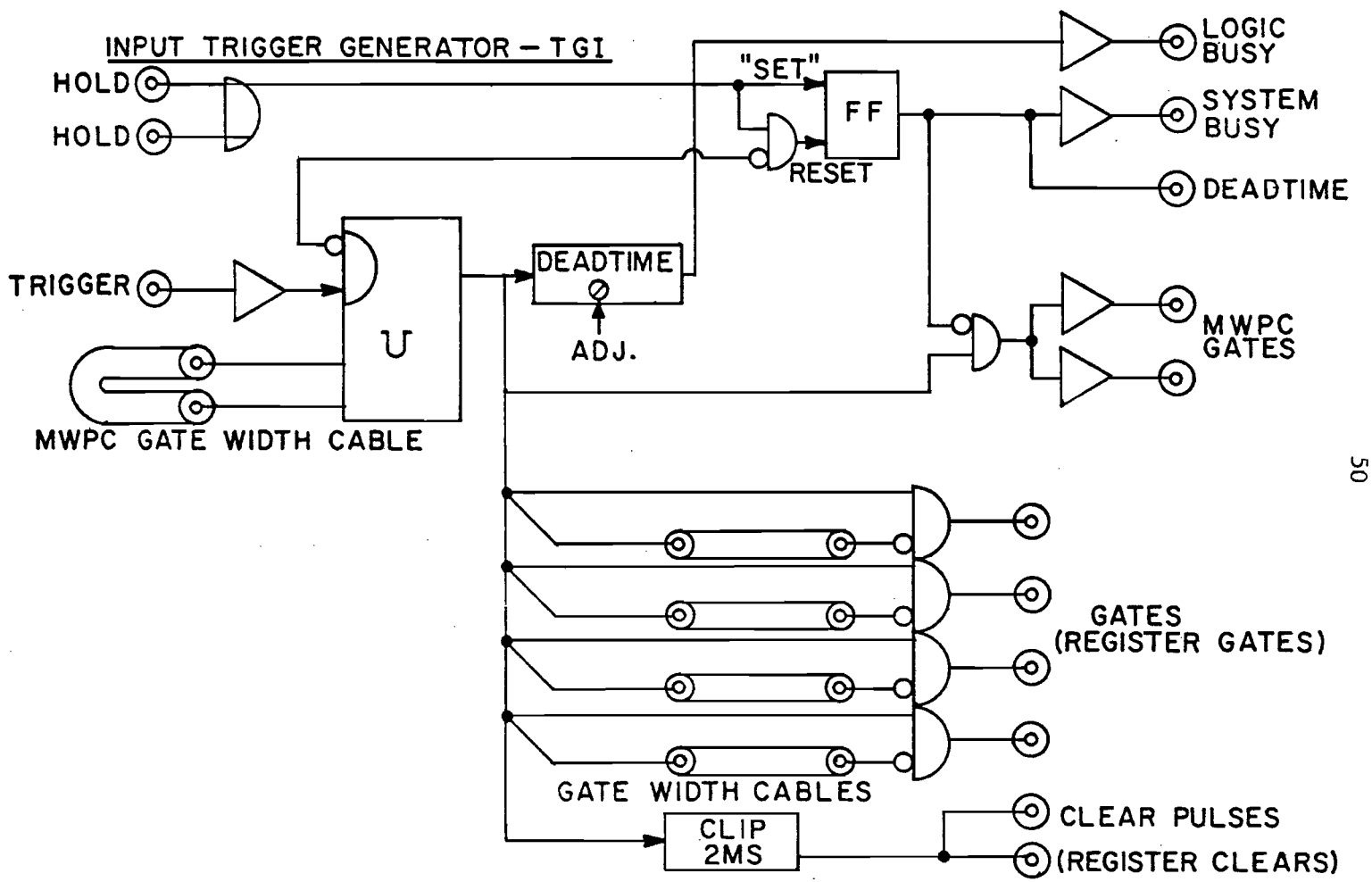
INPUT TRIGGER GENERATOR – TGI
HOLD
HOLD
"SET"
FF
RESET
LOGIC BUSY
SYSTEM BUSY
DEADTIME
TRIGGER
U
DEADTIME
ADJ.
MWPC GATES
MWPC GATE WIDTH CABLE
GATES (REGISTER GATES)
GATE WIDTH CABLES
CLIP 2MS
CLEAR PULSES
(REGISTER CLEARS)

Fig. 16. Electronics. Coincidence register (CR). Inputs to the CR are the clear and gate from the TGI and up to eight counter signals. In this CR the outputs (DC) are two sums of four of the input counter signals.

8 FOLD COINCIDENCE REGISTER TYPE B-(SPLIT Σ OUTPUTS)

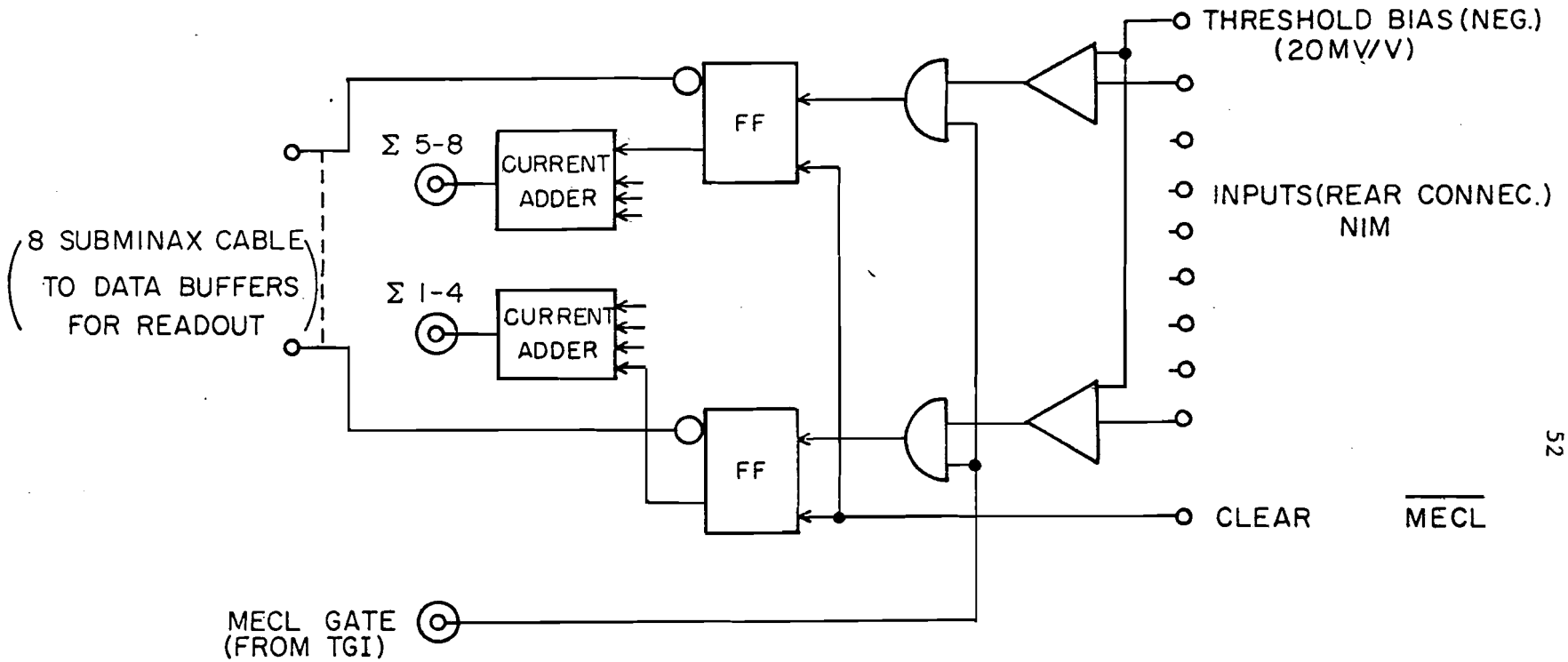

Fig. 17. Electronics. Sum (Σ) logic module. Inputs are DC currents from the CR's. Threshold comparators determine the number of latches that have been set (i.e., the number of counters which have fired).

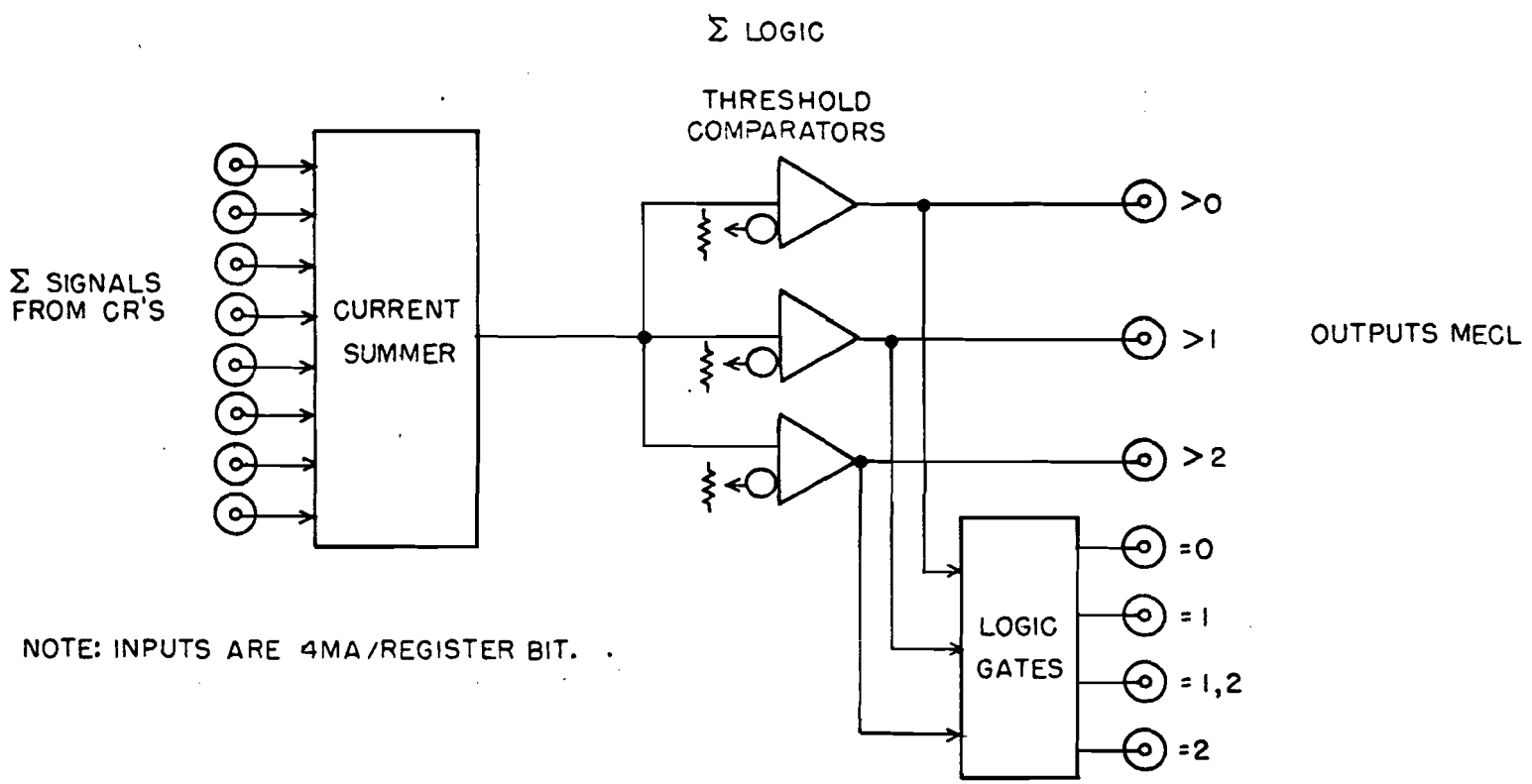

NOTE: INPUTS ARE 4MA/REGISTER BIT.

Fig. 18. Electronics. Derivation of 2π buss line from L x R and H x V logic.

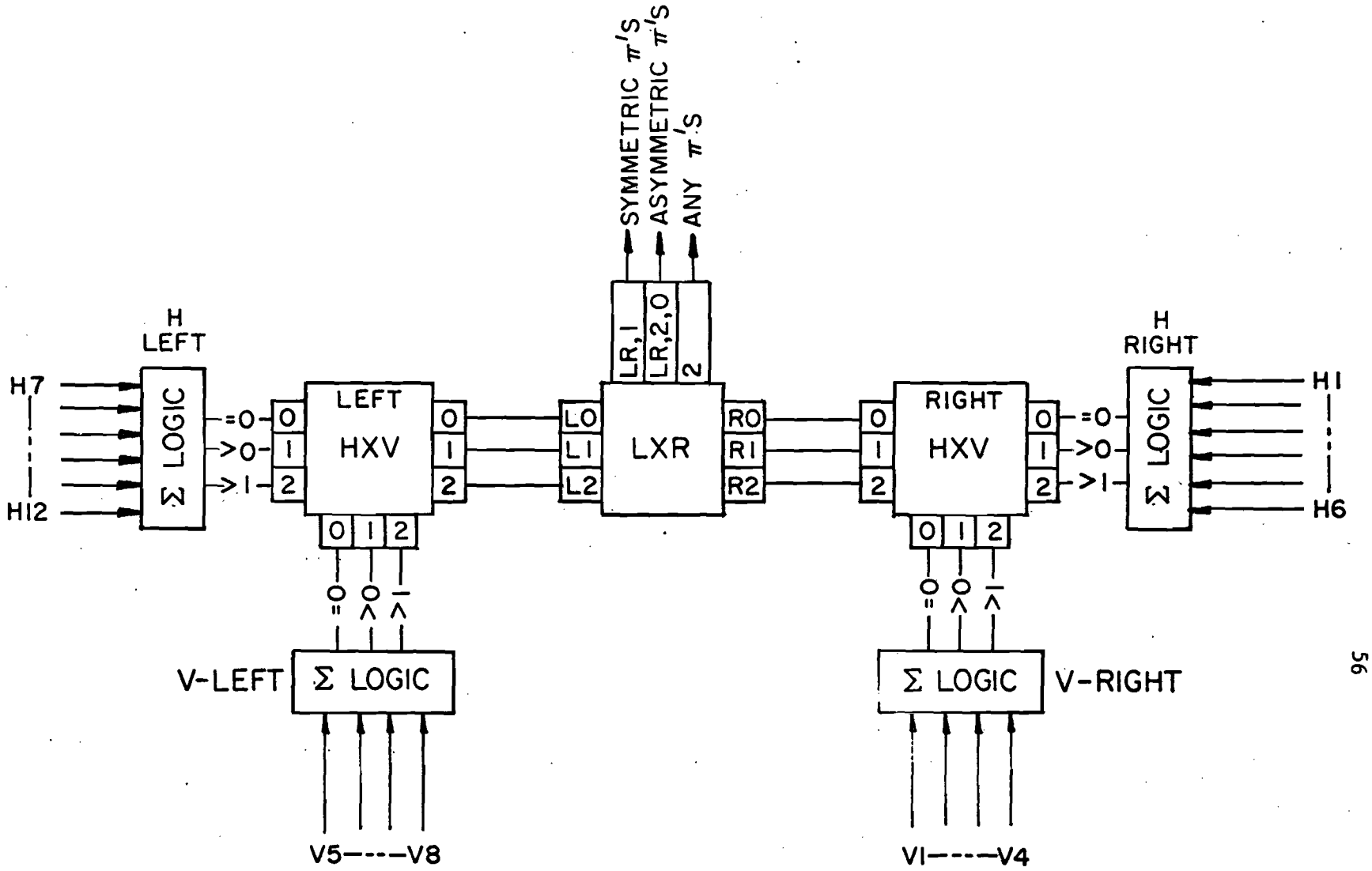
SYMMETRIC π'S
ASYMMETRIC π'S
ANY π'S
LR,1
LR,2,0
2
H
LEFT
H7
H12
Σ LOGIC
=0
>0
>1
0
1
2
LEFT
HXV
0
1
2
0 1 2
=0
>0
>1
V-LEFT
Σ LOGIC
V5----V8
L0
L1
L2
LXR
R0
R1
R2
0
1
2
RIGHT
HXV
0
1
2
0 1 2
=0
>0
>1
Σ LOGIC
V-RIGHT
V1----V4
H
RIGHT
Σ LOGIC
H1
H6

The coincidence registers (CR's) generate DC latches. Up to eight fast input signals are sent to each CR from the various arrays of scintillation counters. A clear pulse from the TGI arrives just prior to the arrival of the gate, signals arriving in time with the TGI gate latch the C R on, which depending on the CR card, indicates the firing of one or the sum of several counters (Fig. 16). The DC output current is proportional to the number of counters that have fired. The outputs of the CR's go to the sum (Σ) logic and to the CR buffer. The sum logic units are DC current comparators whose outputs indicate the number of latches set (=0, >0, >1, etc.) (Fig.17). This information is then either:

1. Sent directly to the pin logic buss lines, or
2. Further decisions are made before going to the buss lines.

For example, in case (1) say one only wished to know if any of the wide anti (AW) counters fired, then the sum Σ(AW) would be sent directly to the buss line, and from the CR buffer one would know which AW counter fired. In case (2) one might wish to make a more restrictive decision as in the use of the L x R logic in the H, V trigger counters (Fig. 18). In this example one might wish to have one particle on the left side of the H, V counters and one on the right side. This information determines a two-particle (2π) trigger, again in the form of a DC level, and is sent to the buss lines.

To require the shower detectors, the hadron calorimeter, or the PWC's in the pin logic, the procedure becomes slightly different. The primary signals from these detectors go to

either the ADC's or to the PWC registers. Therefore, the dynode signals from the shower counters and the hadron calorimeter are used, and the trigger mixer signals (sum of strips of wires) from the PWC's are used. In the former case one wishes to make an energy requirement in the trigger, and in the latter one wishes to know into what region of the chamber did a particle go.

To obtain an electromagnetic shower energy trigger, first the left and right, front and back dynode signals are passively added. Then front and back on the left side as well as on the right are added (Fig. 19). These summed analog signals are then discriminated, the level of discrimination being set such that a shower of at least 3 GeV was required in the front (EFR, EFL) and 10 GeV total (ETR, ETL). The outputs of these discriminators went to CR's and the buss lines were set in the same fashion as above.

The hadron trigger was done in the same way except that all calorimeter dynode signals were passively added instead of separating them into left and right components. The hadron calorimeter discriminators were set at two levels: one very low to veto any hadron energy in electron events, and the other somewhat higher to require high energy hadrons (Fig. 20).

The PWC trigger was made from sums of wires of chambers P2 and P3 to require at least two charged particles in the apparatus before and after the magnet. Furthermore, the central sixteen wires (32 mm) in each of these planes were removed from the trigger mixer such that 0° electron pairs

Fig. 19. Electronics. Derivation of buss line 6 (EFR) and buss line 7 (ETR) from shower detector dynodes on right side. The left side (EFL, ETL) is done in the same way.

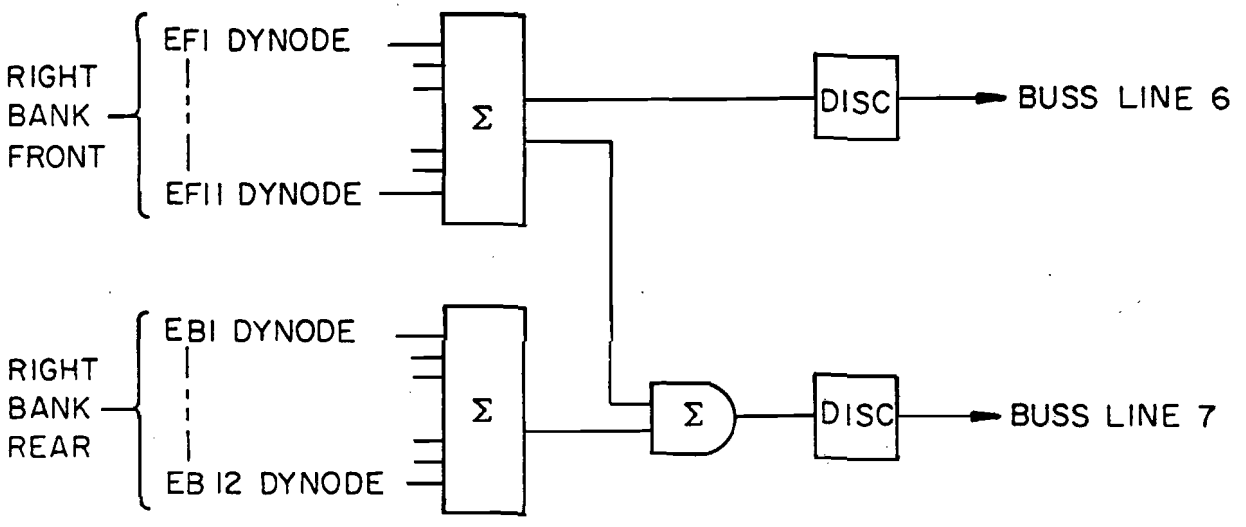
RIGHT
BANK
FRONT
EF1 DYNODE
EF11 DYNODE
Σ
DISC
BUSS LINE 6
RIGHT
BANK
REAR
EB1 DYNODE
EB 12 DYNODE
Σ
Σ
DISC
BUSS LINE 7

Fig. 20. Electronics. Derivation of buss lines 13 (HC1) and 14 (HC2) from sum of hadron calorimeter dynodes.

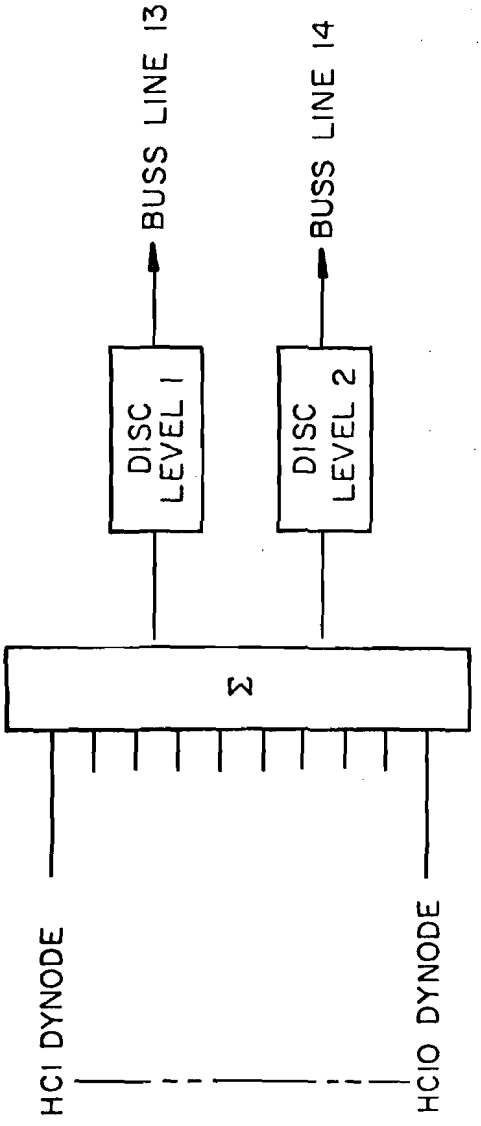
HC1 DYNODE
HC10 DYNODE
Σ
DISC LEVEL 1
DISC LEVEL 2
BUSS LINE 13
BUSS LINE 14

Fig. 21. Electronics. Derivation of buss line 15 (P1(2/3)) from P1 trigger mixers.

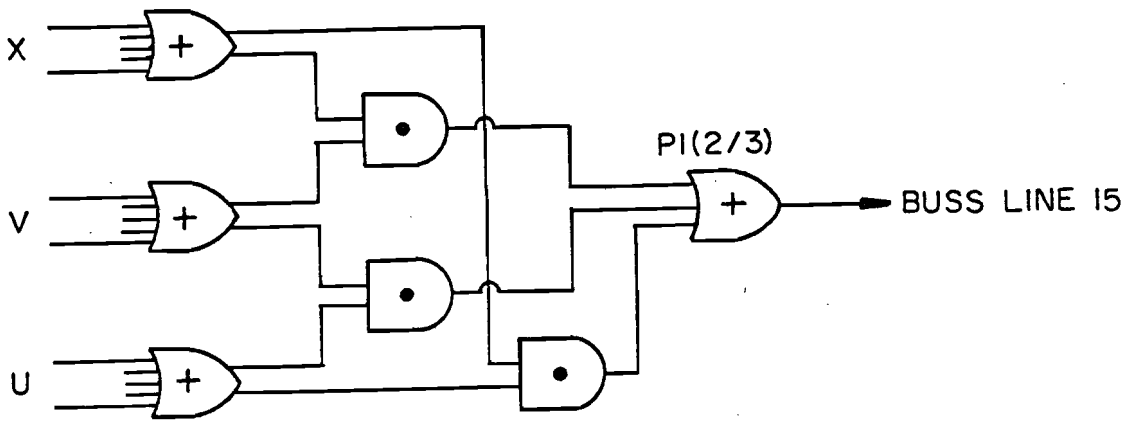
X
V
U
+
+
+
P1(2/3)
+
BUSS LINE 15

Fig. 22. Electronics. Derivation of buss line 4 (PWC logic $= \{P2X_L \cdot P3X_L + P2X_R \cdot P3X_R\} \cdot \{P2(>1)^2 \cdot P3(>1)^2\}$) from P2, P3 trigger mixers.

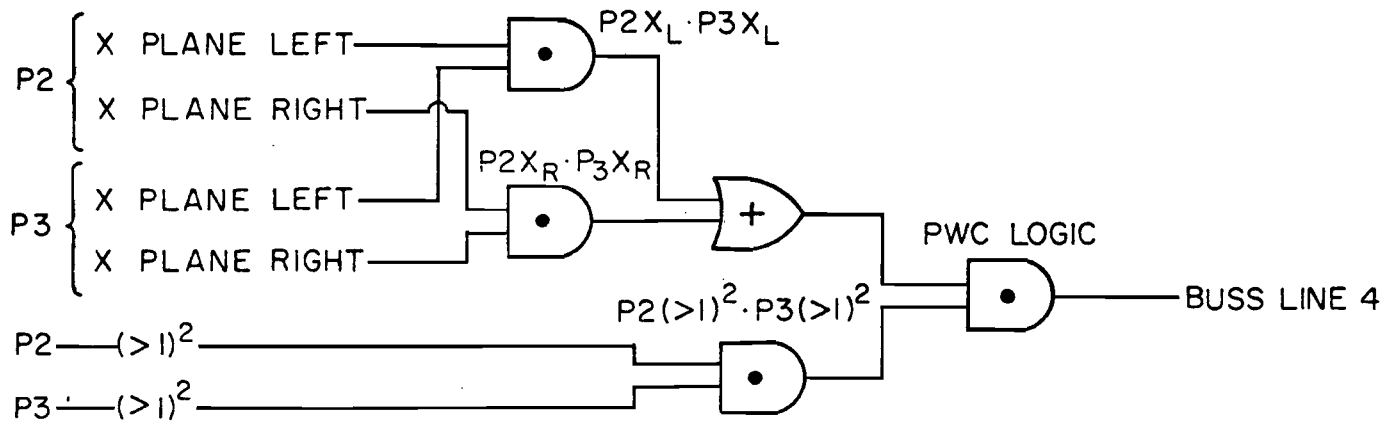
P2
X PLANE LEFT
X PLANE RIGHT
P3
X PLANE LEFT
X PLANE RIGHT
P2 (>1)²
P3 (>1)²
P2X_L · P3X_L
P2X_R · P3X_R
+
P2(>1)² · P3(>1)²
PWC LOGIC
BUSS LINE 4

Fig. 23. Electronics. Pin logic, buss line diagrams showing derivation of leptonic and hadronic triggers. (True = √ and False = X.)

BUS LINE NO.	LOGIC PIN NO.					
	1	2	3	4	5	6
	2μ	2e	2e	μe	H1	H2
1 $\geq 2\pi$	✓	✓	✓	✓	✓	✓
2						
3 B3	✓	✓	✓	✓	✓	✓
4 PWC LOGIC	✓	✓	✓	✓	✓	✓
5						
6 EFR		✓		✓		
7 ETR		✓	✓	✓		
8 EFL		✓				
9 ETL		✓	✓			
10 1μ				✓		
11 2μ	✓					
12						
13 H1					✓	
14 H2		×				✓
15 PWC P1	✓	✓	✓	✓	✓	✓
16 $Ao+(A\mu)>2$	×	×	×	×	×	×

Fig. 24. Electronics. Pin logic module. Inputs are the 16 buss lines, and the strobe and deadtime from the TGI. Outputs are scaled and trigger the TGO.

PIN LOGIC

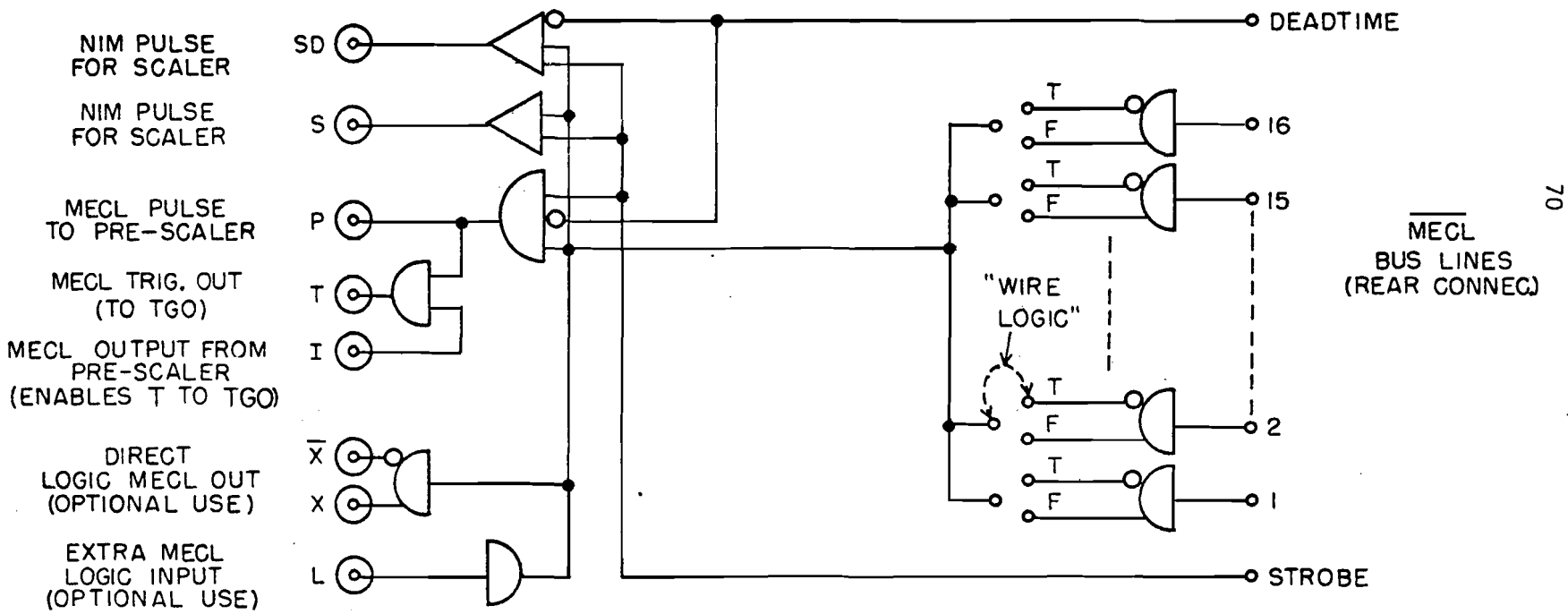
NIM PULSE FOR SCALER
SD
NIM PULSE FOR SCALER
S
MECL PULSE TO PRE-SCALER
P
MECL TRIG. OUT (TO TGO)
T
MECL OUTPUT FROM PRE-SCALER (ENABLES T TO TGO)
I
DIRECT LOGIC MECL OUT (OPTIONAL USE)
$\overline{X}$
X
EXTRA MECL LOGIC INPUT (OPTIONAL USE)
L
DEADTIME
T
F
16
15
"WIRE LOGIC"
2
1
STROBE
$\overline{\text{MECL}}$ BUS LINES (REAR CONNEC.)

Fig. 25. Electronics. Output trigger generator (TGO). The TGO is triggered by the pin logic modules and is inhibited by ACE busy. The TGI gates the ADC's, sends a "hold" to the TGI to prevent the clearing of data during readout, and interrupts ACE.

OUTPUT TRIGGER GENERATOR–TGO

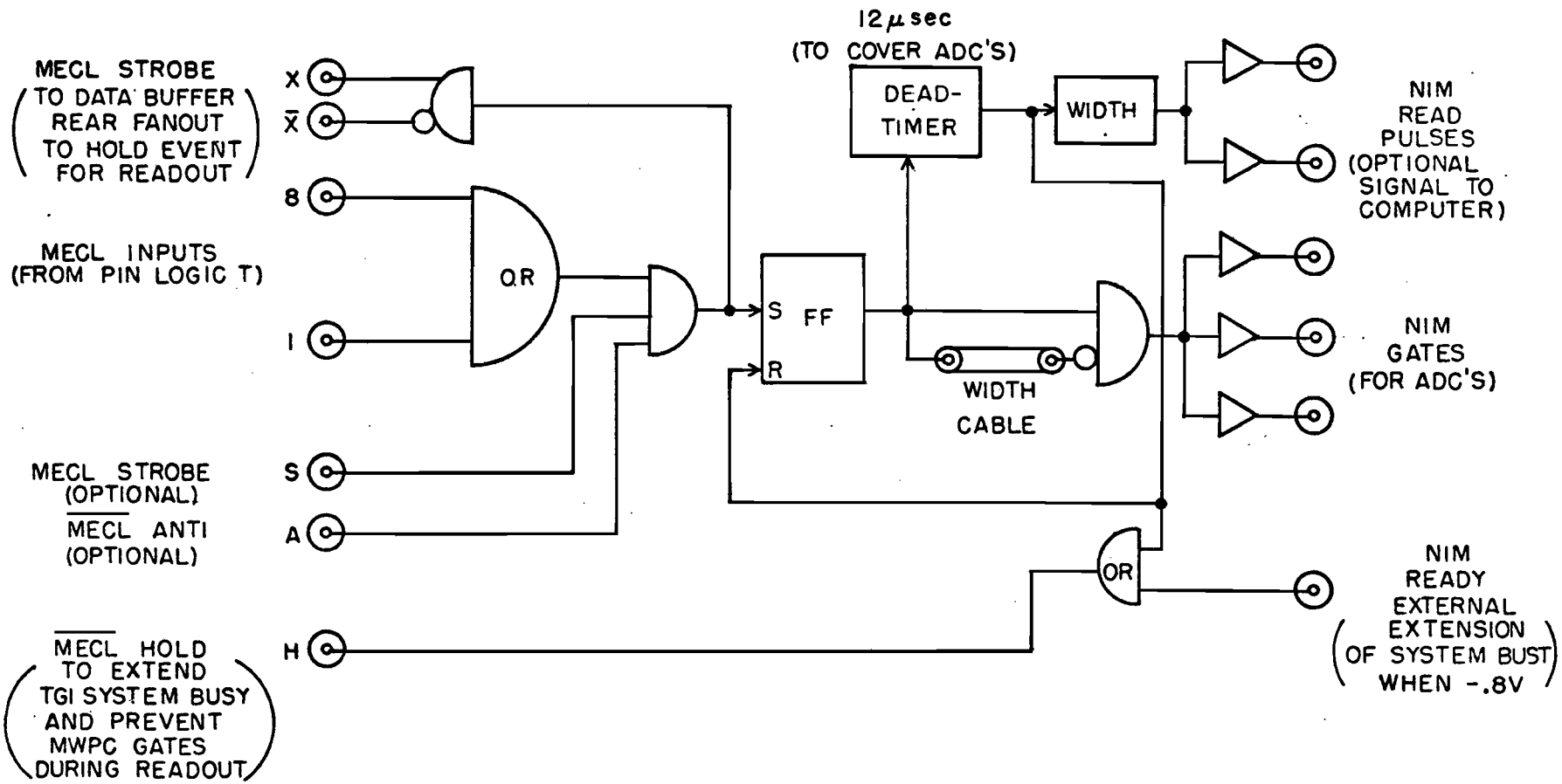

would not satisfy the PWC trigger, so the PWC trigger became (Fig. 22).

$$\text{PWC Logic} = [\bar{P}2(>1^2) \cdot P3(>1^2)] \cdot$$

$$[\bar{P}2X_L \cdot P3X_L + P2X_R \cdot P3X_R]$$

where $(>1)^2$ means greater than one wire firing on two of three planes in the chamber indicated and $X_{L(R)}$ means at least one wire firing (outside of the central sixteen wires) in the indicated chamber on the left (right) side. The PWC logic requirement went to the buss lines and was required in most triggers (Fig. 23).

A buss line driver and the pin logic cards are inserted in a special crate whose buss lines are the sixteen possible logic decisions from the Σ logic, deadtime from the trigger output generator (ACE busy), the strobe from the TGI (delayed gate), and of course, power. Pin logic decisions, which finally determine the trigger type, are made by placing a jumper (pin) between the input of a given buss line and its AND gate (Fig. 24). For every pin logic card the strobe is required and the deadtime is a veto. Any of the sixteen buss lines may serve as a logical true or false depending upon the particular trigger desired. For example, let us consider the 2e trigger pin 2. This pin logic trigger has the following requirements (Fig. 23):

Buss Line 1: $\geq 2\pi$

Buss Line 3: B3

Buss Line 4: PWC Logic

Buss Line 6: EFR

Buss Line 7: ETR

Buss Line 8: EFL

Buss Line 9: ETL

Buss Line 14: $\overline{H2}$

Buss Line 15: P1

Buss Line 16: $\overline{A_o + \Sigma(A_\mu) > 2}$.

The derivation of these buss lines is shown in Figs. 18-22. To require a given buss line, say buss line 3 (B3), a pin is placed between buss line 3 and AND gate 3. To discriminate against a given buss line, say buss line 14 (HC2), a pin is placed between that buss line and the veto input to the AND gate.

When all buss line requirements of a given pin logic have been satisfied, outputs are generated to a scaler, a livetime scaler (ACE not busy--from TGO), and to an optional prescaler. If the prescale requirement is satisfied and ACE is not busy an event trigger is issued. This trigger is tagged by a trigger store and through the TGO interrupts ACE. The trigger store tag is eventually strobed in with the rest of the CR buffer data.

In the meantime, ADC as well as PWC wire information is pouring into the system. Analog anode signals from each shower detector and each hadron calorimeter counter and summed dynode signals from each counter array are integrated by the ADC's. The signals from each counter are timed to arrive simultaneously with the gate signal from the TGO. The ADC's then integrate the pulse area of each signal while the gate is on (30 ns). The output of the ADC's is a pulse train; the

number of pulses in the train being proportional to the input pulse area. The ADC's are linear in a range from 0 to at least 1024 channels. The gain of the ADC's was chosen to give approximately 1000 pulses (channels) for a 100 GeV signal, or 10 channels/GeV. The pulse train is scaled by computer addressable scalers. These scalers are read and cleared by ACE (buffer memory) when ACE has been interrupted (triggered) by the TGO.

A large portion of the electronics is devoted to the PWC's. There are approximately six thousand wires in fifteen planes. The output of each wire is amplified and discriminated at the chamber. These discriminated signals are sent to trigger mixers as described above and to the PWC electronics rack (Fig. 13). This rack consists of register cards, encoder cards, and the PWC interface. The register cards are gated by the TGI and set bits for those wires which have fired. The register cards are cleared by a delayed TGI gate if the event is not to be read by ACE (Fig. 15). If the event is to be read, a hold from the TGO prevents the clearing of the register cards until the event is read out. When the event is read, the encoder cards code the bits indicating which chamber, plane, wire, and adjacencies have fired. This information is transferred through the PWC interface to ACE. Eventually one encoder card has finished. It returns an "empty" signal, and the next encoder begins reading and transmitting.

The entire data taking process is controlled by ACE, the buffer memory, and its associated electronics. Its functions

have been briefly discussed above. In more detail then, ACE is a solid state memory (INTEL Corporation) capable of storing 32K of 16 bit words. ACE is activated by an interrupt generated from the pin logic-TGO system (Fig.13). ACE then begins reading in words along 16 bit data lines. The sequence of data transferal is determined by hardware. Each bin of addressable scalers, registers, buffers and interfaces has its own port through which it communicates with ACE. Each bin and every half-slot (top and bottom) in the bin has an address which ACE has been wired to read. Some addresses will transmit only one word to ACE (e.g., ADC scalers), while others (e.g., CR buffer interface, PWC interface) will transmit several 16 bit words. In the case of the CR buffer a fixed number of words (ten) is transmitted, but for the PWC's a variable number (one for every hit in each plane) is transmitted. When ACE has finished reading and clearing every bin, the system is then ready to receive another event. Events are taken until the memory is full or the beam spill is over. Typical events are about 150 words long so up to 200 events per pulse may be taken.

When the beam spill is over, ACE begins transmitting data to the Σ2. The Σ2 then writes the data on magnetic tape (800 BPI nine track).

Since the actual data taking is done by ACE and associated hardware, the Σ2 is free a good portion of the time to do other tasks. These tasks include on-line analysis and scope display. The on-line program is divided into two parts, foreground and

background. The foreground program formats the data written on tape, fires the light pulser, and sums the monitor information such as SEM, loss monitors, quantameter, light pulser, and pin logic scalers. Besides the data records discussed above, several other record types are written. A begin run record signals the beginning of a new run and contains information about initial conditions such as magnet current and run number. An end of spill record signals the end of a beam spill and contains the sums of the various monitors. A light pulser record is written when the light pulser is fired (See Appendix II). And finally, an end run record is the last record of a run and contains the cumulative sum of all the monitors. At the conclusion of a run the foreground program types on the teletype all the monitor information.

The background program selects a few events at random from each spill and does some simple analysis tasks on them. These analysis tasks include: display of chambers and hits, calculation of mass, momentum transfer, vertex distribution, etc., monitoring of the efficiency of chambers (an alarm is sounded if the efficiency is low), wire chamber profiles, and pulse height histograms. A summary of the background program's functions are also typed at the end of a run.

D. Spectrum Measurement and Shower Detector Calibration

In a wide band photon beam it is essential that the beam spectrum be known in order to deduce cross sections. The photon spectrum was measured by producing 0° electron pairs ($\leq$ 2 mr opening angle) and bending them into the shower

detectors. The data taking mode is identical in shower detector calibration or spectrum measurement.

The standard photoproduction target was removed and a thin Pb foil (4% radiation length) was inserted in the beam line just upstream of the horizontal bending magnet M1 (Fig. 5). The magnet M1 was set at two different currents and M2 at both polarities alternately to sweep electron pairs into all quadrants of the shower detectors. In other words, four sets of runs were taken. The low M1 current setting swept low energy pairs into the top and bottom counters, while the high current setting swept high energy pairs into the center counters. Reversing the polarity of M2 interchanged the quadrants into which the pairs were bent.

Data was taken in the standard fashion as described in the previous sub-section. The trigger was MG · P1 (2/3). This data could then be used for either shower detector calibration or spectrum measurement.

In the case of shower detector calibration the following cuts were made to obtain a "clean" sample of e^+e^- triggers:

1. Each event was required to have two tracks.
2. The tracks had to define a pair of less than 2 mr opening angle.
3. The tracks had to be of opposite charge.
4. Each track had to lie within 5 cm of the ends of the active area of the detector array.
5. Each track had to lie within 3.8 cm of the top or bottom of the active area of a given counter.

6. The track (i.e., a 3.8 cm cone around the track) had to pass through one and only one front and one and only one back counter.

In other words, the cuts insured that an event for calibration purposes had two 0° tracks of opposite sign each of which were totally confined to one front and one back counter. In this way each front counter was calibrated separately with two overlapping back counters and each back counter (except the four at extreme top and bottom) was calibrated with two overlapping front counters.

The purpose of the calibration runs was to determine the conversion factors (calibration constants) which translate ADC pulse height measurement into energy measurement. To derive these constants, we use a method of Lagrange multipliers. Let

N_F = ADC reading for front counter

N_B = ADC reading for back counter

p = momentum of track

E = energy deposited in the shower detector.

The signature for electrons in the shower detectors is the fact that $E = p$; so we wish to minimize the function $f = E/p$ as a function of the calibration constants, defining $\varepsilon_F = N_F/p$ and $\varepsilon_B = N_B/p$, and introducing the calibration constants G and α, we write

$$f = E/p = G/p\ (\alpha N_F + N_B)$$

or (17)

$$f = G\ (\alpha\varepsilon_F + \varepsilon_B).$$

Then defining the calibration constants $\beta = G_\alpha$ and $\gamma = G$

$$f = \beta\varepsilon_F + \gamma\varepsilon_B. \tag{18}$$

We can calculate the variance (width) δf of f in terms of β , γ and the measured pulse heights. Details of this calculation are given in Appendix I. We introduce a Lagrange multiplier λ and the function

$$h = 1 - \bar{f} = 1 - \frac{1}{N}\sum_{i=1}^{N} f_i \tag{19}$$

and then minimize $\delta f + \lambda h$ with respect to β, γ, and λ. Using this method we obtain calibration constants for each counter.

Typical results for a calibration run are shown in Fig. 26. The function f = E/p is plotted for one counter. Also the resolution curve for all counters is shown. The curve can be fit by

$$\frac{\Delta E}{E}\ (\%) = \frac{39}{\sqrt{E}} + 2.6. \tag{15}$$

At 100 GeV the shower detectors have a resolution of 6.5% and about 8% at 50 GeV.

As was mentioned previously, these runs were taken at least once a week. Using this information the phototube high voltages were set to give equal gains for each counter.

Once the shower counters are calibrated the photon spectrum can be measured from the same data tapes. The following cuts were made on the data:

1. Each event was required to have two tracks.
2. The two tracks had to have a maximum opening angle of 2 mr.

Fig. 26. Shower detector calibration.

a. Resolution of the detectors as a function of $1/\sqrt{E}$ is shown.

b. E/p for a typical sum of EF and EB counters at $p \approx 10$ GeV.

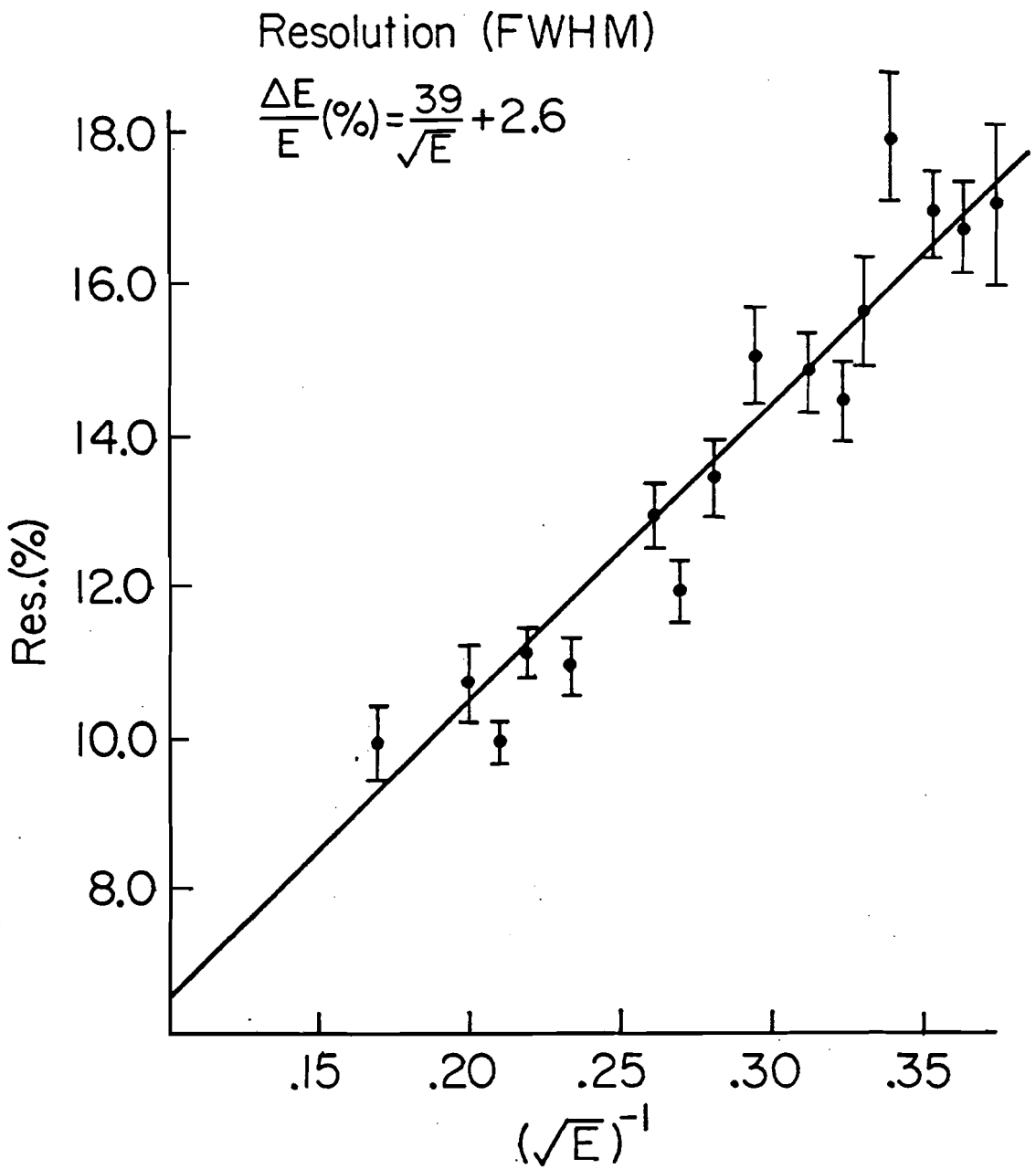
Resolution (FWHM)
$\frac{\Delta E}{E}(\%) = \frac{39}{\sqrt{E}} + 2.6$
Res.(%)
18.0
16.0
14.0
12.0
10.0
8.0
.15
.20
.25
.30
.35
$(\sqrt{E})^{-1}$

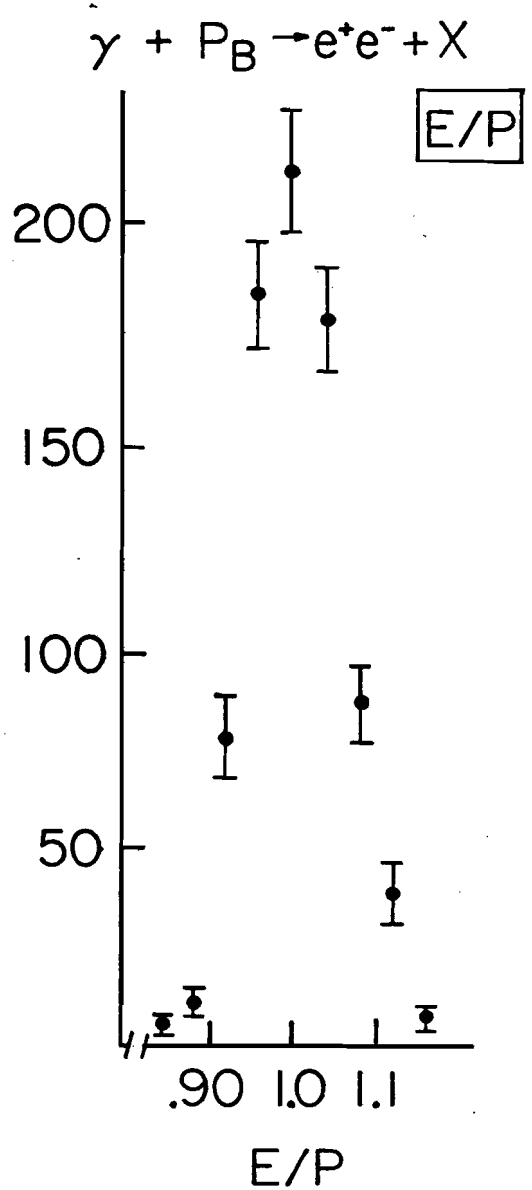
$\gamma + P_B \rightarrow e^+e^- + X$
E/P
200
150
100
50
.90
1.0
1.1
E/P

3. The particles defining the tracks had to be of opposite sign.

Geometric acceptance and electronic deadtimes were folded in. The number of events were normalized to SEM (number of protons per pulse). The resulting measured spectra are shown in Fig. 27 for incident protons of 300 and 380 GeV/c momentum.

One important check of the beam during running periods was to monitor the ratio of quantameter/SEM. This ratio should remain constant if all beam elements are functioning properly. The status of the liquid D_2 system could be checked by measuring this ratio (Q/SEM) as the Pb attenuation sheets were inserted one at a time (Fig. 2). From Fig. 28 we can see that Q/SEM is highly dependent on the status of the liquid D_2 system. When the D_2 cryostats are full, we see an $e^{-\frac{7}{9}\frac{X}{X_o}}$ dependence on the Pb sheets. When the cryostats are empty the beam is essentially all neutrons. In this way then, the "quality" of the beam could be checked.

Fig. 27. Photon spectrum from 300 and 380 GeV/c protons.

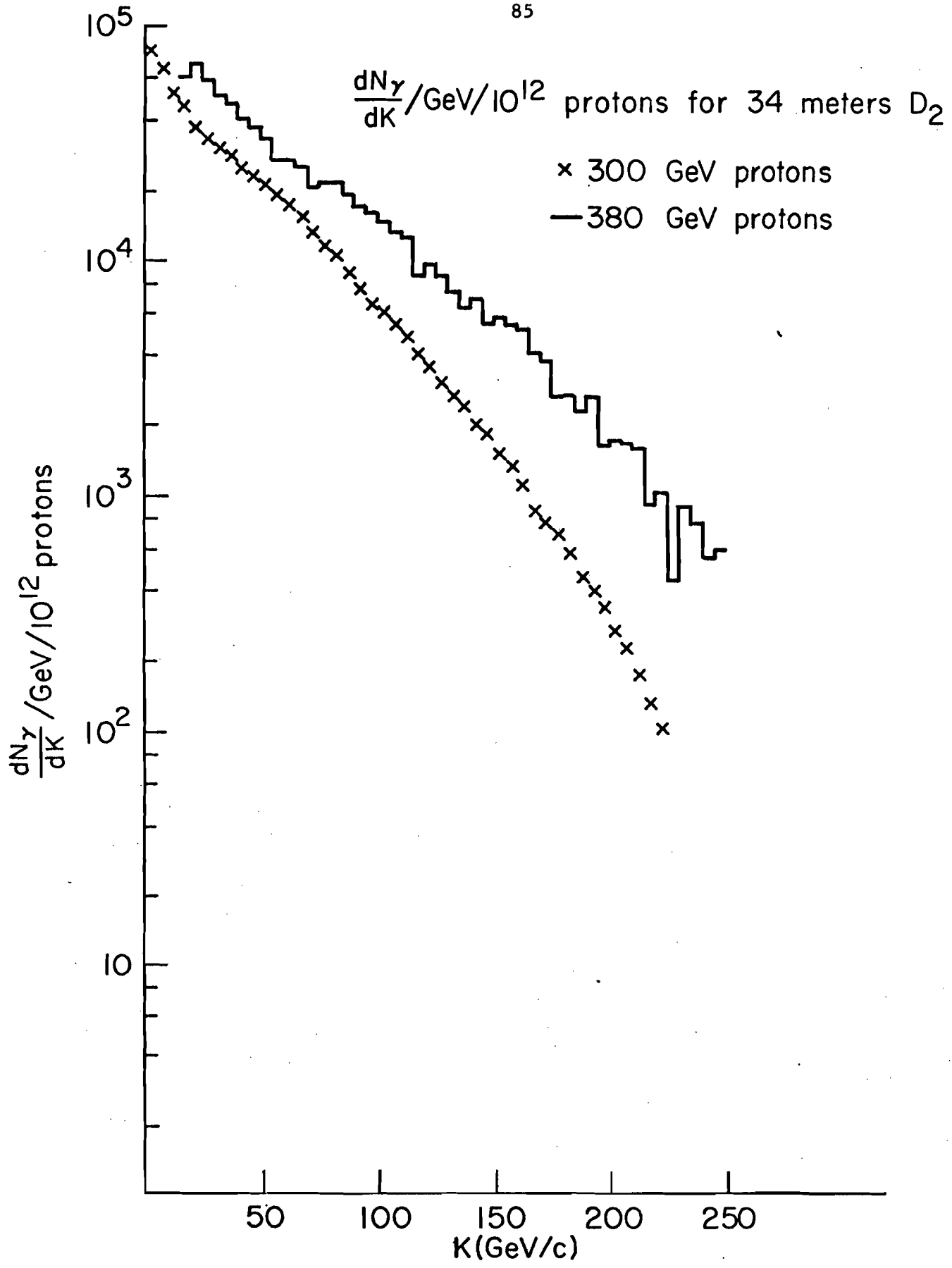
$\frac{dN_\gamma}{dK}$/GeV/10^{12} protons for 34 meters D_2
× 300 GeV protons
— 380 GeV protons
10^5
10^4
10^3
10^2
10
$\frac{dN_\gamma}{dK}$/GeV/10^{12} protons
50
100
150
200
250
K(GeV/c)

Fig. 28. Quantameter/SEM versus number of radiation lengths of Pb inserted by photon attenuator. The curves show that the beam is essentially all neutrons for 0 m of liquid D_2 and essentially all photons for 34 m of liquid D_2.

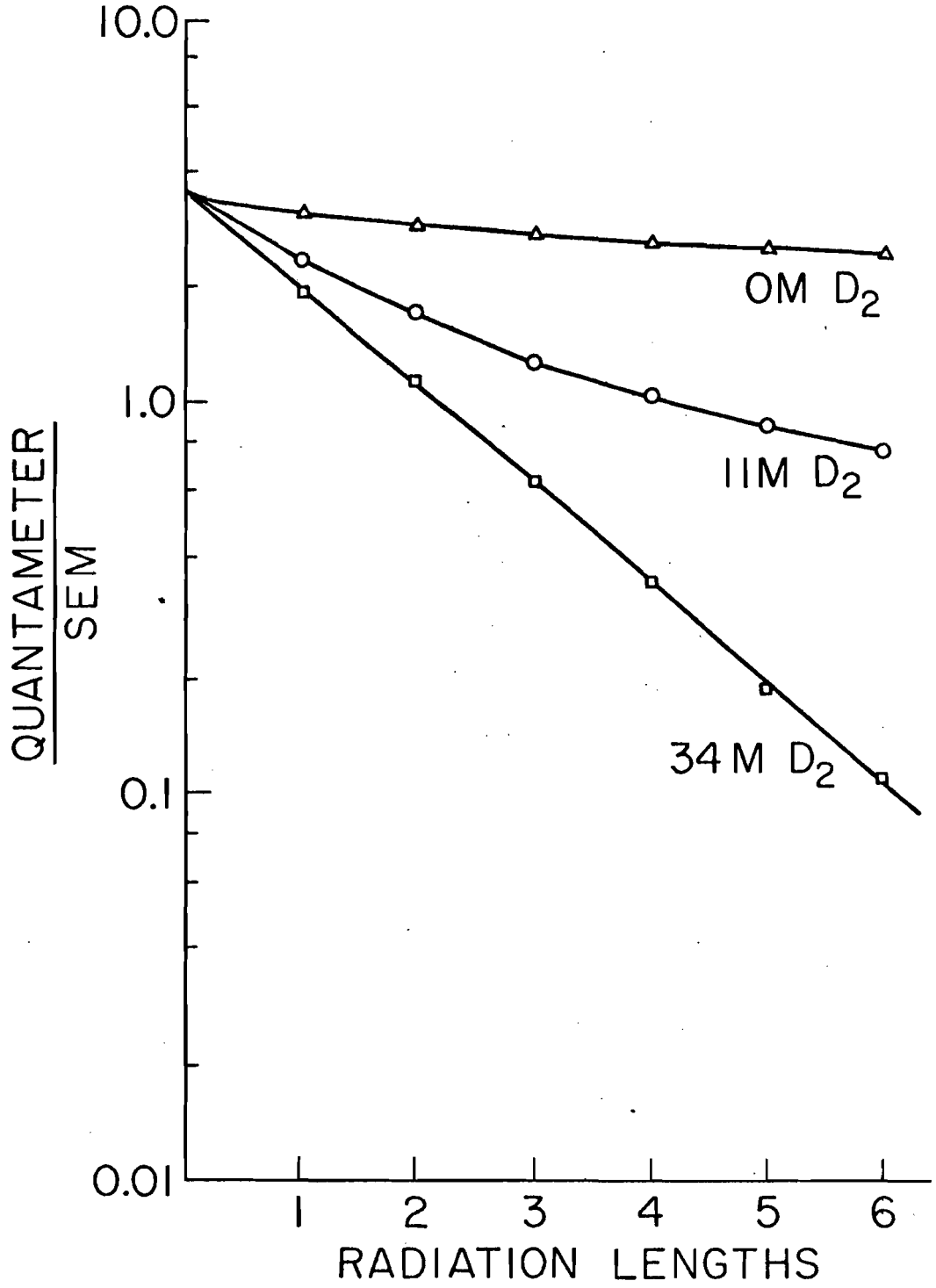
10.0
1.0
0.1
0.01
QUANTAMETER / SEM
OM D_2
11M D_2
34 M D_2
1
2
3
4
5
6
RADIATION LENGTHS

III. DATA AND RESULTS

A. Overview

In this section we present results of photoproduction of electron pairs at the highest photon energies. In particular we discuss data from the interaction $\gamma + Be \rightarrow \psi_{\hookrightarrow e^+e^-} + X$. Several corrections must be made to the raw data. These corrections include geometric acceptance, counter efficiency, and electronic livetime. Folding in these corrections and normalizing to beam flux, we calculate $\sigma(\psi \rightarrow e^+e^-)$, $\frac{d\sigma}{dt}$, $(\frac{d\sigma}{dt})_{t=0}$, and finally $\sigma(\psi N)$. Data is presented for distributions of mass of the pairs M, momentum transfer t, photon energy K, electron transverse momentum p_T, and decay angular distribution $\cos\theta^*$. A comparison between this experiment and similar experiments will be given.

B. Raw Data

Electron pair data was taken in four different running conditions summarized in Table 1. The variable conditions in these sets were the incident proton energy, thickness of the Be target, position of the target, number of chambers, and the width of the shower counter gap.

TABLE 1: VARIABLE CONDITIONS

Data Set Variables	1	2	3	4
Proton Momentum (GeV/c)	300	300	300	380
Number of Chambers	5	4	4	5
Target (cm of Be)	7.6	5.1	2.5	2.5
Target Position (m) (from center of magnet)	-6.55	-4.19	-4.34	-6.60
Shower Detector Gap (cm)	$\pm$7.6	$\pm$3.8	$\pm$3.8	$\pm$7.6

Data was taken with the pin 2 trigger which required (Fig. 23).

Buss Line 1: $\geq$ 2 hits in the horizontal and vertical trigger array (H, V)

Buss Line 3: B3 (the target trigger counter)

Buss Line 4: PWC logic (at least one track on the left and right sides of chambers P2 and P3)

Buss Line 6: EFR (shower energy greater than minimum ionizing in the front right shower detectors)

Buss Line 7: EFL (shower energy greater than minimum ionizing in the front left shower detectors)

Buss Line 8: ETR (total shower energy greater than 10 GeV in the right shower detectors)

Buss Line 9: ETL (total shower energy greater than 10 GeV in the left shower detectors)

Buss Line 10: $\overline{HC2}$ (veto on energy in the hadron calorimeter)

Buss Line 15: P1(2/3) (at least 2 of 3 planes in chamber P1 firing)

Buss Line 16: $\overline{A0 + \Sigma(A_\mu) > 2}$ (veto on any hits in the anticounter A0 or more than two in the anticounters A1-A6)

The function of these buss lines was described in Sec. II. C. The overall effect of this trigger is to require two or more charged particles originating in the target, passing through the PWC's, and depositing energy in both sides of the shower detectors, but no energy in the hadron calorimeter.

The data was analyzed by a multi-step process. First the output tapes from the $\Sigma 2$ were analyzed by a reconstruction program to find tracks in the chambers (see Appendix I). Second, output tapes from the track reconstruction program were compressed by saving only those events with two or more tracks that satisfied the pin 2 trigger. Finally, all data from these compressed tapes with two or more tracks were examined. The following cuts were made on the data:

1. Two or more tracks were required
2. Two of the tracks must be identified as electrons of opposite sign, i.e.,
   A. Energy in the front shower detector greater than minimum ionizing for each track
   B. $E/P > 0.5$ (shower energy/track momentum) for each track
3. Photon energy of 50 (70) GeV or greater for the four (five) chamber running
4. Target bremsstrahlung, $E_{\gamma B}$, at most 75% of the energy of the electron, E

5. Geometric cuts

   A. Distance of closest approach of the tracks < 5 mm

   B. Vertex (as defined in (A) within ± 15 cm of the center of the target in the "Z" direction

   C. Vertex within the target and beam spot in X and Y (typically ± 2.5 cm)

   D. Both tracks within the fiducial volume defined in Table 2.

TABLE 2: FIDUCIAL VOLUME, GEOMETRIC ACCEPTANCE

Apparatus	Z (cm)	Y_{min} (cm)	Y_{max} (cm)	X_{min} (cm)	X_{beam} (cm)	X_{beam} (cm)	X_{max} (cm)
P1:	-338.1	-19.1	19.1	-12.7	0	0	12.7
M2:	91.4	-30.5	30.5	-20.3	0	0	20.3
P4:	715.3	-76.2	76.2	-50.8	0	0	50.8
H, V:	801.1	-81.3	81.3	-53.3	-2.5	2.5	53.3
Shower Detector:	863.6	-88.9	88.9	-50.8	-7.6 (-3.8)	7.6 (3.8)	50.8

() denotes four chamber shower counter gap

The sample of data obtained from these cuts we will call the "all" sample. This sample was analyzed and the various kinematic and dynamic variables calculated including M, K, t, $\cos\theta^*$, and p_T. Some details of these calculations are given in Appendix I. In particular, we note here the calculation of mass M. Since targets of up to 25% of a radiation length were used, there is a considerable amount of bremsstrahlung from the electrons.

This bremsstrahlung energy must be added to the energy of the electron. The photon bremsstrahlung energy is measured by the shower detectors. If $E_{\gamma B}$ is the energy of the bremsstrahlung photon, p is the momentum of the electron, and θ_L is the opening angle of the electron pair in the laboratory. Then

$$M^2 = 2Me^2 + 2(p^+ + E^+_{\gamma B})(p^- + E^-_{\gamma B})(1 - \cos\theta_L) \qquad (20)$$

$$= 2Me^2 + 2(E^+)(E^-)(1 - \cos\theta_L).$$

An example of this calculation is shown in Fig. 29. A mass plot of this sample is shown in Fig.30 for the sum of all data sets.

Further cuts were made to obtain a "clean" sample. These cuts were:

1. Exactly two tracks coming from the vertex
2. At most one hit in the t, AB, or AW counters (consistent with nucleon recoil).

The events remaining after these cuts are shown in Fig. 31. As we can see in Figs. 30, 31, there is a continuum of events from $1.2 < M < 2.8$ GeV with no particularly distinctive features. (We will discuss this continuum further in Sec. III. E. 3.) However, above 2.8 GeV we see a very large peak many standard deviations above the background at 2.7 GeV. These events are from the e^+e^- decay of the $\psi(3095)$ meson. The peak extends from 2.8 to 3.4 GeV with no events of mass greater than 3.4 GeV. For two-body decays one also expects an enhancement in the single particle p_T distribution. In Fig. 32 we see an exponential distribution in the continuum region from $0.5 < p_T < 1.2$ GeV/c. Above 1.2 we can see a definite enhancement in the p_T distribution consistent with the e^+e^- decay of the ψ meson.

Fig. 29. Target bremsstrahlung. Example of the addition of the target bremsstrahlung energy to the momentum of the electron. In this example the mass calculated from the momentum vectors gives M = 2.72 GeV, but by adding the bremsstrahlung energy the mass becomes M = 3.06 GeV.

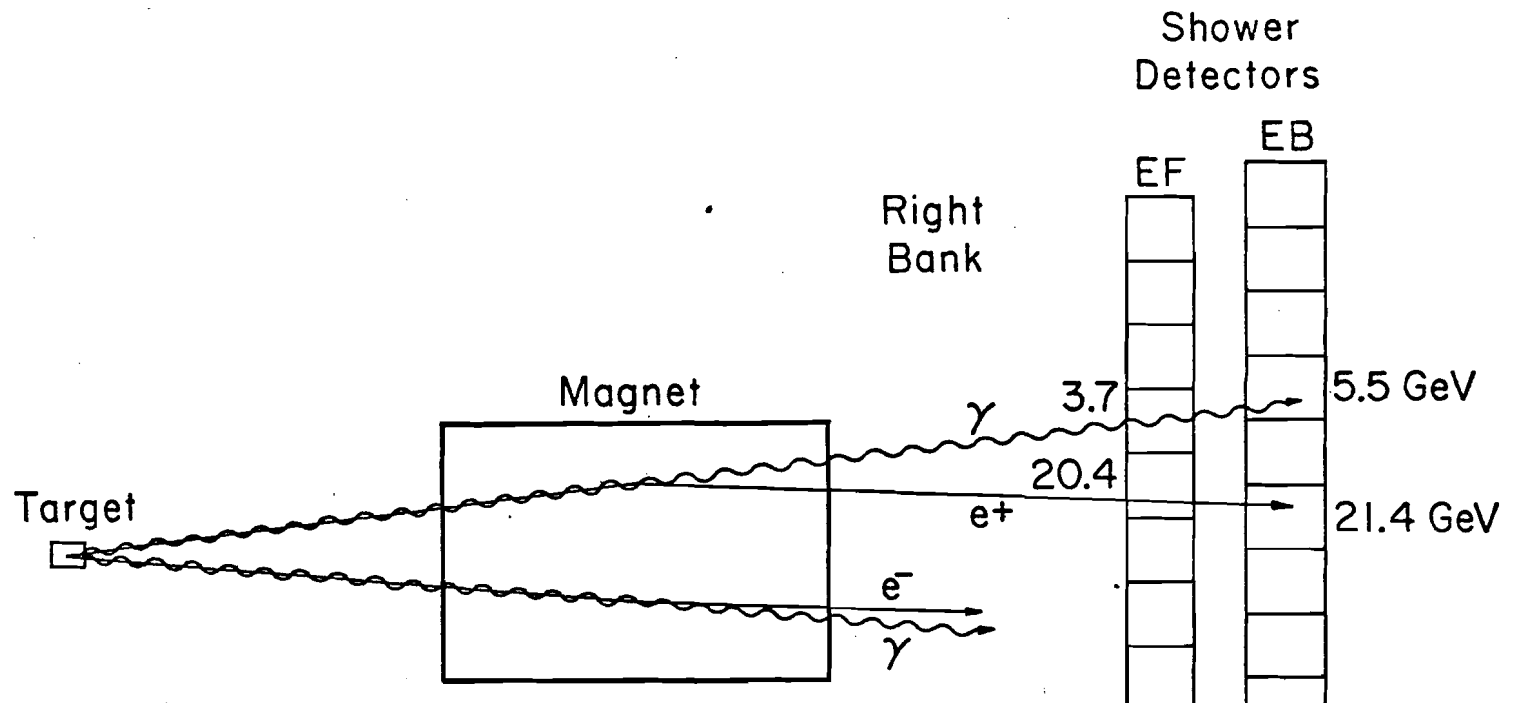

Right Bank	Left Bank
e^+ :	e^- :
$P = 37$ GeV	$P = 50$ GeV
$E_e = 46$ GeV	$E_e = 51$ GeV
$E_\gamma = 9$ GeV	$E_\gamma = 1$ GeV

$M(p) = 2.72$ GeV

$M(p + E_\gamma) = 3.06$ GeV

Fig. 30. "All" mass distribution from $\gamma + Be \rightarrow e^+e^- + X$.

a. There is a continuum of e^+e^- events from 1.2 to 2.7 GeV. Above 2.8 GeV there are seventy-nine events with no events greater than 3.4 GeV. (The mass acceptance extends out to 5 GeV.)

b. Finer detail of the events with $M \geq 2.6$ GeV.

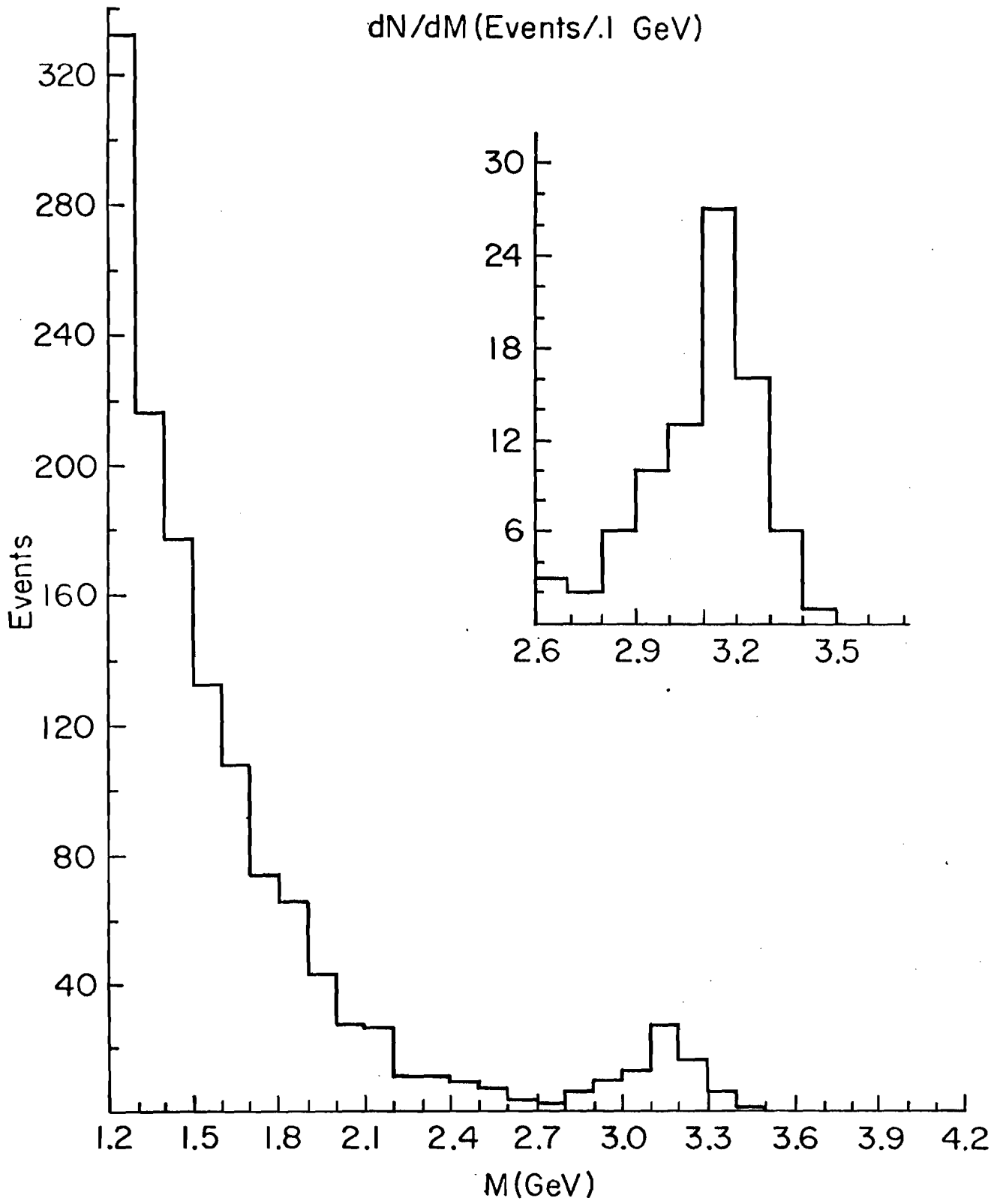
dN/dM (Events/.1 GeV)
Events
320
280
240
200
160
120
80
40
1.2
1.5
1.8
2.1
2.4
2.7
3.0
3.3
3.6
3.9
4.2
M(GeV)
30
24
18
12
6
2.6
2.9
3.2
3.5

Fig. 31. "Clean" mass distribution from $\gamma + Be \rightarrow e^+e^- + X$.

a. There is a continuum of events from 1.2 to 2.7 GeV. Above 2.8 GeV there are fifty-eight events with no events greater than 3.4 GeV. (The mass acceptance extends out to 5 GeV.)

b. Finer detail of the events with $M \geq 2.6$ GeV.

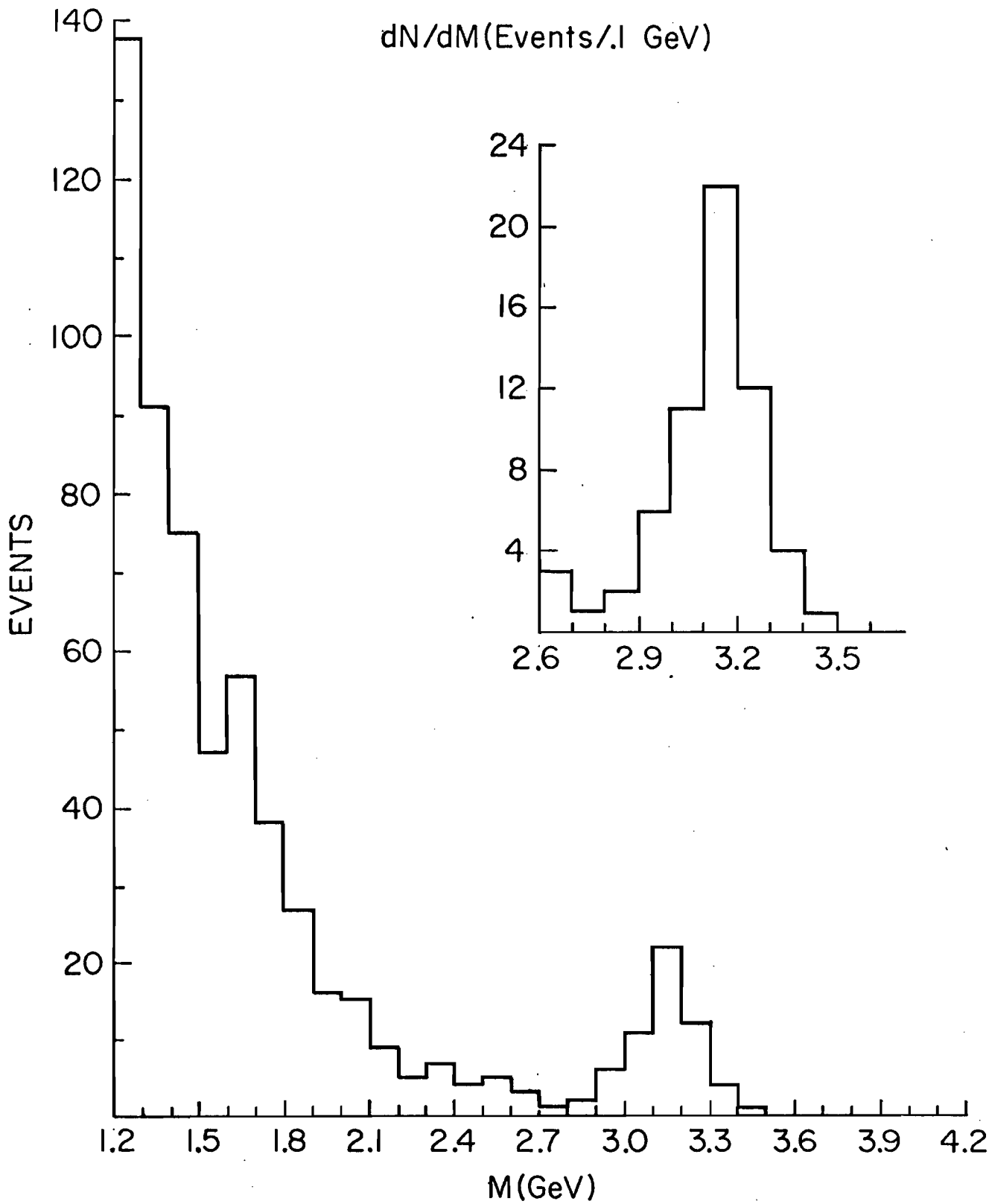
dN/dM(Events/.1 GeV)
EVENTS
140
120
100
80
60
40
20
1.2
1.5
1.8
2.1
2.4
2.7
3.0
3.3
3.6
3.9
4.2
M(GeV)
24
20
16
12
8
4
2.6
2.9
3.2
3.5

Fig. 32. Distribution of events as a function of single electron p_T. There is an exponential distribution up to 1.2 GeV with an abundance of events above 1.2 GeV p_T indicating $\psi \rightarrow e^+e^-$ decay ($p_T \simeq \frac{1}{2}$ M).

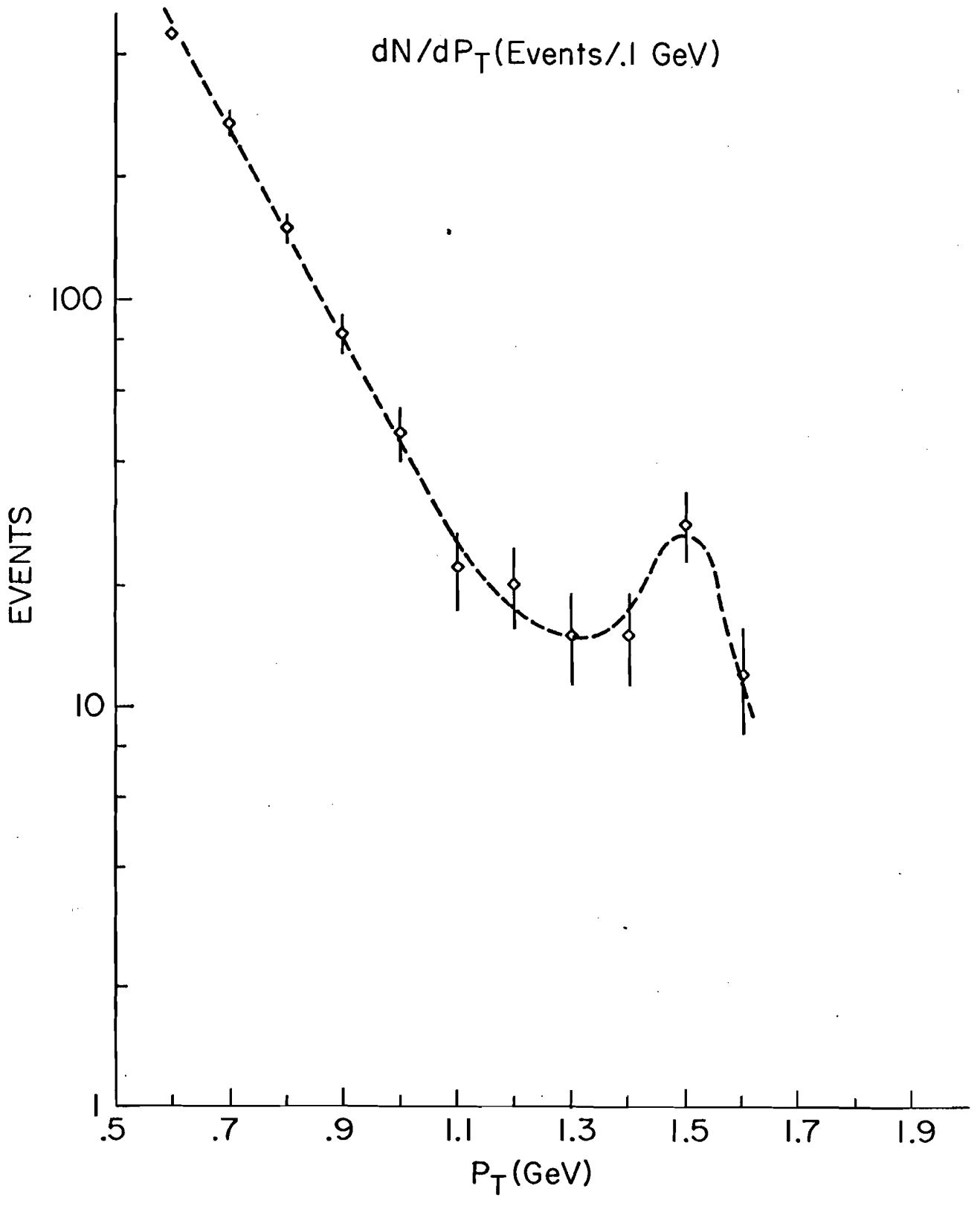
dN/dP_T(Events/.1 GeV)
EVENTS
100
10
1
.5
.7
.9
1.1
1.3
1.5
1.7
1.9
P_T(GeV)

Since the ψ is known to be a very narrow resonance, the remaining question is to determine the events within the experimental mass resolution of the ψ. We plot the curve

$$G = Ke^{-g^2/2} \tag{21}$$

where K is a constant, $g = (m - 3.1)/\langle\delta M\rangle$ and $\langle\delta M\rangle$ is the mass resolution calculated in Appendix 1. A plot of this Gaussian and the events from the two samples are shown in Figs. 33, 34. If we cut at $g = \pm 3$ $(2.8 < M < 3.4)$, there are seventy-nine events in the "all" sample and fifty-eight in the "clean" sample.

C. Background

We turn now to a discussion of possible contamination from background processes to the ψ events in Figs. 30, 31. We consider these possible sources: hadronic background, neutron or K_L^o production, and B-H pair production.

A plot of E/p is shown for the "all" sample in Fig. 35. Based on this distribution and a π/e rejection ratio of $\approx 4 \times 10^{-3}$, we estimate that no events in the ψ region come from two track hadronic events.

Ten per cent of the data taken at the 380 GeV running was taken with the lead attenuator inserted. This sample was also analyzed and only one event in the ψ region was found. One event is completely consistent with what one would expect from the photons still remaining in the beam after attenuation. We therefore estimate no background from neutron or K_L^o production.

One further possible background is from high mass B-H pairs.

Fig. 33. Plot of the function $G = Ke^{-g^2/2}$ discussed in the text for the "all" sample.

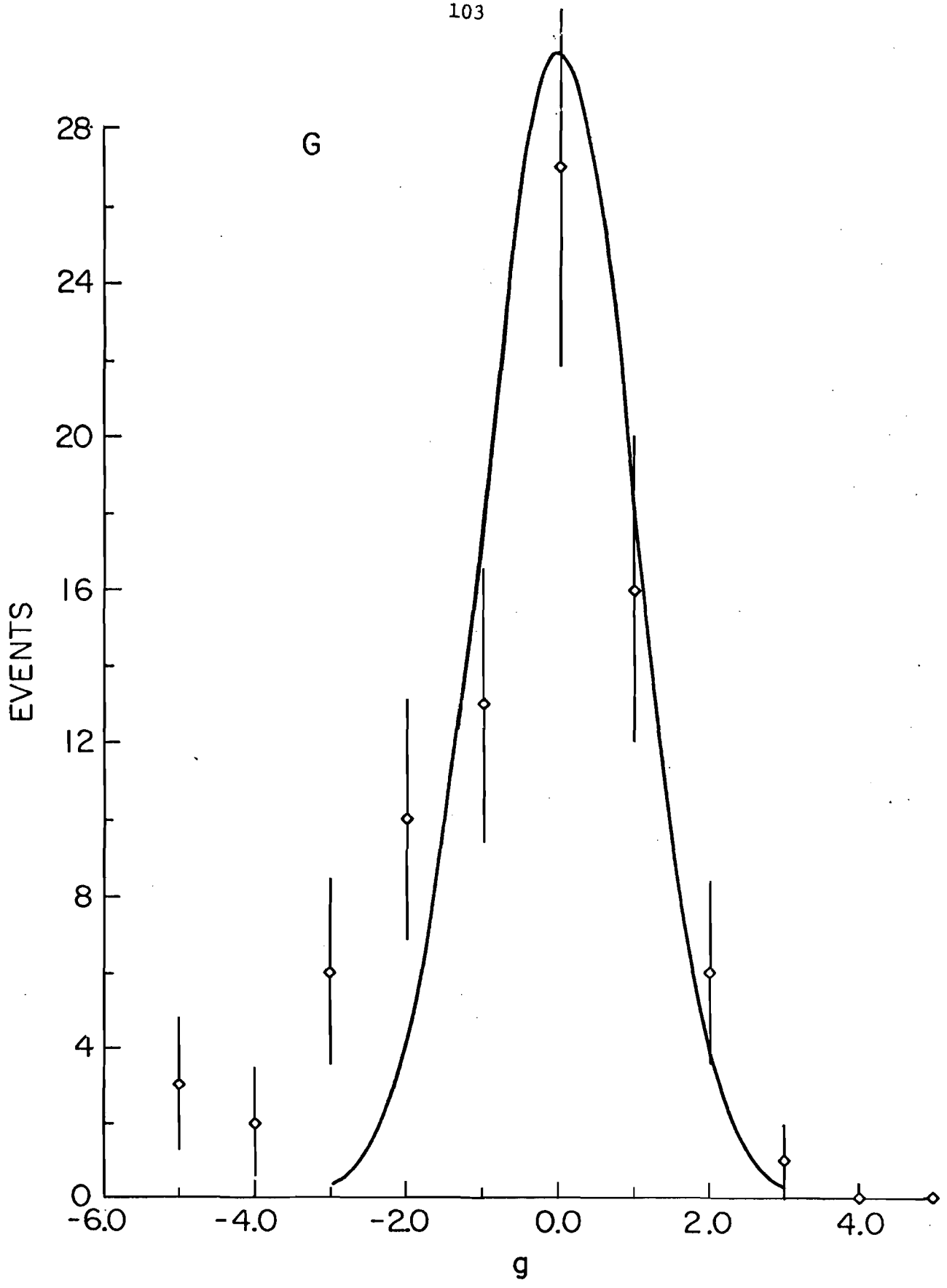
G
EVENTS
28
24
20
16
12
8
4
0
-6.0
-4.0
-2.0
0.0
2.0
4.0
g

Fig. 34. Plot of the function $G = Ke^{-g^2/2}$ discussed in the text for the "clean" sample.

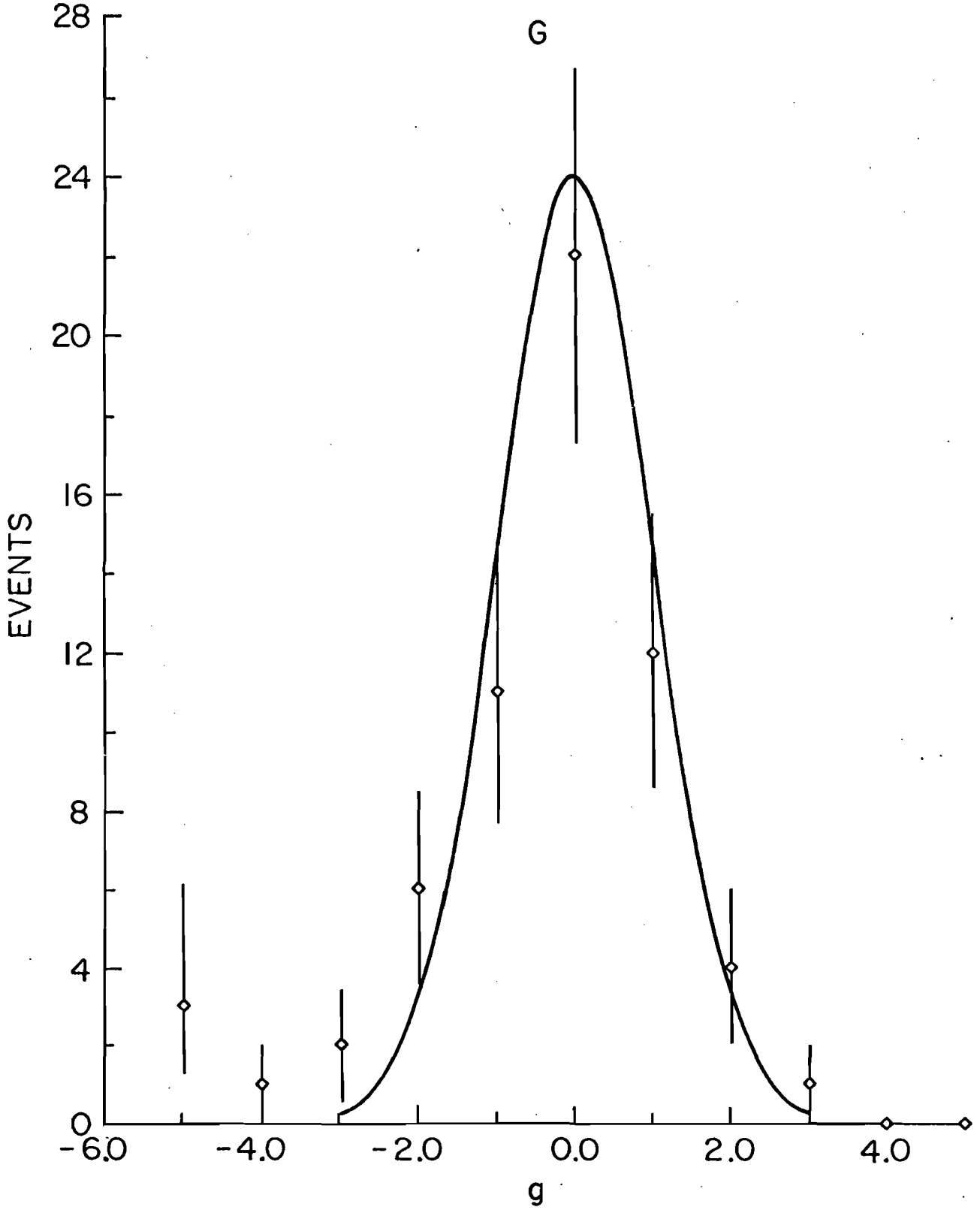
G
28
24
20
16
12
8
4
0
EVENTS
-6.0
-4.0
-2.0
0.0
2.0
4.0
g

Fig. 35. Distribution of E/p for the ψ events in the "all" sample.

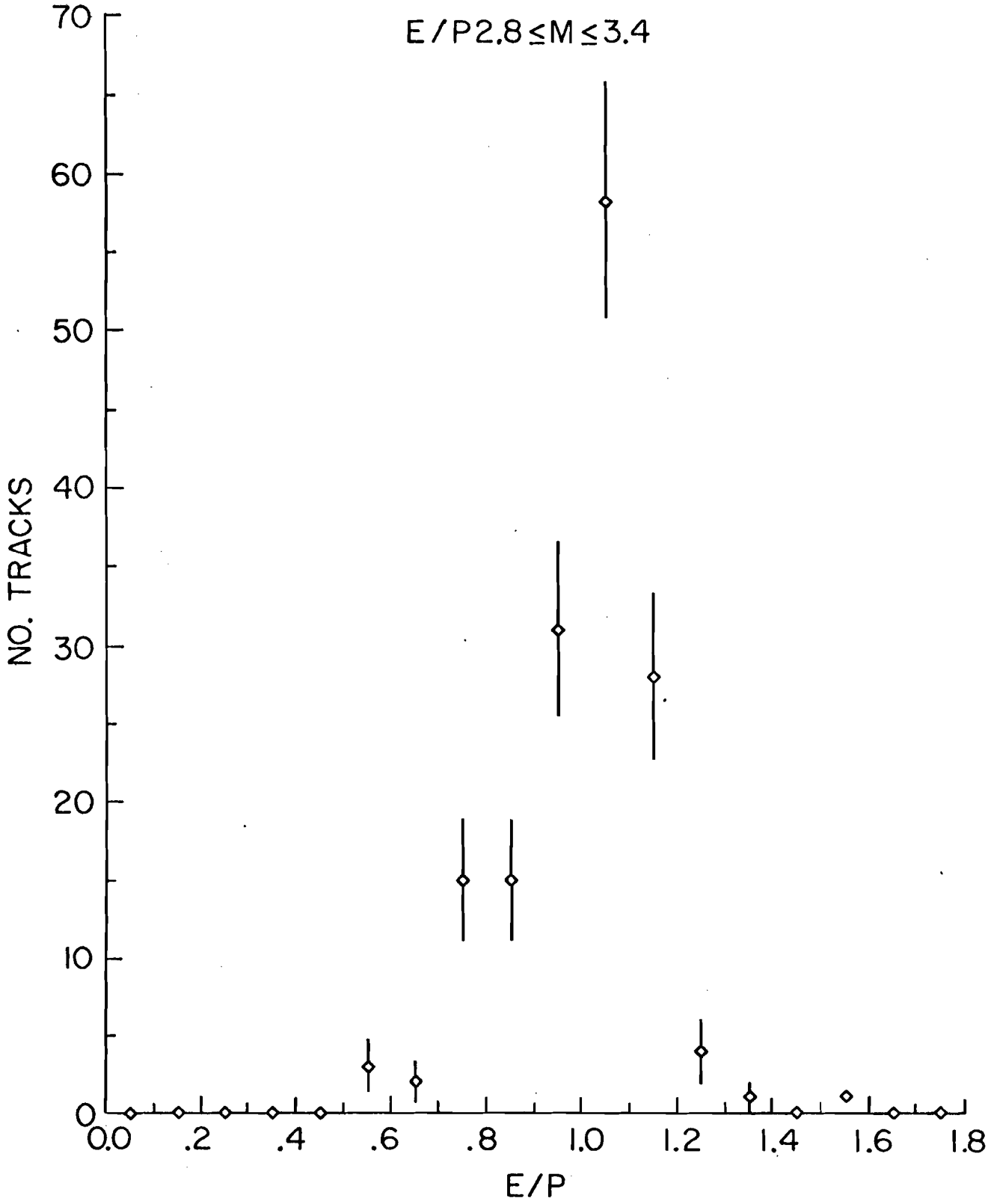
E/P2.8≤M≤3.4
NO. TRACKS
70
60
50
40
30
20
10
0
0.0
.2
.4
.6
.8
1.0
1.2
1.4
1.6
1.8
E/P

From Figs. 30, 31 we estimate less than one event from this background and therefore subtract none.

However, a correction to the raw data is needed for the effect of the bremsstrahlung energy cut. The data was cut such that $E_{\gamma B}/E < 0.75$. Based on a $1/E_{\gamma B}$ bremsstrahlung spectrum we can calculate the fraction of events lost by this cut (see Appendix I). A correction factor ν for this cut is given in Table 3. The motivation for this cut was the fact that occasionally an energetic π° may accompany an e^+e^- event. The cut has the effect of cleaning up the e^+e^- continuum ($1.2 < M < 2.8$) considerably but only cuts away a number of events in the ψ region consistent with the expected bremsstrahlung spectrum.

D. Acceptance, Flux and Efficiency Corrections

The cross section $\sigma(\psi \to e^+e^-)$ will be calculated using the following formula (dropping the $\psi \to e^+e^-$ subscript)

$$\nu \quad N_{evts} = \varepsilon \; N_A F \; B\sigma \qquad (22)$$

where

N_{evt} = Number of events detected

ε = All efficiency corrections

B = Branching ratio of $\psi \to e^+e^-$ (0.069 ± 0.005)

σ = Total ψ photoproduction cross section

F = Useful flux (flux X acceptance)

N_A = Effective number of atoms in the target

ν = Correction factor for Bremsstrahlung energy cut.

In this section we calculate the factors N_A, F and ε. The results of these calculations are summarized in Table 3.

TABLE 3: EVENTS, CORRECTIONS, AND NORMALIZATION

Data Set Factors	1	2	3	4
Target (cm of Be)	7.6	5.1	2.5	2.5
N_{evts} ("all")	26.0	30.0	5.0	18.0
N_{evts} ("clean")	19.0	21.0	4.0	14.0
ν (brem. factor)	1.08	1.06	1.10	1.05
Q (10^{-4} Coulomb)	2.88	1.61	0.85	3.30
Pin LT	0.96	0.96	0.98	0.87
MG LT	0.96	0.99	0.98	0.83
B3 Efficiency	0.95	0.96	0.94	0.98
(LxR) 2π Efficiency	0.99	0.99	0.99	0.99
$\overline{A0, A_\mu}$ Efficiency	0.80	0.89	0.92	0.98
EF, EB Efficiency	0.92	0.91	0.92	0.93
$\overline{HC2}$ Efficiency	0.99	0.99	0.99	1.00
P1 Efficiency	1.00	1.00	1.00	1.00
PWC Efficiency	1.00	1.00	1.00	1.00
Track Recon. Efficiency	1.00	1.00	1.00	1.00
$\varepsilon(\pi_i$ Efficiency$_i)$	0.64	0.74	0.76	0.65
"L" (cm)	7.00	4.83	2.43	2.47
N_A	8.65	5.97	3.00	3.05
Flux (x 10^9)	2.65	4.01	2.39	3.59

1. Acceptance and Flux

In order to normalize the data we must know the effective number of atoms in the target per cm and the beam flux. The number of scattering atoms for the several Be targets was calculated in the following manner

$$N_A = \frac{N^\circ \rho "L"}{A} \tag{23}$$

where

A = Molecular weight of Be (gm)

ρ = Density of Be (gm/cm^3)

N° = Avagadro's number

$$"L" = \int_0^L e^{-\frac{7}{9}\frac{X}{X_0}} dX.$$

X_0 is the radiation length of Be (35.7 cm), and L is the physical length of the target in cm.

Calculation of the useful beam flux is integrally tied to the calculation of the geometric acceptance. A Monte Carlo calculation of the acceptance, A(K), as a function of the photon energy K was done. Events were generated with the following dynamics and topology:

a. An object of mass 3.095 GeV was generated in the cm frame.

b. The object was allowed to decay into two electrons with a $(1 + \cos^2\theta^*)$ angular distribution and a uniform distribution in ϕ.

c. The electron pair was transformed into the laboratory frame with an energy distribution that agreed with the photon spectrum.

d. The pair was given a t distribution of e^{38t} or e^{4t}.

e. The event was randomly distributed over the target volume.

The electron paths were then traced through the apparatus. Those events which did not lie within the geometric acceptance (Table 2) were cut. Several Monte Carlos were generated for the varying parameters in the four data sets. All relevant variables, their resolution, and acceptance were calculated. In particular, A(K) was calculated and is shown in Fig. 36 for one data set.

The useful flux (for producing ψ's) is then

$$F = \int_0^{K_{max}} \frac{dN_\gamma}{dK} A(K)\, dK \tag{24}$$

where K_{max} is the maximum photon energy and dN_γ/dK is the photon spectrum. The spectrum power is measured by the quantameter in Q Coulombs

$$Qc = \int_0^{K_{max}} K \frac{dN_\gamma}{dK}\, dK \tag{25}$$

where c is the conversion factor (16). (A correction factor $1/e^{-\frac{7}{9}\frac{L}{X_0}}$ is made to the quantameter reading to account for beam interacting in the target.) Now if

N_0 = Number of photons from the spectrum measurement (Fig. 27)

and

Q_0 = The corresponding quantameter reading for N_0 photons

that is

$$Q_0 c = \int_0^{K_{max}} K \frac{dN_0}{dK}\, dK \tag{26}$$

Fig. 36. Monte Carlo generation of photon spectrum $\frac{dN}{dK} \sim e^{-K/35}$ and resulting geometric acceptance $\frac{dN}{dK} A(K)$ for ψ photoproduction.

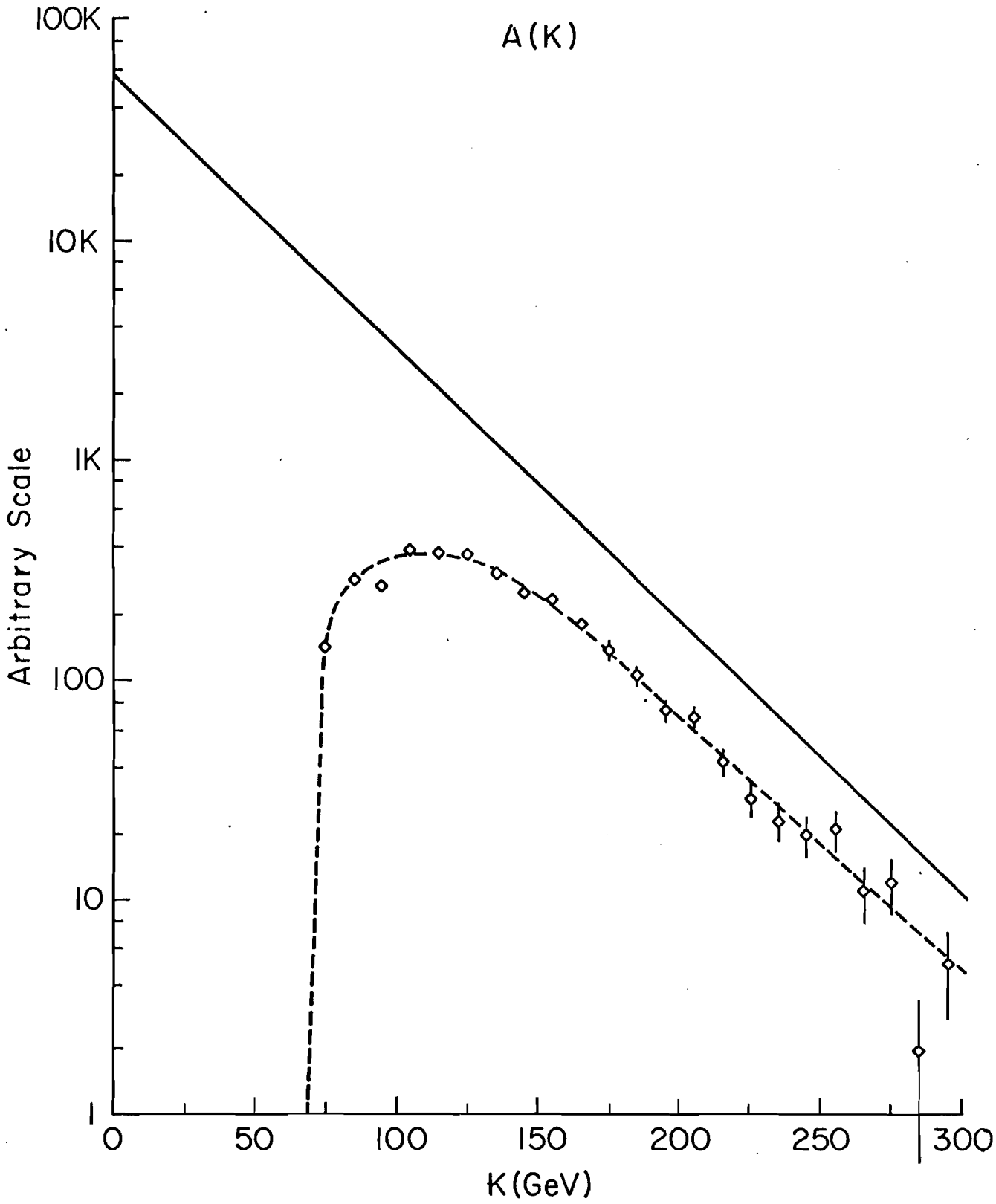
A(K)
100K
10K
1K
100
10
1
Arbitrary Scale
0
50
100
150
200
250
300
K(GeV)

then

$$\frac{N_o}{N} = \frac{Q_o}{Q} \tag{27}$$

so

$$F = \left(\frac{Q}{Q_o}\right) \int_o^{K_{max}} \frac{dN_o}{dK} A(K)\ dK. \tag{28}$$

The results of this calculation are given in Table 3. Expressing the flux as this integral eliminates some of the confusion in using a fit to the spectrum in the Monte Carlo.

2. Efficiency

The efficiency factor, ε, is a product of the electronic livetime, the efficiencies of the detectors in the 2e buss lines, PWC efficiency, and track finding efficiency. The electronic livetime is a product of the pin logic and MG livetimes. These livetimes are obtained from sums of scalers with and without deadtime. So the electronic livetime, LT, is

$$LT = \frac{\Sigma\ \text{Pin}\ 2 \cdot \overline{D}}{\Sigma\ \text{Pin}\ 2} \times \frac{\Sigma\ \text{MG} \cdot \overline{D}}{\Sigma\ \text{MG}}$$

where $\overline{D}$ means the appropriate electronics is live (i.e., not dead).

Counter B3, buss line 3, was subjected to large instantaneous rates due to spill structure and the large B-H production rate. These large instantaneous fluctuations caused deadtime in the counter. If C_o is the actual rate in B3, C is the rate detected for N r.f. buckets, Δt_{B3} is the deadtime of B3, and $\Delta t_{r.f.}$ is the time between r.f. buckets, then

$$C_o = C\ \{1 - \frac{C_o}{N} \left(\frac{\Delta t_{B3}}{\Delta t_{r.f.}}\right)\}. \tag{29}$$

But $\frac{C_o}{N}\left(\frac{\Delta t_{B3}}{\Delta t_{r.f.}}\right) << 1$, so the livetime or efficiency (assuming 100% detection efficiency) is

$$\varepsilon = \frac{C}{C_o} \approx 1 - \frac{C}{N}\left(\frac{\Delta t_{B3}}{\Delta t_{r.f.}}\right) = 1 - \frac{C}{N}(1.0 \pm 0.5). \quad (30)$$

Varying target size, and beam flux caused fluctuations in this correction for the various data sets. The corrections for each set are summarized in Table 3.

The A0, A_μ array was also subjected to large instantaneous rates causing deadtimes in that buss line. Using the notation of the previous example, we can calculate the livetime of A0

$$\varepsilon = \frac{C}{C_o} = 1 - \frac{C}{N}\left(\frac{\Delta t_{A0}}{\Delta t_{r.f.}}\right) = 1 - \frac{C}{N}(2 \pm 1). \quad (31)$$

The A_μ requirement in buss line 16 was $\Sigma(A_\mu) > 2$. If we assume an equal probability p for each of the six counters to be live and q to be dead, then the probability that the array is live for one track is

$$\begin{aligned} \varepsilon = p^7 = 1-(q^7 &+ 7q^6p + 21q^5p^2 + 35q^4p^3 \\ &+ 35\, q^3p^4 + 21q^2p^5 + 7qp6). \end{aligned} \quad (32)$$

However, the A_μ buss line required more than two hits, so the livetime becomes

$$\begin{aligned} \varepsilon &= 1-(q^7 + 7q^6p + \ldots + 7qp^6)^3 \\ &\approx 1-(7qp^6)^3 \end{aligned} \quad (33)$$

which is nearly unity.

The shower detector efficiency involves both a geometric and a high rate correction. A cut was made on the data requiring that the front shower detectors (EF) yield a pulse greater

than minimum ionizing (see Sec. III. B.), but since there is a horizontal gap between counters, not all electrons would register a sufficient signal. This geometric efficiency then is

$$\varepsilon = 1 - \frac{\text{width of the gap}}{\text{width of active area}} = 1 - \frac{7.87 \text{ mm}}{152.4 \text{ mm}} = 0.948.$$

The deadtime in the shower detectors due to high rates was calculated by studying an electron calibration run. The data was cut in the same way as the calibration data, i.e., two tracks of opposite sign were required in the shower detectors with an opening angle of less than 2 mr, but with the HC2 buss line off. Then assuming that some tracks do not register in the shower detectors because of high rates, we can calculate an efficiency

$$\varepsilon = \frac{\text{No. tracks registering in shower detector}}{\text{No. tracks}} = 0.906.$$

To obtain the correction for a given data set we scale the deadtime by the ratio of the rates in that set to the rate in the calibration run. Again the results are summarized in Table 3.

A high rate correction must also be made for the HC2 buss line. A data run in which there was a large sample of ρ mesons was examined. Cuts were made to remove electron pairs and to insure that the two tracks passed through the hadron calorimeter. Assuming then that all events are hadronic, we obtain an efficiency

$$\varepsilon = \frac{\text{No. events with HC2 on}}{\text{all events}} = 0.994.$$

To obtain the efficiency for each data set we again scale by the ratio of rates.

The $\geq 2\pi$ buss line was derived from the L x R logic of the H, V array (Fig. 18). The efficiency of this array was checked periodically by a special counter check run. The run was taken by inserting the collimators into the beam line and then triggering on B3 and the 1μ buss line. Since the H, V array was not required in the trigger their efficiency could be determined by checking to see if the proper counters were on when a reconstructed track passed through them. The following average efficiencies were found:

$$\varepsilon_{H_L} = 0.991$$

$$\varepsilon_{H_R} = 0.989$$

$$\varepsilon_{V_L} = 0.996$$

$$\varepsilon_{V_R} = 0.993.$$

Since we only require 3 of 4 H, V counters to fire, this amounts to about a 99% efficiency.

The efficiency of the PWC's enters the corrections to the data in three ways:

1. P1 buss line
2. PWC logic buss line
3. PWC efficiency for each point on a track.

From the special counter check runs described in the previous paragraph the efficiency of each plane could be determined. The average efficiencies are given in Table 4.

TABLE 4: CHAMBER EFFICIENCIES

Chamber / Plane	P0	P1	P2	P3	P4
X	0.997	0.997	0.999	0.991	0.998
V	0.992	0.994	0.999	0.997	0.996
U	0.984	0.994	0.998	0.997	0.998

The P1 buss line required two of three planes in that chamber to fire. If we assume an average probability p for each plane in P1 to register a hit, and q not to register, then the efficiency of the P1 logic for two tracks is

$$\varepsilon = 1 - (q^3 + 3q^2p)^2 \tag{34}$$

which is a negligible correction.

The PWC logic buss line required

$$\{P_2(>1)^2 \cdot P_3(>1)^2\} \cdot \{P_2\ X_L \cdot P_3\ X_L + P_2\ X_R \cdot P_3\ X_R\}. \tag{35}$$

Assuming an average efficiency $p_{2(3)}$ for the planes in chamber P2 (P3) and an inefficiency $q_{2(3)}$, it is easy to show that the overall efficiency for two tracks is

$$\begin{aligned}\varepsilon &= \{1 - (q_2{}^3 + 3q_2{}^2\ p_2)^2\}\{1 - (q_3{}^3 + 3q_3{}^2\ p_3)^2\} \\ &\quad \cdot \{2\ (2p_2p_3 - p_2{}^2p_3{}^2) - (2p_2p_3 - p_2{}^2p_3{}^2)^2\} \\ &\approx 4p_2p_3 - 6p_2{}^2p_3{}^2 + 4p_2{}^3p_3{}^3 - p_2{}^4p_3{}^4\end{aligned} \tag{36}$$

which is again a negligible correction.

The chamber efficiency for each plane from Table 4 is seen to be about 99.5%. However, most of this inefficiency is due to

the high rates from B-H pairs in the central region of the chambers. Since we are not interested in these low mass pairs, the real question of inefficiency is with the track finding program. That is, given the existence of points (hits) on a track, does the reconstruction program recognize the pattern. The track finding efficiency was calculated by generating a Monte Carlo tape that simulated ρ photoproduction. The Monte Carlo output tape was analyzed by the track reconstruction program. All tracks were found. We therefore assume the efficiency of the program and the chambers to be unity under normal operating conditions.

However, during one period of running, the PWC voltages were inadvertently lowered causing about a 10% inefficiency. Data from this period was re-analyzed with a less restrictive track fitting program which allowed for missing hits in the inefficient chambers. Eight of the seventy-nine events of the "all" sample were found in this manner. We therefore do not estimate any further inefficiency in the PWC's or track finding program.

E. Results and Conclusions

In this section we present results of calculations for the total cross section of $\gamma + Be \rightarrow \psi_{\hookrightarrow e^+e^-} X$ plots of $\frac{d\sigma}{dt}$, $\frac{d\sigma}{dK}$, and $\frac{dN}{d\cos\theta^*}$. From $\frac{d\sigma}{dt}$ we extract $(\frac{d\sigma}{dt})_{t=0}$ per nucleon from which we obtain $\sigma(\psi N)$. We also make an investigation of the di-lepton continuum ($1.2 < M < 2.8$) to determine its structure, and , finally we make comparisons to other photoproduction experiments.

1. Total Cross Section

The ψ photoproduction cross section is calculated from

$$\nu\ N_{evts} = \varepsilon\ N_A F\ B\sigma \tag{22}$$

where the factors are defined in Sec. III. D. Including all corrections from Table 3, we obtain

$$B\sigma\ (\text{"All"}) = (20 \pm 3)\ \text{nb}$$

$$B\sigma\ (\text{"Clean"}) = (15 \pm 2)\ \text{nb}.$$

The error in this calculation arises from several sources. The two major contributions, however, come from uncertainties in the spectrum measurement and from statistical fluctuations.

2. Differential Cross Section

A plot of $B\frac{d\sigma}{dt}$ is shown in Figs. 37, 38 for the "all" and "clean" samples respectively. The resulting plots are fit by these four parameter curves:

$$\text{"All"}:\ B\frac{d\sigma}{dt} = (189\ e^{31t} + 23\ e^{1.2t})\ \text{nb/GeV}^2 \tag{37a}$$

with $\chi_\nu^2 = 1.19$ and

$$\text{"Clean"}:\ B\frac{d\sigma}{dt} = (193\ e^{32t} + 17\ e^{2.0t})\ \text{nb/GeV}^2 \tag{37b}$$

with $\chi_\nu^2 = 1.45$.

Writing $\frac{d\sigma}{dt}$ ("clean") in the form of Eq. 2, we have

$$\frac{d\sigma}{dt} = 39(\text{nb/GeV}^2)\ e^{2.0t}\ [A^2\ e^{30t} + A(1 - e^{30t})]. \tag{38}$$

To extract $(\frac{d\sigma}{dt})_{t=0}$ per nucleon we correct for t_{min} and resolution in the slope by a factor ω, which yields

$$(\frac{d\sigma}{dt})_{t=0} = 39(\text{nb/GeV}^2)A^2\ (\frac{\omega}{e^{30\omega\langle t_{min}\rangle}}) \tag{39}$$

Fig. 37. $B\frac{d\sigma}{dt}$ for the "all" sample. The curve can be fit by

$$B\frac{d\sigma}{dt} = (189e^{31t} + 23e^{1.2t})\ \mathrm{nb/GeV^2}.$$

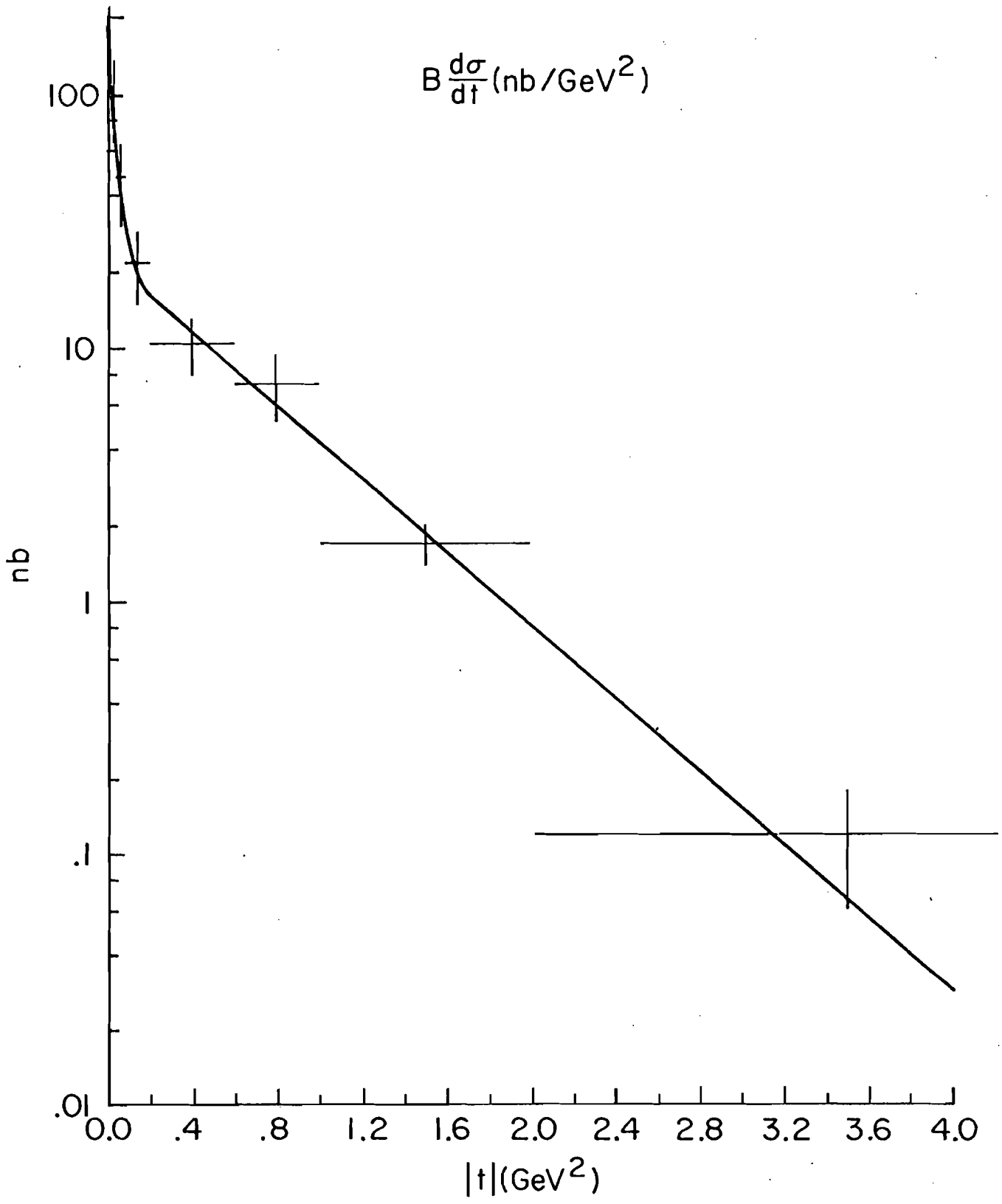
$B\frac{d\sigma}{dt}$(nb/GeV^2)
100
10
1
.1
.01
nb
0.0
.4
.8
1.2
1.6
2.0
2.4
2.8
3.2
3.6
4.0
|t|(GeV^2)

Fig. 38. $B\frac{d\sigma}{dt}$ for the "clean" sample. The curve can be fit by

$$B\frac{d\sigma}{dt} = (193e^{32t} + 17e^{2.0t})\ \mathrm{nb/GeV}^2.$$

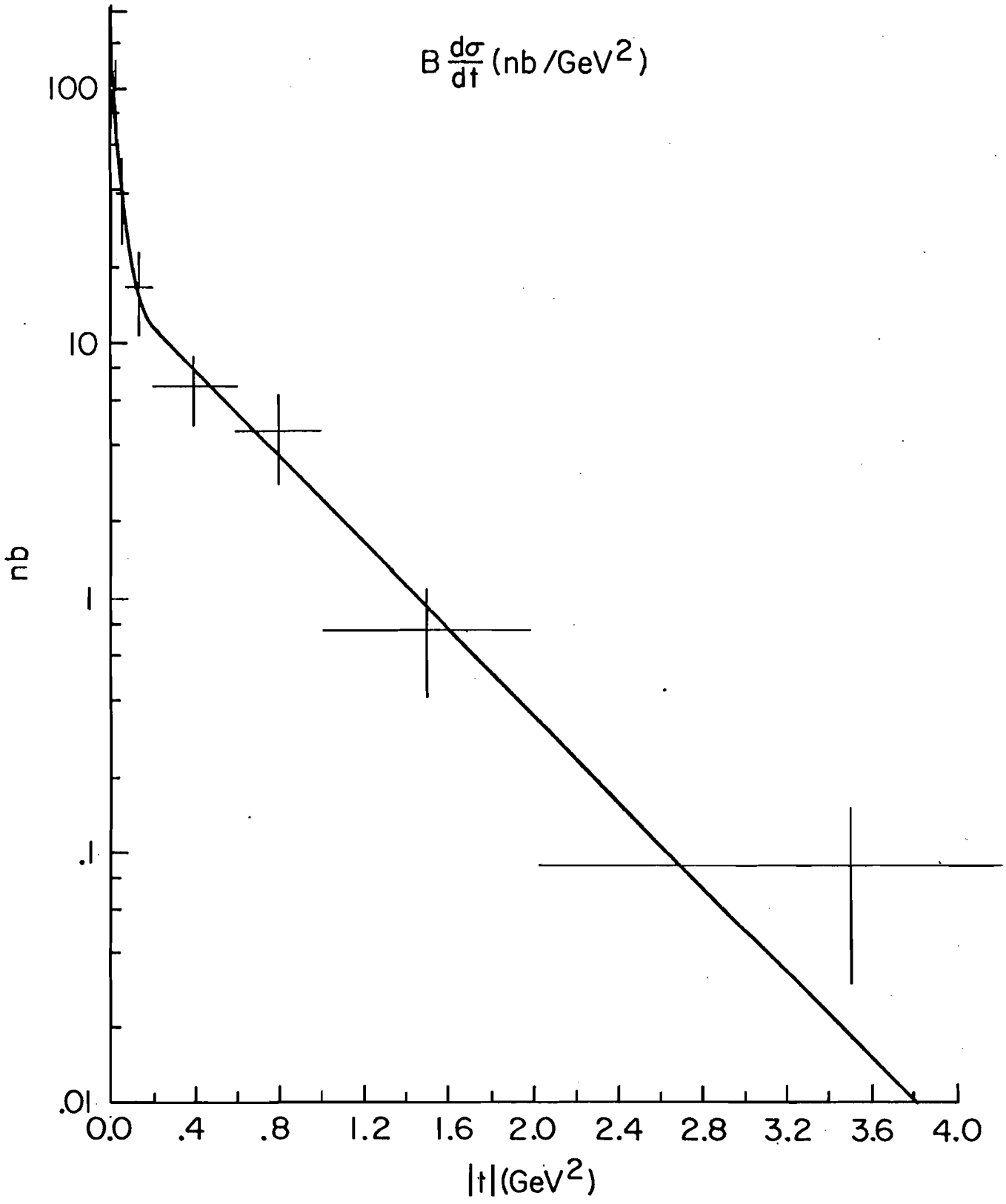
$B\frac{d\sigma}{dt}$ (nb/GeV^2)
100
10
1
.1
.01
nb
0.0
.4
.8
1.2
1.6
2.0
2.4
2.8
3.2
3.6
4.0
|t| (GeV^2)

where $\omega = 1.4 \pm 0.3$ and $\langle t_{min} \rangle = -2.2 \times 10^{-4}$. (See Appendix I.) Then per nucleon, we have

$$\frac{1}{A^2} \left(\frac{d\sigma}{dt}\right)_{t=0} = (59 \pm 15) \text{ nb/GeV}^2.$$

Assuming VMD, and that the amplitude at $t = 0$ is purely imaginary, and using $\Gamma_{ee} = 4.8 \pm 0.6$, we obtain from Eq. 12

$$\sigma\ (\psi N) = 1.3 \pm 0.3 \text{ mb}.$$

These numbers are to be compared with those obtained from ρ, ω, and ϕ photoproduction in Table 5. The ψN cross section is smaller than that for other vector mesons, but from the prediction of Eq. 13 we can conclude the ψ is a hadron.

TABLE 5: ρ, ω, ϕ CROSS SECTIONS

Particle	σ(VN) (mb)	$\left(\frac{d\sigma}{dt}\right)_{t=0}$ (μb)	Reference
ρ	27	120	3-5,36-39
ω	26	12	3-5,40-41
ϕ	13	3	3-5,42-44

3. Additional Distributions and Di-Lepton Continuum

In Fig. 39 we show a plot for the dependence of photoproduction on the photon momentum K. The average photon momentum for these events is 129 GeV. The data is consistent with a flat distribution at about 1.6 nb/GeV, but may also be rising slowly with energy.

We also show in Fig. 40 the angular distribution of the decaying electrons in the helicity frame. The angular distribution is consistent with $a(1 + \cos^2\theta^*)$ distribution which is expected from the decay of a vector meson into two fermions.

Fig. 39. $\frac{d\sigma}{dK}$ for the "all" sample. The average photon momentum is $\langle K \rangle = 129$ GeV. The cross section is consistent with being flat but could also be rising slowly with energy.

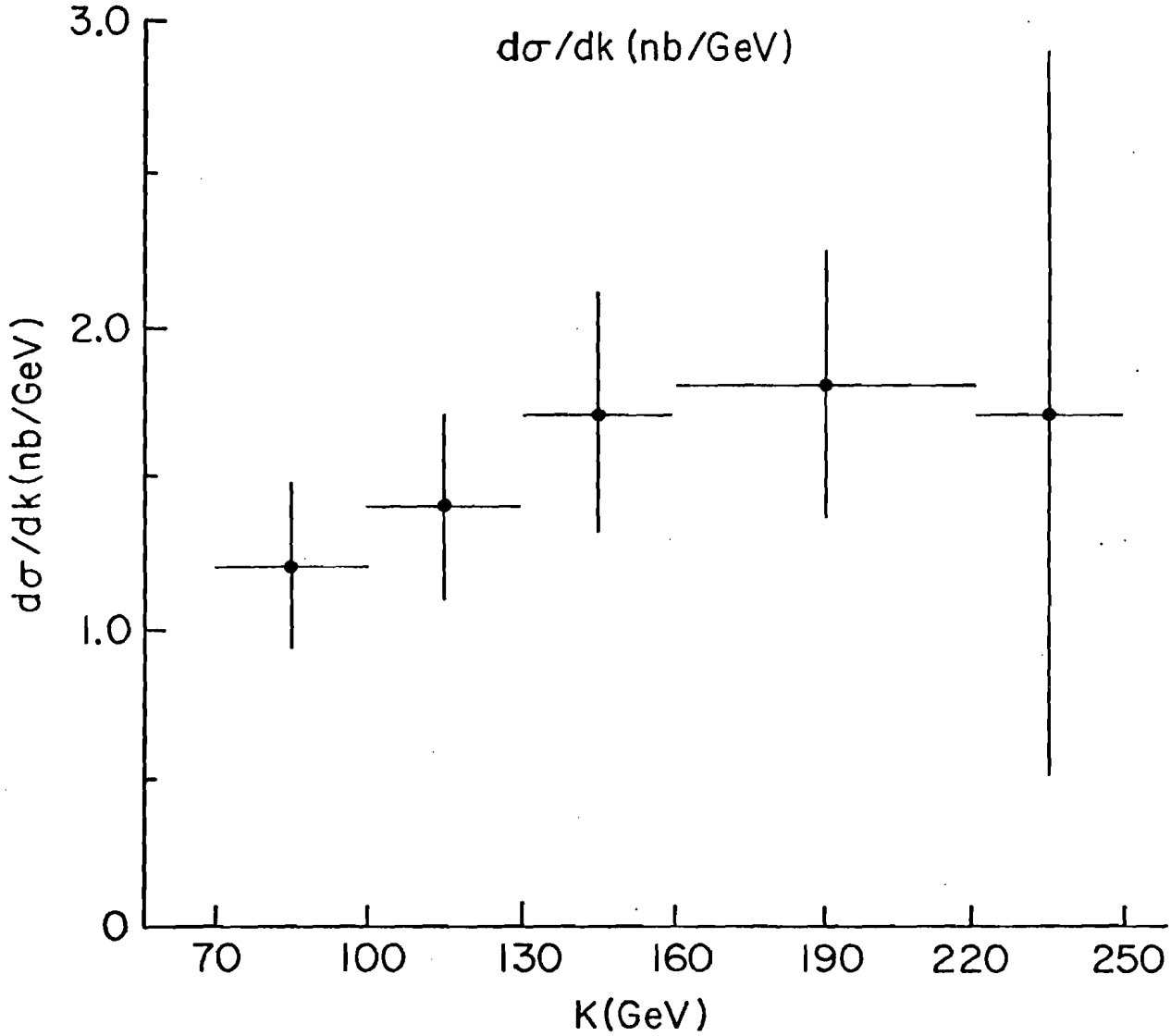
dσ/dk (nb/GeV)
3.0
2.0
1.0
0
dσ/dk (nb/GeV)
70
100
130
160
190
220
250
K(GeV)

Fig. 40. Distribution of events as a function of $\cos\theta^*$.

Three curves are plotted against the data:

1. $1 + \cos^2\theta^*$ ———
2. Constant ·—·—·
3. $\sin^2\theta^*$ ---

The data is consistent with $1 + \cos^2\theta^*$.

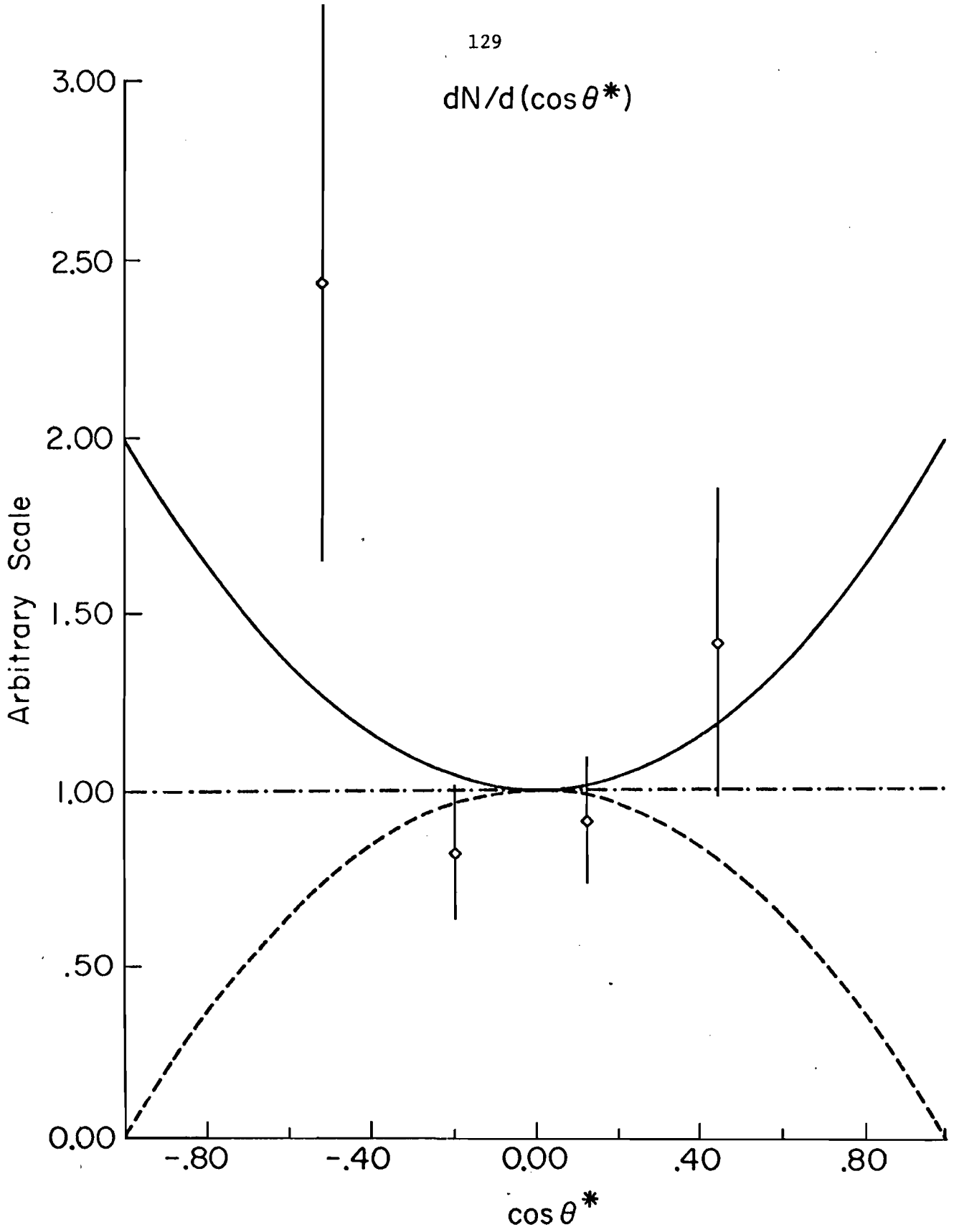
dN/d(cos θ*)
3.00
2.50
2.00
1.50
1.00
.50
0.00
Arbitrary Scale
-.80
-.40
0.00
.40
.80
cos θ*

In the continuum region ($1.2 < M < 2.8$) we expect a $1/M^4$ dependence for B-H pair production. The "clean" data is plotted in Fig. 41 and is seen to follow a $1/M^4$ fall-off. There is a deviation from the continuum in the region of 1.6 GeV. This effect does not show up in the "all" sample. The region around 1.6 GeV is where one would expect to find contributions to pair production from the decay of the ρ' and ω' mesons. However, in this data the effect is no more than a tantalizing fluctuation of about two standard deviations.

4. Comparison to Other Experiments

A summary of data taken in this experiment in both the e^+e^- and $\mu^+\mu^-$ channels is compared with data taken at SLAC and Cornell in Table 6. The data taken in both lepton channels of this experiment are self-consistent, but are about a factor of four larger than the highest energy data taken at SLAC. In Fig. 42 we plot a curve of $\sigma(\psi N)$ as a function of the invariant mass squared, s. In this plot we see that the points determined by this experiment are not at all inconsistent with the continuing rise of the cross section. In fact, based on Figs. 39, 42 it is evident that to within the statistics of the experiment the cross section is flat from at least 70-250 GeV.

Fig. 41. Log-log plot of mass distribution for the "clean" sample in the continuum region. The data follows approximately a $1/M^4$ distribution.

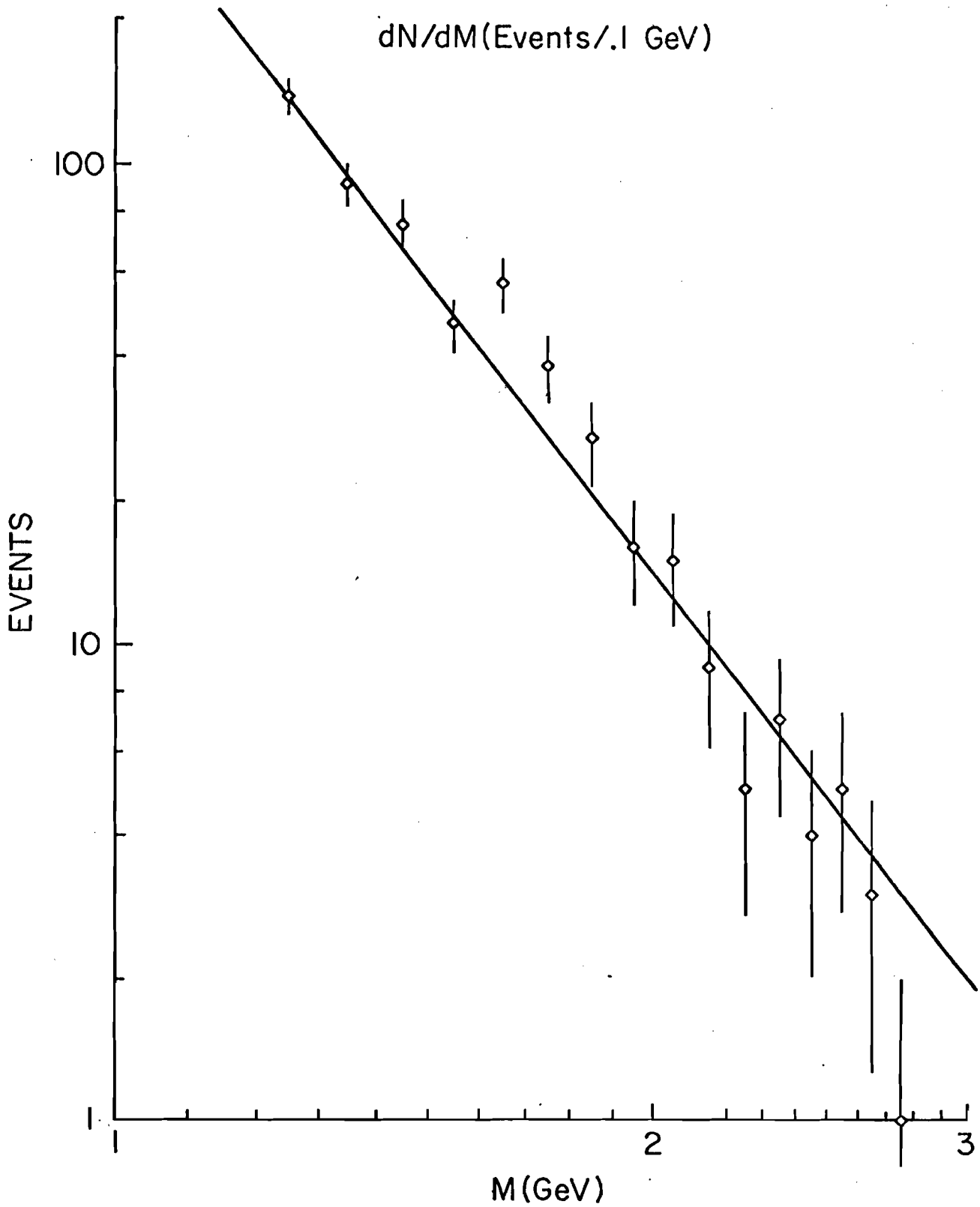
dN/dM(Events/.1 GeV)
100
10
1
EVENTS
1
2
3
M(GeV)

Fig. 42. V-N cross section for ρ, ϕ, and ψ. Data from:

		Reference
ρ:		3-5,36-39
ϕ:		3-5,42-44
ψ:		37
		38
		36
		Sec.III.E.

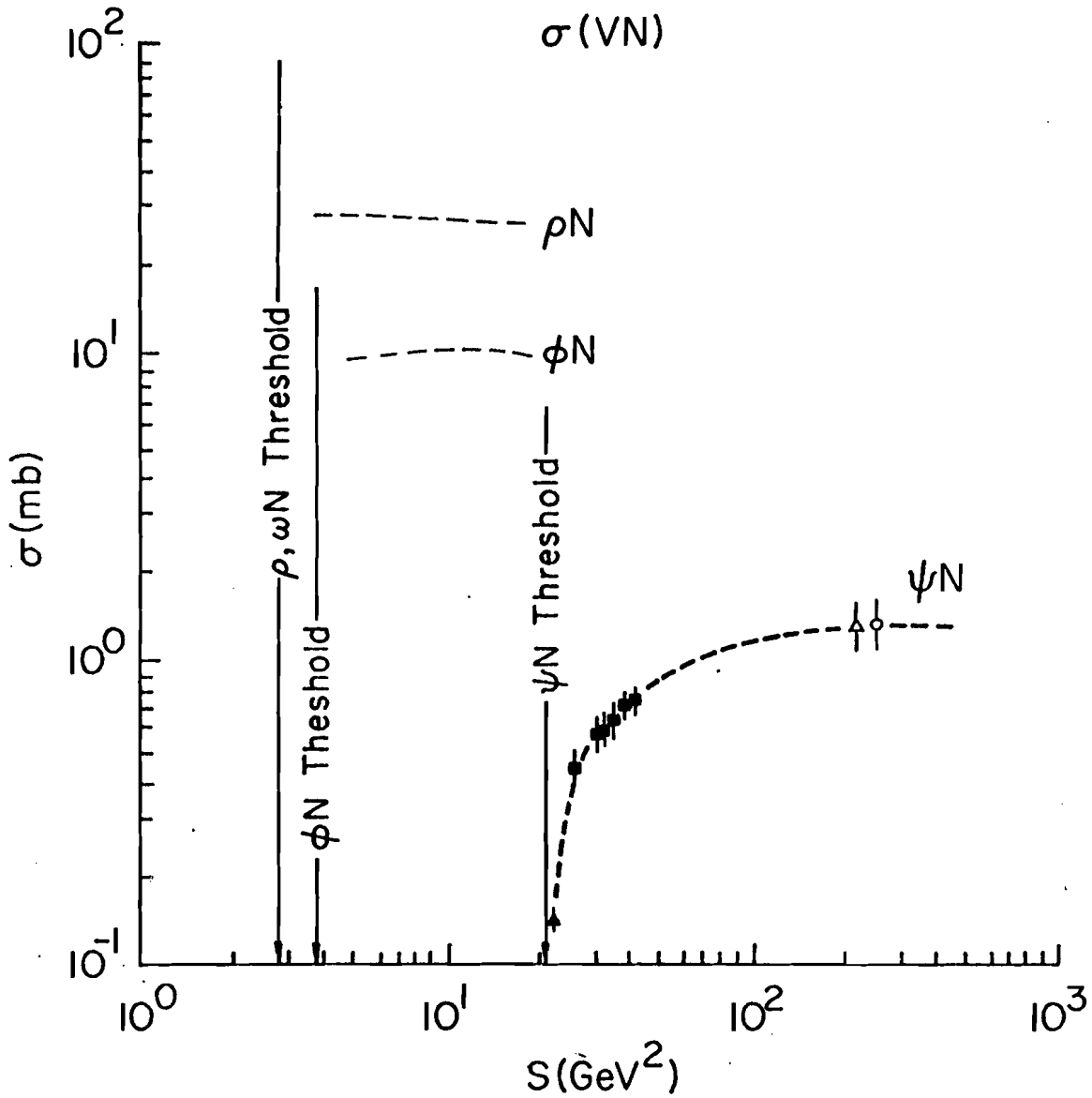
σ(VN)
ρN
φN
ψN
ρ, ωN Threshold
φN Theshold
ψN Threshold
σ(mb)
S(GeV²)
10²
10¹
10⁰
10⁻¹
10⁰
10¹
10²
10³

TABLE 6: COMPARISON OF ψ PHOTOPRODUCTION RESULTS

Target	Energy (GeV)	$(\frac{d\sigma}{dt})_{t=0}$ (nb/GeV^2)	$\sigma(\psi N)$ (mb)	Slope a (GeV^{-2})	Reference
Be	$\langle K \rangle = 116$	58.0±17.0	1.3±0.25	1.8±0.6	45, 46
Be	$\langle K \rangle = 129$	59.0±16.0	1.3±0.3	2.0±1.0	Sec.III.E.
D_2	(21.0,21.5)*	14.9± 1.2	0.8		47
	(19.0,20.0)	15.3± 0.9		2.8±0.3	
	(19.0,19.5)	12.3± 1.1			
	(17.0,17.5)	11.2± 1.0			
	(16.0,16.5)	8.6± 1.2			
	(15.0,20.0)	7.8± 1.6			
	(15.0,16.0)	6.0± 1.0			
	(13.0,13.5)	3.9± 0.8			
H_2	(19.0,19.5)	11.0± 1.1			
Be	(8-11.8,11.8)	0.8± 0.2	0.3	1.2±0.3	48

*(K,E_o) denotes the ψ energy K and the bremsstrahlung end point E_o.

We can compare the data taken in the e^+e^- channel with that of the $\mu^+\mu^-$ channel to verify the equality of the two di-lepton branching ratios. The $\mu^+\mu^-$ data was taken under the pin 1 trigger of Fig. 23 simultaneously with the 2e data, and was analyzed in a manner similar to the e^+e^- analysis. A summary of this comparison is given in Table 7. From these comparisons we obtain

$$ee/\mu\mu = 1.00 \pm 0.15.$$

TABLE 7: FURTHER COMPARISON OF DATA TAKEN IN DI-LEPTON CHANNELS IN THIS EXPERIMENT

Decay Mode	$B\sigma(\gamma\to\psi)$ (nb)	$(\frac{d\sigma}{dt})_{t=0}$ (nb/GeV^2)	Slope b (GeV^{-2})	Slope a (GeV^{-2})	$\sigma(\psi N)$ (mb)	$\langle\frac{d\sigma}{dK}\rangle$ (nb/GeV)	Reference
ee	15 ± 2	59 ± 16	42 ± 11	2 ± 1	1.3 ± 0.3	1.6	Sec.III.E.
$\mu\mu$	15	58 ± 19	48 ± 16	$1.8\pm.6$	1.3 ± 0.25	1.6	45,46

In conclusion, then, we have photoproduced the ψ meson at the highest possible energies, determined its photoproduction cross section, and its differential cross sections as functions of K and t. From this information we obtained the ψN total cross section which indicated that the ψ is a hadron. Furthermore, we have seen that (within statistics) the cross section is constant at high energy.

APPENDIX I: DETAILS OF ANALYSIS

A. Shower Detector Calibration

The purpose of the calibration runs was to determine the conversion factors (calibration constants) which translate ADC pulse height measurement into energy measurement. To derive these constants, we use a method of Lagrange multipliers. Let

N_F = ADC reading for front counter

N_B = ADC reading for back counter

p = Momentum of track

E = Energy of track deposited in shower counters.

The signature for electrons in the shower detectors is the fact that $E = p$; so we wish to minimize the function $f = E/p$ as a function of the calibration constants. Defining $\varepsilon_F = N_F/p$ and $\varepsilon_B = N_B/p$, and introducing the calibration constants G and α, we write

$$f = E/p = G/p\ (\alpha N_F + N_B),$$

or (40a)

$$f = G\ (\alpha\varepsilon_F + \varepsilon_B)$$

then defining $\beta = G\alpha$ and $\gamma = G$

$$f = \beta\ \varepsilon_F + \gamma\ \varepsilon_B. \tag{40b}$$

We can calculate the variance (width) δf of f in terms of β, γ and the measured pulse heights. Then we can minimize δf subject to the constraint $\overline{f} = 1$ by use of Lagrange multipliers. The variance is

$$\delta f = \sum_{i=1}^{N} (f_i - \bar{f})^2$$

$$= \sum f_i^2 - 2\bar{f} \sum_i f_i + N\bar{f}^2 \tag{41}$$

$$= \sum_{i=1}^{N} f_i^2 - N\bar{f}^2$$

where N is the number of tracks in the data sample. Substituting for f

$$\delta f = \sum_i (\beta^2 \varepsilon_{F_i}^2 + \gamma^2 \varepsilon_{B_i}^2 + 2\gamma\beta\ \varepsilon_{F_i}\ \varepsilon_{B_i}) - \frac{1}{N} \{\Sigma(\beta\varepsilon_{F_i} + \varepsilon_{B_i})\}$$

$$= \beta^2 \{\Sigma\varepsilon_{F_i}^2 - \frac{1}{N} (\Sigma\varepsilon_{F_i})^2\} + \gamma^2 \{\Sigma\varepsilon_{B_i}^2 - \frac{1}{N} (\Sigma\varepsilon_{B_i})^2\} \tag{42}$$

$$+ 2\gamma\beta \{\Sigma\varepsilon_{F_i}\ \varepsilon_{B_i} - \frac{1}{N} \Sigma\varepsilon_{F_i}\ \Sigma\ \varepsilon_{B_i}.$$

Defining the sums

$$\begin{aligned} S_2 &= \Sigma\varepsilon_{F_i} \\ S_3 &= \Sigma\varepsilon_{F_i}^2 \\ S_4 &= \Sigma\varepsilon_{B_i} \\ S_5 &= \Sigma\varepsilon_{B_i}^2 \\ S_6 &= \Sigma\varepsilon_F\varepsilon_{B_i} \end{aligned} \tag{43}$$

and

$$\begin{aligned} A_1 &= S_3 - S_2^2/N \\ A_2 &= S_5 - S_4^2/N \\ A_3 &= S_6 - S_2S_4/N \\ A_4 &= S_4/N \\ A_5 &= S_2/N, \end{aligned} \tag{44}$$

we can rewrite

$$\delta f = A_1\ \beta^2 + A_2\ \gamma^2 + 2\gamma\beta\ A_3. \tag{45}$$

We introduce a Lagrange multiplier λ and the function

$$h = 1 - \bar{f} = 1 - \frac{1}{N}\{\beta S_2 + \gamma S_4\}$$
$$= 1 - \beta A_5 - \gamma A_4. \tag{46}$$

We now minimize the function $\delta F + \lambda H$ with respect to β, γ, λ

$$\frac{\partial}{\partial\beta}(\delta f + \lambda h) = 0 = 2\beta A_1 + 2\gamma A_3 - \lambda A_5 \tag{47a}$$

$$\frac{\partial}{\partial\beta}(\delta f + \lambda h) = 0 = 2\gamma A_2 + 2\beta A_2 - \lambda A_4 \tag{47b}$$

$$\frac{\partial}{\partial\beta}(\delta f + \lambda h) = 0 = 1 - \beta A_5 - \gamma A_4. \tag{47c}$$

Eliminating λ from (47a) and (47b):

$$2\beta A_4 A_1 + 2\gamma A_4 A_3 - 2\gamma A_2 A_5 - 2\beta A_3 A_5 = 0$$

or (48)

$$\beta(A_4 A_1 - A_3 A_5) + \gamma(A_4 A_3 - A_2 A_5) = 0.$$

Then from (47c),

$$\gamma = \frac{1 - \beta A_5}{A_4} \tag{49}$$

so

$$\beta(A_4 A_1 - A_3 A_5) + \frac{1 - \beta A_5}{A_4}(A_4 A_3 - A_2 A_5) = 0. \tag{50}$$

$$\beta = \frac{A_5 A_2 - A_3 A_4}{A_4{}^2 A_1 + A_5{}^2 A_2 - 2A_3 A_4 A_5}. \tag{51}$$

Using this method we obtain calibration constants β, γ for each counter.

B. Track Reconstruction

The first level editing of the data tapes involved the transformation of encoded MWPC wire addresses into x, y, z

coordinates and the pattern recognition to translate these hits into reconstructed tracks passing through the spectrometer.

Z coordinates were known from survey information for each of the 15 MWPC planes. Internal chamber coordinates were related by the series of equations:

$$u = Cy + Sx \qquad v = Cy - Sx \qquad x = x \tag{52}$$

where C and S are the cosine and sine of $\tan^{-1}(.2) = 11°$. Coordinates M_i were obtained from the wire address in the i'th plane by

$$M_i = (A - J/2 - O_i) * W_i \tag{53}$$

where A and J are the address and adjacency, O_i is the origin in the i'th plane, and W_i is the wire spacing. The origin O_i was determined from a straight line fit to muon tracks passing through the spectrometer when the magnetic field was off.

Each track found by the pattern recognition program was fit to

$$x = \alpha z + \beta \qquad y_{z\leq 0} = \rho z + \gamma \qquad y_{z\geq 0} = \lambda z + \gamma. \tag{54}$$

A constraint that the y tracks must intersect at z = 0 has been put into these equations. The fit was obtained by simultaneously minimizing

$$\chi^2 = \sum_{t=0}^{15} \frac{f_i}{\sigma_i^2} (M_i - C_i(\alpha,\beta,\rho,\lambda,\gamma))^2 \tag{55}$$

with respect to α, β, ρ, λ, and γ where the C_i are obtained by inserting Eqs. 54 into Eqs. 52, $\sigma_i = W_i/12$, and $f_i = 0$ if there was no i'th point on the track or $1/(J+1)^2$ if there was.

All events on the original data tape were passed along to the edited tape. Also included for each event were the number

of tracks found, pointers to the wires addresses used for each track, and the fits to each track. In order to be considered a track in the initial reconstruction, the track must have no more than one missing point and have a mean squared error of less than one wire spacing squared per point.

Due to inefficiencies in some proportional chambers during certain data taking periods, it became necessary to make a second reconstruction pass on the edited tapes. The second reconstruction searched for additional tracks among the hits not used for the tracks in the initial reconstruction. Track requirements were relaxed to require:

1. At most one missing x point in P0-P4
2. At most one missing v point in P1-P4
3. At most one missing u point in P1-P4
4. Both P4 and P1 must have either a u or v point.

Additional tracks were found in about 5% of the events for periods of high efficiency running and in up to 14% during periods of lower efficiency.

C. Kinematic Calculations

1. Mass

The mass of the lepton pairs was determined from the momentum vectors of the pair (measured by the spectrometer) and the target bremsstrahlung photon energy (measured by the shower detectors). The bremsstrahlung problem was critical for several reasons:

a. Targets of as much as 25% X_o were used.

b. For the ψ events $\langle E_{\gamma B}\rangle \approx 5$ GeV. The resolution of the shower detectors at 5 GeV is

$$\frac{\Delta E}{E} = 20\%.$$

c. For high energy events the shower detectors for the electron and bremsstrahlung photon were usually the same detectors.

These three factors had the net effect of producing a huge number of bremsstrahlung photons which were not resolved very well.

The mass was calculated according to Eq. 20.

$$M^2 = 2me^2 + (p^+ + E_{\gamma B}{}^+)(p^- + E_{\gamma R}{}^-)(1 - \cos\theta_L)$$

where $E_{\gamma B}$ was defined in the following manner:

1. If the electron and bremsstrahlung photon did not share the same shower detectors, then $E_{\gamma B}$ was simply the energy deposited in the detectors at which the photon "pointed."
2. If the electron and bremsstrahlung photon shared the same shower detectors, then $E_{\gamma B}$ was ambiguous. An algorithm was made for extracting $E_{\gamma B}$ in this case. If

$$\frac{E}{p} > 1 + 0.87\left(\frac{\Delta E}{E}\right) \qquad \left(0.87\left(\frac{\Delta E}{E}\right) = 2\sigma\right) \tag{56a}$$

in the electron's shower detectors, then,

$$E_{\gamma B} = E - p\left(1 + 0.87\,\frac{\Delta E}{E}\right). \tag{56b}$$

Analyzing the data in this manner, seventy-one ψ events were found in the "all" sample. A second pass was then made on the events in the region $2.3 < M < 3.4$ with the less restrictive requirements that if

$$\frac{E}{p} > 1, \tag{56c}$$

then

$$E_{\gamma B} = E - p. \tag{56d}$$

An additional eight events were found from this pass which satisfied the $E_{\gamma B}/E_{tot} < 0.75$ cut.

2. K And t

Since the target recoil in Fig. 1b was not measured, the interaction was determined by a 0 constraint fit. (Only the magnitude and the direction of the electron momentum were measured.) A quasi-elastic calculation was employed to improve the calculation of K and t. From Fig. 1b

$$-t = (p_i - p_f)^2 = 2M_N{}^2 - 2M_N E_f \tag{57}$$

and

$$E_f - M_N = K - (E_+ + E_-). \tag{58}$$

Combining (57) and (58) we have

$$K = (E_+ + E_-) + \frac{2}{2M_N} \tag{59}$$

which is an improved relation from the assumption $K \approx (E_+ + E_-)$.

We can also write

$$\begin{aligned} -t &= (K' - K)^2 \\ &= M^2 - 2K\{(E_+ + E_-) - \hat{K}\cdot(\vec{p}_1 + \vec{p}_2) \end{aligned} \tag{60}$$

and substituting (59) we have

$$-t = M^2 - 2\{(E_+ + E_-) + \frac{t}{2M_N}\} \cdot \{(E_+ + E_-) - \hat{K} \cdot (\vec{p}_1 + \vec{p}_2)\}. \tag{61}$$

The photon momentum K is not measured by the experiment, but its average direction $\hat{K}$ is known from the calibration runs.

D. Mass Resolution

We wish to calculate $\langle\delta M\rangle$ associated with Eq. 21. In the high energy small angle limit, Eq. 20 becomes

$$M^2 \approx E_+E_- \ \theta_L. \tag{62}$$

Differentiating we have

$$\frac{\Delta M}{M} = \frac{1}{2}\frac{\Delta E_+}{E_+} + \frac{1}{2}\frac{\Delta E_-}{E_-} + \frac{\Delta\theta}{\theta} . \tag{63}$$

But

$$E = p + E_{\gamma B}$$

and from Eq. 14, 15

$$\frac{\Delta p}{p} = \frac{(\pm\ 0.035)p}{100\ \text{GeV}}$$

$$\frac{\Delta E_{\gamma B}}{E_{\gamma B}} = \frac{0.39}{\sqrt{E_{\gamma B}}} + 0.026$$

also

$$\Delta\theta \approx 0.3\ \text{mr}.$$

Substituting average values for ψ decay energies and angles we have

$$\left.\frac{\Delta M}{M}\right|_{M=3.1} \approx 7\%$$

or $\langle\delta M\rangle \approx 100$ MeV (1σ) at $M = 3.1$ GeV.

E. Bremsstrahlung Energy Loss

The energy lost by an electron of incident energy E at position X in a target of radiation length X_o is

$$Q(x) = E(1 - e^{-X/X_o}). \tag{64}$$

We expect a spectrum of radiated photons given by

$$N_{\gamma B}(E_{\gamma B})\ dE_{\gamma B} = n(x)\ \frac{dE_{\gamma B}}{E_{\gamma B}} \tag{65}$$

where $N_{\gamma B}$ is the number of photons of energy $E_{\gamma B}$ radiated away and n is a factor to be determined. The energy lost to bremsstrahlung becomes

$$Q(x) = \int_0^E N_\gamma(E_{\gamma B}) E_{\gamma B}\, dE_{\gamma B} = \int_0^E n\, dE_{\gamma B}$$

or

$$Q(x) = n(x)\, E = E\,(1 - e^{-X/X_o}) \tag{66}$$

then

$$\langle n \rangle = \frac{1}{L} \int_0^L (1 - e^{-X/X_o})\, dX$$

$$\approx \frac{1}{2}\, {}^{L}/_{X_o} \tag{67}$$

for small target thicknesses L.

The electron data was cut such that $E_{\gamma B}/E < 0.75$ (see Sec. III). So the probability p of radiating away more than 75% of the electron's energy is

$$p = \int_{0.75}^{1.0} N_{\gamma B}\,(E_{\gamma B})\, dE_{\gamma B} = \langle n \rangle \int_{0.75}^{1.0} \frac{dE_{\gamma B}}{E_{\gamma B}} = 0.357\, \langle n \rangle. \tag{68}$$

For two tracks then the probability for either one to radiate $E_{\gamma B} > 0.75\, E$ is

$$(\nu - 1) = p + p - p^2 \tag{69}$$

where ν is the bremsstrahlung correction factor in Eq. 22.

F. <u>t Resolution</u>

The resolution of the apparatus was such that the measured forward slope in the plot of $\frac{d\sigma}{dt}$ would be smaller than the actual slope. A correction ω (Eq. 39) is made for this effect by studying the Monte Carlo generations for ψ production. Events were

generated with a forward slope of e^{38t}. Comparing the generated slope with that calculated by the spectrometer with all resolutions folded in we get a weighted correction factor

$$\omega = \frac{19(1.16) + 25(1.71) + 14(1.23)}{58} = 1.4 \pm 0.3$$

for the "clean" events. This correction factor is fairly constant throughout the range of slopes from 30-50.

APPENDIX II: LIGHT PULSER SYSTEM

In order to maintain a reliable measurement of electromagnetic showers over an extended period of time, it was necessary to provide a monitor of the stability of the shower counters. The requirements for such a monitor are the following:

A. Stability of approximately 5% for a period of several months.

B. Long life time on the order of 10^9 pulses.

C. Ability to monitor many counters at once.

D. Production of signals comparable to those produced by electromagnetic showers.

E. Mechanical, optical, and electrical simplicity as well as stability.

Such a monitoring system could then be used for testing of tubes and bases, comparisons between tubes, and monitoring of the stability of counters. The best method of achieving these requirements is with a light pulser system.

Over the years many light pulsers have been built for monitoring counters and detectors. Considerable insight can be gained from a study of these devices.[49,50] The light pulser described here has, after many trials and errors, met all the requirements listed in the previous paragraph. A diagram of the pulser and associated electronics is shown in Figs. 43-45. At the heart of the system is a neon glow lamp (General Electric NE 30). The lamp is fired by a high voltage pulse. Light is collected in a lucite rod wrapped in aluminum foil. The rod serves as a mixing block making the light somewhat more uniform.

Fig. 43. Light pulser box.

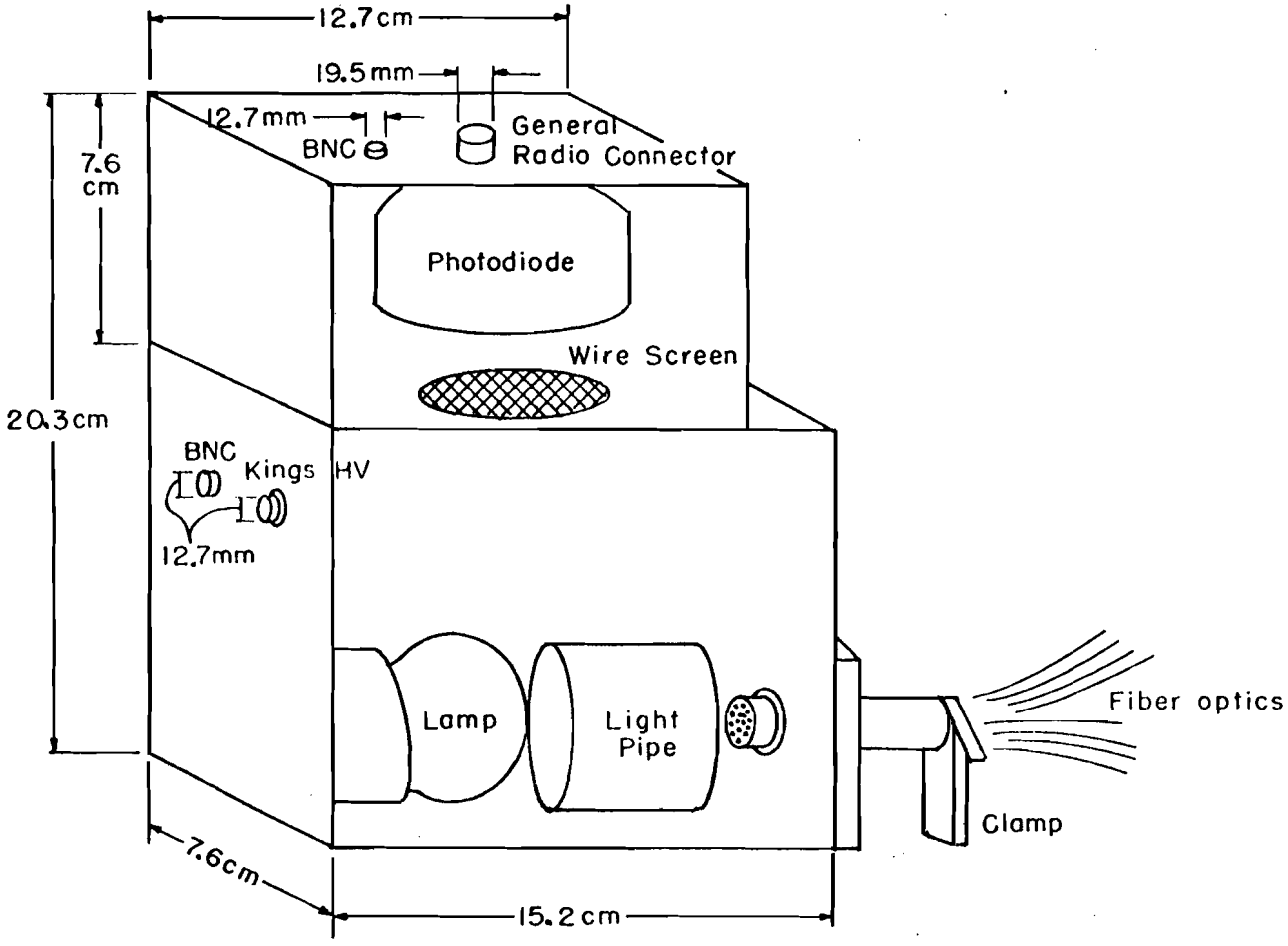
12.7cm
19.5mm
12.7mm
BNC
General
Radio Connector
7.6
cm
Photodiode
Wire Screen
20.3cm
BNC
Kings
HV
12.7mm
Lamp
Light
Pipe
Fiber optics
Clamp
7.6cm
15.2 cm

Fig. 44. Light pulser circuit.

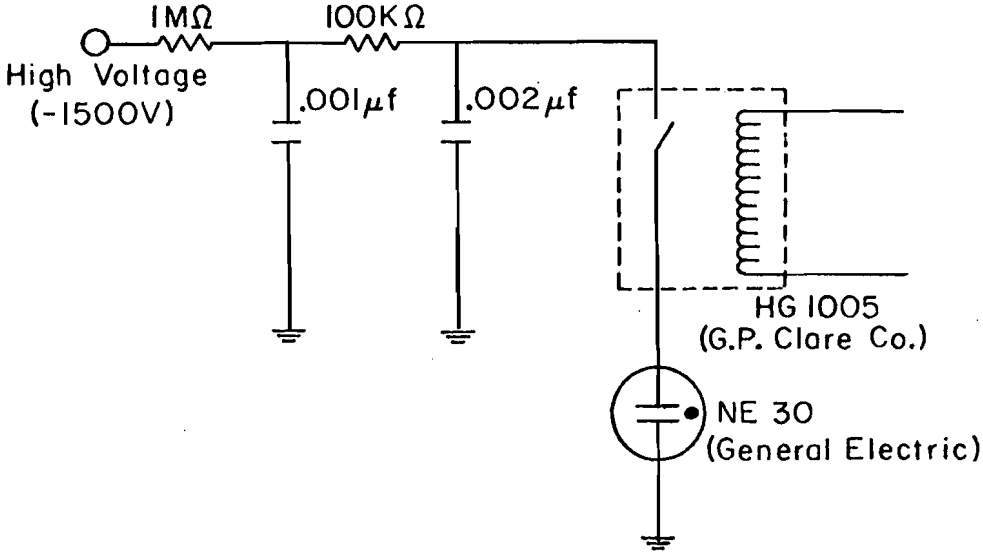
1MΩ
100KΩ
High Voltage
(-1500V)
.001μf
.002μf
HG 1005
(G.P. Clare Co.)
NE 30
(General Electric)

Fig. 45. Photodiode circuit.

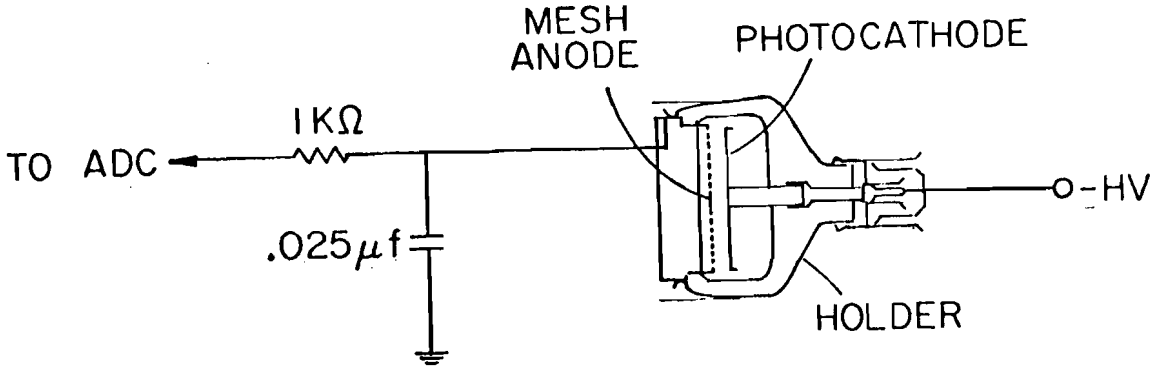
MESH
ANODE
PHOTOCATHODE
1KΩ
TO ADC
-HV
.025μf
HOLDER

Light from the rod is then incident on bundles of fiber optics (DuPont "Crofon 1610" fiber optics). Each bundle contains sixty-four "Crofon" light guides 0.25 mm in diameter. The bundles are held firmly in place by an aluminum plate. Four bundles 2 m long are fanned out to each tube in the shower counter array. Because of the physical and mechanical independence of the shower counter banks, there is a light pulser for each bank mounted on the bank itself. Each group of four bundles is potted in a lucite vial 6.3 mm in diameter and 7.6 cm long with one end sealed with a piece of lucite 1.5 mm thick and 6.3 mm in diameter. This end of the vial is in turn glued to the face of the tube (Amperex "58-AVP") in the shower counter box.

The circuitry for firing the lamp is also located in the light pulser box. It consists of a set of charging resistors and capacitors, and a mercury wetted reed relay (C.P. Clare Co. HG-1005). A pulse, 6 V in amplitude and 4 msec long energizes the coil of the relay causing the contacts to close. The 0.001 μF capacitor then discharges through the lamp when the relay is closed. The relay is mercury wetted thus eliminating contact bounce and increasing life time to about 10^9 operations.

Attached to the light pulser box is a photodiode (ITT FW114A) which monitors the stability of the lamp. A photodiode is more stable than any other photomultiplier tube because it only has one stage and therefore is the best way to monitor the performance of the light pulser. This particular photodiode is linear over a range of nine orders of magnitude from a dark

current of 5 nA to a maximum of 4 A at 2000 V. The tube has an S-20 spectral response which means the photocathode has a peak quantum efficiency at about 4200 Å. The quantum efficiency falls from a peak of about 10% at 4200 Å to about 6% for the neon lamp.

The light pulser was used to test all tubes and base designs for the shower counters. It was known from tests at SLAC how the counters responded for electrons of 3, 6 and 10 GeV/c momentum. Expected response could be extrapolated to 100 GeV/c for use at FNAL energies, so the light pulser was designed accordingly to reproduce light levels of a 100 to 300 GeV shower. The proper tube base, i.e., one linear in pulse height response to several hundred GeV, was then designed (see Fig. 46). Using this new base and the light pulser, all tubes were tested. The testing procedure was the following:

A. The tube was placed in a light tight box with a jig, as shown in Fig. 47a, fitted over the face of the tube.

B. The gain and focusing pots were alternately adjusted to give a maximum response when light from the light pulser was incident on the tube at Position 5.

C. The uniformity of the response for the tube was then found by placing the light source in four other positions across the face of the tube.

D. One modification was made to the light pulser for the purpose of checking linearity. A set of rotating Polaroid filters was placed in front of the lamp.

Fig. 46. Seven stage phototube base for Amperex 58 AVP.

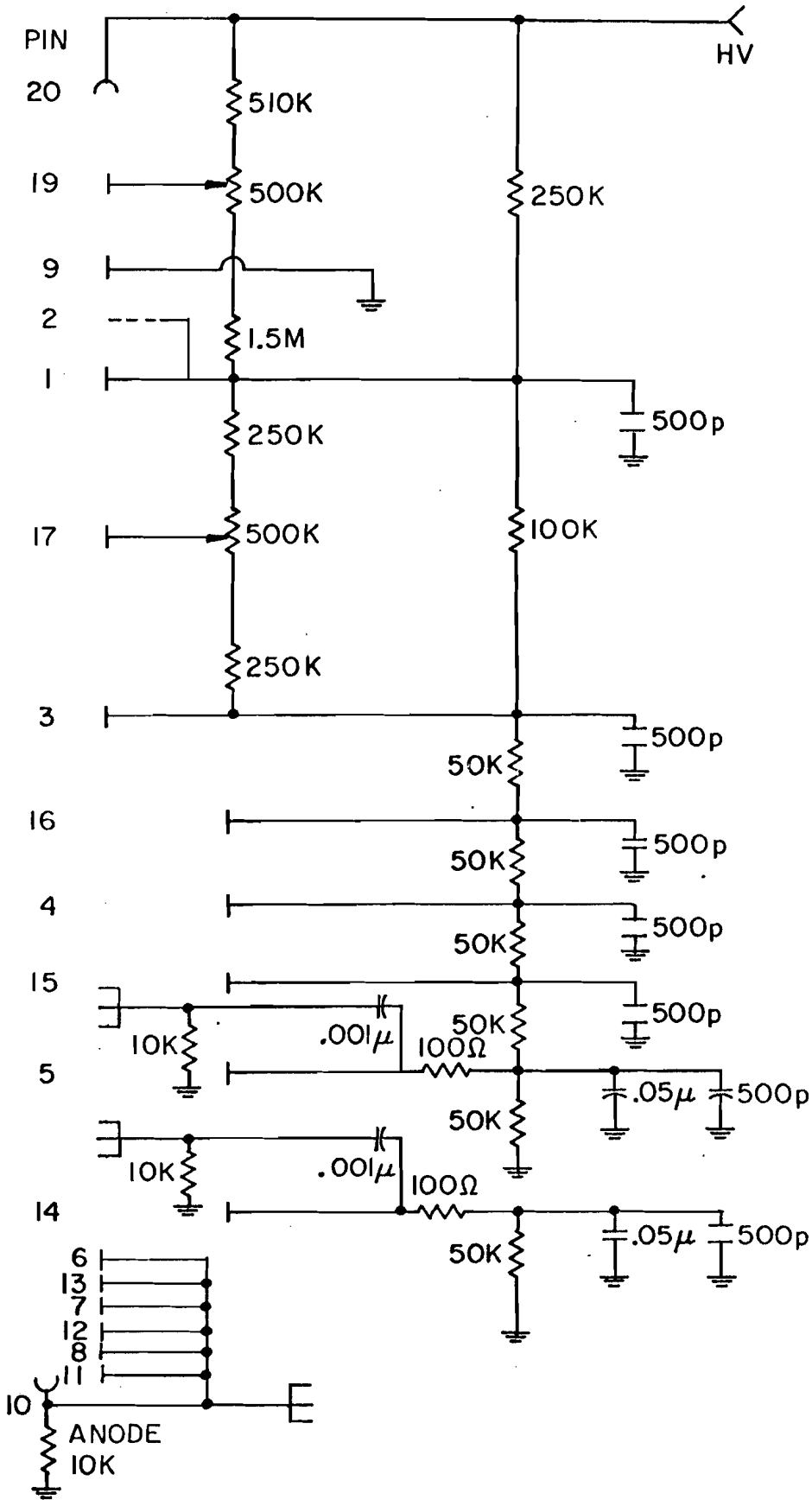
PIN
20
19
9
2
1
17
3
16
4
15
5
14
6
13
7
12
8
11
10
HV
510K
500K
1.5M
250K
500K
250K
250K
100K
500p
500p
50K
500p
50K
500p
50K
500p
10K
.001μ
100Ω
.05μ
500p
50K
10K
.001μ
100Ω
.05μ
500p
50K
ANODE
10K

Fig. 47. Uniformity tests.

a. Position jig for testing the phototube's uniformity at several positions across the face.

b. Typical results of phototube uniformity.

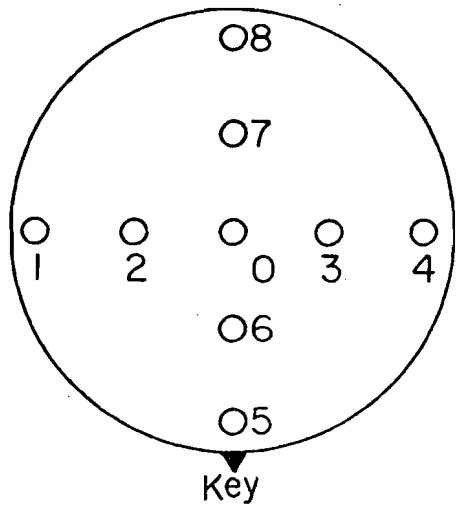
8
7
1
2
0
3
4
6
5
Key

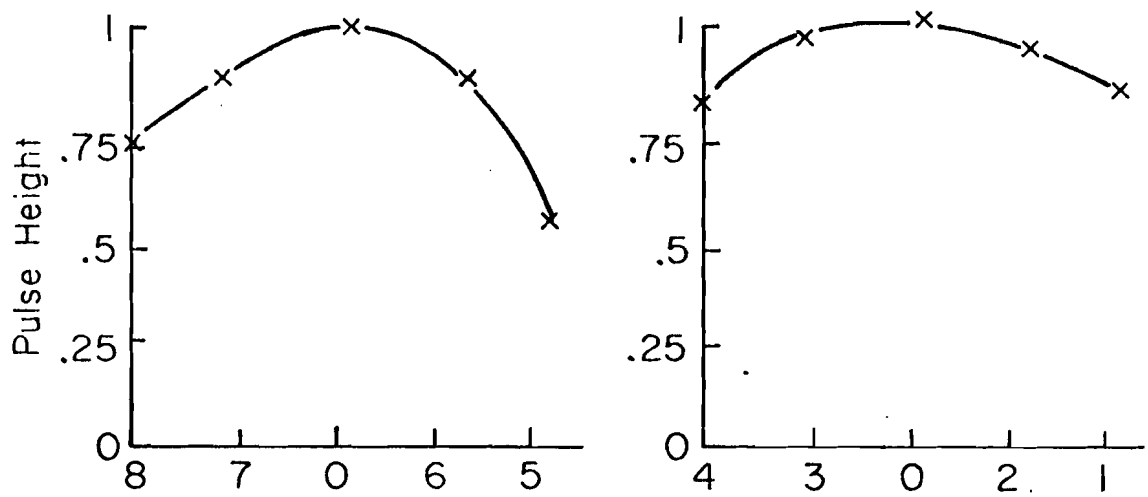
Pulse Height
1
.75
.5
.25
0
8
7
0
6
5
1
.75
.5
.25
0
4
3
0
2
1

By rotating the axes of polarization in the filters, light levels from 0 to 300 GeV could be simulated. The results of these tests for a typical tube are shown in Fig. 47b.

One light pulser was installed on each of the four shower counter banks on a small platform which extended out from the bank. During a data taking run, the light pulsers were fired several times at the beginning of the run and again after every one hundred beam spills. The triggering of the light pulsers was computer controlled and occurred between spills. The light pulsers were fired alternately about forty times each. The pulse height from each counter and photodiode was integrated by ADC and the result written on disk and magnetic tape. At the end of the run the cumulative results were printed out. In this way all shower counters were monitored run by run. The data on tape could also be analyzed to correlate long term averages and trends. Over a running period of several months, the average sort of reliability for the detectors is given in Table 8.

TABLE 8: PHOTOTUBE STABILITY

Tube	Stability
FW114A	$\pm$ 1%
58 AVB	$\pm$ 2.5%

The four light pulsers on the shower counters have been in operation for over a year without any problems. The light pulsers have proved to be a very stable and reliable system for monitoring the shower counters.

GLOSSARY

Apparatus:

AB: Counters just downstream of target which signal non-diffractive events, AB1, AB2.

A_μ: Pre-target anti-counters, A0-A6.

AW: Wide angle anti-counters mounted behind P1, AW1-4.

EF: Front electromagnetic shower detectors, EF1-22.

EB: Back electromagnetic shower detectors, EB1-24.

H: Horizontal trigger counters, H1-12.

HC: Hadron calorimeter, HC1-20.

M1: Horizontal bending magnet.

M2: Vertical bending magnet.

PWC: Proportional wire chamber, P0-P4.

Q: Quantameter or quantameter reading in Coulombs.

SEM: Secondary emission monitor.

SWIC: Segmented wire ion chamber.

T: Target counters, mounted around target T1-8.

X_o: Radiation length.

X,V,U: PWC signal planes, X is vertical, V and U are crossed at an angle of 11° to the horizontal.

X,Y,Z: Axes of left handed co-ordinate system used in this experiment where up is positive Y, downstream is positive Z and the origin is at the center of magnet M2.

$_\mu$H: Horizontal muon detectors, $_\mu$H1-22.

$_\mu$V: Vertical muon detectors, $_\mu$V1-18.

Electronics:

ACE: Buffer memory and associated electronics.

ADC: Analog to digital converter (pulse area integration).

BPI: Bytes per inch.

CR: Coincidence register.

(L + R): Left or right side of H, V array.

(L x R): Left and right side of H, V array.

MG: Master gate.

P1(2/3): 2 of 3 planes in P1.

$P2(>1)^2$: Greater than 1 hit in 2 planes of P2.

$P2X_R$: Hit in right side of X plane of P2.

TGI: Trigger input generator.

TGO: Trigger output generator.

Σ logic: Sum logic.

Σ2: Xerox Data Systems computer.

Kinematics:

E: Energy of electron.

$E_{\gamma B}$: Energy of target bremsstrahlung photon.

K: Momentum of the beam photon.

M: Mass of e^+e^- pair.

m_e: Mass of electron.

p: Momentum of electron.

p_T: Single electron transverse momentum.

θ_L: Opening angle of e^+e^- pair in the lab.

θ^*: Angle between the electron and the ψ in the cm frame.

Measurements:

A: Atomic weight of Be.

A(K): Acceptance as a function of photon momentum.

B: Branching ratio of $\psi \to e^+e^-$.

$\frac{dN}{dK}$:	Photon spectrum.
F:	Useful photon flux.
FWHM:	Full width at half maximum.
L:	Length of target.
"L":	Effective length of target.
N°:	Avagadro's number.
N_A:	Effective number of atoms in the target.
r.f.:	Radio frequency.
ε:	Efficiency correction.
ν:	Correction factor for the bremsstrahlung energy cut.
ρ:	Density of Be (or ρ meson).
σ:	Cross section (or possibly standard deviation).

Theory:

B-H:	Bethe-Heitler.
c:	Charmed quark.
$j_\mu^{em}(x)$:	Hadronic electromagnetic current.
J^{PC}:	J is the total angular momentum, P is the parity and C is charge conjugation.
VMD:	Vector meson dominance model.
$V_\mu(x)$:	Vector meson field.
s:	Strange quark.
γ_V:	Photon-vector meson coupling constant.
Γ:	Decay width.

LIST OF REFERENCES

1. M. Ross and L. Stodolsky, Phys. Rev. 149, 1172 (1966).
2. L. Stodolsky, Phys. Rev. Letters 18, 135 (1967).
3. G. Wolf in Proceedings of the 1971 International Symposium on Electron and Photon Interactions at High Energies, 190 Cornell (1971).
4. K. Gottfried in Proceedings of the 1971 International Symposium on Electron and Photon Interactions at High Energies, 222 Cornell (1971).
5. D. W. G. S. Leith in Hadronic Interactions of Electrons and Photons, Scottish Universities Summer School in Physics (1970).
6. S. Hayes, et al., Phys. Rev. Letters 24, 1369 (1970).
7. D. R. Earles, et al., Phys. Rev. Letters 25, 1312 (1970).
8. J. D. Bjorken and S. L. Glashow, Phys. Lett. 11, 255 (1964).
9. S. L. Glashow, et al., Phys. Rev. D2, 1285 (1970).
10. S. Weinberg, Phys. Rev. Letters 19, 1264 (1967).
11. S. Weinberg, Phys. Rev. Letters 27, 1688 (1971).
12. G. 't Hooft, Nucl. Phys. B35, 167 (1971).
13. C. E. Carlson and P. G. O. Freund, Phys. Lett. 39B, 349 (1972).
14. M. K. Gaillard, et al., Rev. Mod. Phys. 47, 277 (1975).
15. G. Zweig, CERN Report TH412 (1964).
16. J.-E. Augustin, et al., Phys. Rev. Letters 33, 1406 (1974).
17. G. S. Abrams, et al., Phys. Rev. Letters 33, 1453 (1974).
18. A. M. Boyarski, et al., Phys. Rev. Letters 34, 1357 (1975).
19. G. S. Abrams in Proceedings of the 1975 International Symposium on Electron and Photon Interactions at High Energies, SLAC (1975).
20. H. Harari in Proceedings of the 1975 International Symposium on Electron and Photon Interactions at High Energies, SLAC (1975).

21. M. V. Han and Y. Nambu, Phys. Rev. 139B, 1006 (1965).

22. F. Gilman in Proceedings of the 1975 International Symposium on Electron and Photon Interactions at High Energies, SLAC (1975).

23. W. Braunschweig, et al., Phys. Lett. 57B, 407 (1975).

24. G. J. Feldman, et al., Phys. Rev. Letters 35, 821 (1975).

25. B. Margolis, Acta Physica Polonica B2, 57 (1971).

26. H. Bethe and W. Heitler, Proc. Roy. Soc. (London) 146, 83 (1934).

27. J. D. Bjorken, et al., Phys. Rev. 112, 1409 (1958).

28. S. D. Drell and J. D. Walecka, Ann. Phys. 28, 18 (1964).

29. B. Huld, Phys. Rev. 168, 1782 (1968).

30. H. Alvensleben, et al., Phys. Rev. Letters 21, 1501 (1968).

31. J. Tennenbaum, et al., Phys. Rev. D2, 57 (1970).

32. P. J. Biggs, et al., Phys. Rev. Letters 23, 927 (1969).

33. S. Hayes, et al., Phys. Rev. Letters 22, 1134 (1969).

34. J. Knauer, et al., in Proceedings of the Calorimeter Workshop, 215, FNAL (1975).

35. F. Harris and D. Yount, Nucl. Inst. and Meth. 114, 357 (1974).

36. H. Alvensleben, et al., Nucl. Phys. B18, 333 (1970).

37. G. McClellan, et al., Phys. Rev. D4, 2683 (1971).

38. H. J. Behrend, et al., Phys. Rev. Letters 24, 336 (1970).

39. R. Anderson, et al., Phys. Rev. D1, 27 (1970).

40. H. J. Behrend, et al., Phys. Rev. Letters 24, 1246 (1970).

41. J. Ballam, et al., Phys. Rev. Letters 24, 1364 (1970).

42. G. McClellan, et al., Phys. Rev. Letters 22, 374 (1969).

43. G. McClellan, et al., Phys. Rev. Letters 26, 1593 (1971).

44. S. C. C. Ting in Proceedings of the XIV International Conference on High Energy Physics, Vienna (1968).

45. D. Nease, Ph.D. Thesis, Cornell University (1975).

46. B. Knapp, et al., Phys. Rev. Letters 34, 1040 (1975).

47. U. Camerini, et al., Phys. Rev. Letters 35, 483 (1975).

48. B. Gittelman in Proceedings of the 1975 International Symposium on Electron and Photon Interactions at High Energies, SLAC (1975).

49. C. R. Kerns in Proceedings of the Calorimeter Workshop, FNAL, 143 (1975).

50. E. Loh, Cornell University, private communication.

VITA

Laird Renny Cormell, Jr. was born in Youngstown, Ohio He attended public schools in Austintown, Ohio, North Jackson, Ohio, and Midwest City, Oklahoma. He graduated from high school in 1966 from Midwest City High School. He entered the University of Oklahoma in 1966 where he received the degree of Bachelor of Science in Physics in 1970. Since 1970 he has been a student at the University of Illinois where he received the degree of Master of Science in Physics in 1971.